UNIVERSITAT POLITÈCNICA DE CATALUNYA
BARCELONATECH
Departament de Teoria del Senyal
i Comunicacions

Wireless Sensors Embedded in High Permittivity Lossy Media

Thesis by Compendium of Publications

Author

Giselle González López

Thesis Advisor

Prof. Luis Jofre-Roca

A thesis submitted to the Department of Teoria del Senyal i Comunicacions in partial fulfillment of the requirements for the degree of

Doctor of Philosophy

Universitat Politècnica de Catalunya, March 2021

Acknowledgements

The path that has led me to reach this goal in my life, has been filled with people that either professional or personally have helped and guided me to this moment. To them I am tremendously grateful.

From the Technical University of Catalonia, I want to first thank my supervisor Luis Jofre-Roca, who has been there since my master's, and who has proven to be a constant source of knowledge and wisdom. Thank you for your guidance and for your broad and always down to earth perspective.

I also want to thank professor Jordi Romeu who has been like an unofficial second supervisor to me. Your fresh and out of the box ideas are always welcome. All the collaborative work we've done has been a pleasure to me.

To professor Sebastian Blanch, thank you for your ideas, for your knowledge, and for not being afraid to get your hands filled with concrete!

I am also grateful to professors Albert Aguasca and Joan O'Callaghan for their support, their ideas and answers to all sort of questions.

To all the staff from the laboratory and department in general (Rubén Tardio, Eric Vila, Albert Marton, Joaquim Giner, Aynie Khoe and Cristian García), thank you very much for your constant help and understanding.

I want to specially thank my first workmates, but now dear friends Alejandra Garrido, Luca Montero, Susana Amorós, Christian Ballesteros and Jorge Nicolás. I am grateful for the help, the nerdy chat and brainstorming sessions we've had, but for what I am most grateful, is for turning our office into a place you share with friends. This has been priceless to me.

To my partner Miguel, who has unconditionally listened, cheered and supported me throughout the hardest times of this journey. You have been my rock.

Finally, non of this would have been possible without the continuous help and support of my parents. You have always stood by my side and you've made me who I am. This work is dedicated to you.

Abstract

The design of wireless sensors for operation embedded in a medium with high losses creates a series of additional constraints that should be taken into consideration at design stage to enhance sensor performance. In such a medium, both the real and the imaginary part of the relative permittivity will have a high value. In this thesis, the effect of the imaginary part (which basically accounts for medium losses) on sensor performance and signal propagation will be analysed in detail.

Although the attenuating effect the losses of this surrounding medium will have on a propagating microwave signal can be foreseen, there is still much to be learned with respect to how these dielectric properties impact the actual performance of the sensor, and how this effect may be prevented or mitigated at design stage. Furthermore, currently available set-ups to measure the performance of radiating devices have not been conceived to measure devices that do not operate in air.

Bearing this in mind, this thesis intends to shed some light on the specific challenges encountered when designing devices for embedded operation in high permittivity lossy materials. This is done by means of two specific embedded application scenarios. In the first one a wireless RFID temperature sensor is placed inside a concrete structure to monitor the evolution of the setting process of concrete. Whereas in the second scenario a microwave bodyscope is used to monitor metallic implants inside the human body. Finally, in-field results are presented for both scenarios.

High accuracy measurements of the evolution of concrete's relative permittivity over time and frequency are presented, which are then used as reference at sensor design stage. A specific analysis of the correlation between antenna performance and surrounding medium's dielectric properties is conducted and some preliminary design guidelines are provided. Furthermore, a novel miniaturized anechoic chamber for X-wave and embedded measurement is presented.

Resumen

El diseño de sensores inalámbricos para operación dentro de medios con muchas pérdidas, genera una serie de limitaciones adicionales que han de ser tenidas en consideración durante la etapa de diseño para mejorar el rendimiento del sensor. En tal medio, tanto la parte real como la imaginaia de la permitividad relativa tendrán un valor elevado. En esta tesis, el efecto de la parte imaginaria (la cual está asociada a las pérdidas del medio) en el rendimiento del sensor y en la propagación de la señal serán analizados en detalle.

Aunque el efecto atenuante que las pérdidas del medio tienen en una señal de microondas al propagarse a lo largo del mismo resulta previsible, hay aun mucho que aprender con respecto a cómo estas propiedades dieléctricas impactan en el rendimiento del sensor, y cómo este efecto puede ser evitado o mitigado durante la etapa de diseño. Adicionalmente, los sistemas de medida de dispositivos radiantes disponibles actualmente no han sido concebidos para llevar a cabo medidas de dispositivos que no operan en aire.

Con esto en mente, esta tesis tiene la intención de arrojar algo de luz sobre los desafíos específicos asociados al diseño de dispositivos para operación embedida en medios con pérdidas. Para ello, serán utilizados dos escenarios de aplicación específicos. En el primero, un sensor RFID de temperatura es colocado dentro de una estructura de hormigón para monitorizar la evolución del proceso de fraguado del hormigón. Mientras que en el segundo caso un "bodyscope" de microondas es utilizado para monitorizar implantes metálicos dentro del cuerpo humano. Finalmente, resultados de medidas de campo son presentados para ambos escenarios.

Medidas de alta precision de la evolución de la permitividad relativa del hormigón a lo largo del tiempo y en un cierto ancho de banda, son también presentadas. Estos valores son utilizados como referencia durante la etapa de diseño del sensor. Un análisis específico de la correlación entre el rendimiento de la antena y las propiedades dieléctricas del medio es llevado a cabo, y proveyendo algunas recomendaciones preliminares a tener en cuenta durante la etapa de diseño. Finalmente, se presenta un nuevo diseño de una cámara anecoica miniaturizada para medidas de sensores embebidos.

Contents

List of Publications

This thesis consists of an overview of the following publications. They are referred to in the text using their corresponding Roman numbers.

GG-I González-López, G., Blanch, S., Romeu, J., & Jofre, L. (2019). Debye frequency-extended waveguide permittivity extraction for high complex permittivity materials: Concrete setting process characterization. IEEE Transactions on Instrumentation and Measurement, 69(8), 5604-5613.

GG-II González-López, G., Romeu, J., Cairó, I., Segura, I., Ikumi, T., & Jofre-Roca, L. (2020). Wireless Sensing of Concrete Setting Process. Sensors, 20(20), 5965.

GG-III González-López, G., Jofre Roca, L., Amorós García de Valdecasas, S., Rodríguez-Leor, O., Gálvez-Montón, C., Bayés-Genís, A., & O'Callaghan, J. (2019). Resonance-Based microwave technique for body implant sensing. Sensors, 19(22), 4828.

GG-IV González, G., Jofre, L., Romeu, J., & Cairó, I. (2019, March). Variable capacitive antenna loading for embedded RFID sensors. In 2019 13th European Conference on Antennas and Propagation (EuCAP) (pp. 1-5). IEEE.

GG-V Romeu, J., González-López, G., Blanch, S., & Jofre, L. (2020, March). Antenna packaging for in-body applications. In 2020 14th European Conference on Antennas and Propagation (EuCAP) (pp. 1-5). IEEE.

GG-VI González-López, G., de Valdecasas, S. A. G., & Jofre, L. (2020, March). Optimal Probe Geometry for Microwave Monitoring during in-Lab ex-vivo Measurements. In 2020 14th European Conference on Antennas and Propagation (EuCAP) (pp. 1-4). IEEE.

GG-VII Sellés Valls, M., González-López, G. & Jofre, L. (2020). Embedded Sensor Transmission Optimization with a X-Wave mini-Anechoic Chamber. XXXV Simposium Nacional de la Unión Científica Internacional de Radio, Málaga, Spain.

Additional contributions:

GG-VIII Rashid, S., Jofre, L., Garrido, A., Gonzalez, G., Ding, Y., Aguasca, A., ... & Romeu, J. (2019). 3-D printed UWB microwave bodyscope for biomedical measurements. IEEE Antennas and Wireless Propagation Letters, 18(4), 626-630.

GG-IX Vidal, N., Lopez-Villegas, J. M., Romeu, J., Barenys, A. S., Garcia-Miquel, A., González-López, G., & Jofre, L. (2020). 3D-Printed UHF-RFID Tag for Embedded Applications. IEEE access, 8, 146640-146647.

CHAPTER 1

Introduction

1.1 Background

Wireless communication systems are subjected to a constant evolution. Ever since the interest in wireless communications system started, microwave signals propagating in air have been thoroughly studied [1], as well as devices for operation under these circumstances. Nevertheless, the Internet of Things (IoT) revolution has opened the door to the idea of wireless devices operating embedded in all sort of media different than air [2]. This idea embraces many applications for wireless communication systems such as RFID tags in our grocery, or even more disruptive applications like implantable devices inside the human body for medicine, or sensors placed inside concrete structures to monitor the evolution of some physical and chemical parameters, just to mention some examples.

Unlike the case of wireless propagation with air as the propagation medium, the phenomenon of a microwave signal propagating through a material with complex relative permittivity (ε_r^*) different than 1 ($\varepsilon_{rAIR}^* = 1$), implies additional challenges both in terms of the embedded device design and in terms of the attenuation experienced by the signal along the propagation path. Under these circumstances, the study of the impact these new propagation scenarios have on the design strategy and the performance of embedded wireless devices gains a renewed interest.

From classical electromagnetic theory, the correlation between the complex relative permittivity and the propagation constant (γ) of a uniform plane wave in an unbounded lossy medium, is known [3]. However, the impact this complex permittivity has (and in particular its imaginary component ε_r'') on an embedded device in terms of impedance match, distribution of the reactive and propagating EM fields, and amount of energy reaching free-space after coping with reactive near fields, propagation attenuation and reflections at the interface between both medium, are yet to be fully assessed.

1.2 State of the Art

There are two main aspects worth to be addressed regarding the effect the dielectric properties of the propagating medium have on an embedded device. The first one is the measurement technique employed to obtain these complex permittivity values, and whether it is or not the most suitable in terms of accuracy and frequency bandwidth. The second aspect concerns the antenna design, and how it may be prepared to cope with the surrounding medium attenuation and the most-likely variability of its dielectric properties over time.

1.2.1 High Permittivity Lossy Media Characterization

Measurement methods employed nowadays to characterize the dielectric properties of materials can be divided into Reflection Methods and Transmission/Reflection Methods.

- **Reflection methods** extract information from a reflection based measurement to estimate the dielectric properties of the Material Under Test (MUT). Most methods in this group are also "Non-Destructive Methods" as they allow to preserve the sample of the material to be measured. In other words, the measuring gadget is shaped as a probe and does not require the previous preparation of a sample of the material to be measured.
- **Transmission/Reflection methods** extract information from both transmission and reflection measurements to compute the dielectric properties of the MUT. In most cases, previous sample preparation is required, which makes them unsuitable for in-field measurements.

There are some advantages and disadvantages associated to each of these categories. Reflection methods are preferred in general for usage during in-field tests as they employ probe based instrumentation most of the time. Hence, no specific sample preparation is required and no alteration or damage is produced on the medium section employed during the measurement. This is also the main disadvantage of currently available transmission/reflection based measurement methods. Although they provide quite accurate measurement results in most circumstances, they require sample preparation

Table 1.1: Classical Measurement Methods for Complex Permittivity (ε_r^*) Characterization.

Method	Operation Regime	Reference
Open-ended Coaxial Line Method	Rx	[4]
Ground Penetrating Radar (GPR)	Rx	[5]
Time Domain Reflectometry (TDR)	Rx	[6]
Coaxial Closed Cell	Tx/Rx	[7, 8]
Strip Line Method	Tx/Rx	[9]
Free Space Measurement	Tx/Rx	[10]
Rectangular Waveguide Method	Tx/Rx	[11, 12]

and the sample employed cannot be reused afterwards. Some of the most often used measurement methods for complex permittivity characterization are summarized in Table 1.1.

Most of the work that has been conducted to measure the relative permittivity of highly lossy materials relays on methods that are reflection based. This is the case of [13], where the Open-ended Coaxial Line method is employed to characterize the electromagnetic properties of concrete at microwave frequencies from wet to oven dried status. These probe methods are quite appealing when performing Non-Destructive Tests (NDT) as they preserve the sample material.

Nevertheless, when measuring the dielectric properties of a medium with high complex permittivity (ε_r^*), it is not recommended to solely rely on the measured reflection coefficient (S_{11}) (as it is done in reflection methods). The inversion process to retrieve the dielectric permittivity is very sensitive to measurement errors. This is why, under these circumstances, a measurement method that operates on transmission/reflection regime (therefore obtaining information from all four scattering parameters) provides higher reliability on the estimation of the dielectric properties of the material than a method based on a reflection measurement only.

Some of the most common techniques to measure the dielectric properties of materials have been studied in [14, 15], providing insights regarding its applicability scenarios. They both agree on the low resolution and accuracy of reflection based methods.

Coaxial structures [7, 8], strip lines [9] and waveguides [11, 12] are the most typically used transmission lines for material characterization. However, the first two inspect small size samples, which is a drawback when it comes to measuring granular or heterogeneous materials (such as concrete), while the third one is limited in terms of bandwidth.

The selection of the appropriate measurement method for the characterization of a certain material depends on a series of factors such as the accuracy required from the instrumentation, sample preparation feasibility, material composition in a gas-to-liquid-to-solid range, material homogeneity and expected losses of the MUT. When designing devices to operate embedded in materials with high losses, having very accurate and reliable data on the electromagnetic properties of the material is paramount to ensure the proper operation of the embedding device.

1.2.2 Embedded Wireless Sensor Design

The design of wireless sensors for operation embedded in high permittivity lossy materials brings up a series of additional constraints that are not considered in the case of antenna design for free-space propagation. These new constraints can be summarized as follows:

1. Attenuation constant (α) of the embedding medium.
2. Variable relative permittivity (ε_r^*).
3. Antenna Impedance Coupling Factor (ICF).

Attenuation constant (α) of the embedding medium

For the case of a uniform plane wave propagating in free-space and time convention e^{jwt}, the propagation constant takes the form $\gamma = j\beta$ (β is the phase constant of the propagating signal) for a positive travelling wave (i.e. $\vec{E}(z) = Ee^{-\gamma z}$) [16]. However, when the signal is propagating in an unbounded lossy medium [3], the propagation constant is then expressed as (1.1b), where the attenuation constant α represents the attenuation suffered by the signal along its propagation path as consequence of inherent medium losses (1.1c). In this case, the phase constant β is computed using expression (1.1d). The complex permittivity ε_r^* is defined as in (1.1a).

$$\varepsilon_r^* = \varepsilon_r' - j\varepsilon_r'' \tag{1.1a}$$

$$\gamma = \alpha + j\beta \tag{1.1b}$$

$$\alpha = \frac{w}{c_0}\sqrt{\varepsilon_r'}\left\{\frac{1}{2}\left[\sqrt{1+\left(\frac{\varepsilon_r''}{\varepsilon_r'}\right)^2} - 1\right]\right\}^{1/2} \tag{1.1c}$$

$$\beta = \frac{w}{c_0}\sqrt{\varepsilon_r'}\left\{\frac{1}{2}\left[\sqrt{1+\left(\frac{\varepsilon_r''}{\varepsilon_r'}\right)^2} + 1\right]\right\}^{1/2} \tag{1.1d}$$

The fundamental antenna characteristics assumed for radiation into the free-space, like the far field, the radiation pattern or the bandwidth, no longer apply when the antenna is radiating into an infinite lossy medium [17,18]. This is because the radiation power will not only depend on the angular coordinates θ and ϕ (as it does in free-space), but also in the radial coordinate through the term $e^{-2\alpha r}$.

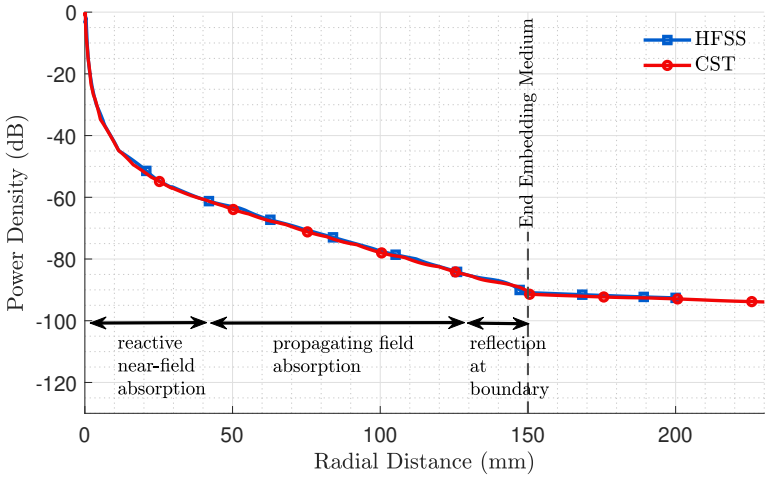

Figure 1.1: Power Density as function of radial distance for a wireless sensor embedded in a spherical concrete medium at 0.868 GHz. Results obtained for simulations in HFSS and CST.

In this propagation scenario, it is possible to separate attenuation experienced by an electromagnetic wave along its propagation path in three zones: (1) the region

immediately surrounding the antenna where the reactive near-field absorption dominates, (2) followed by a region characterized by an exponential decay as consequence of propagating field absorption ($e^{-2\alpha r}$), and (3) at the discontinuity at the embedding medium-free-space boundary (Figure 1.1) [19–21].

Variable relative permittivity (ε_r^*)

In addition to the aforementioned, the relative permittivity of some of these lossy propagation media is dependent on the variations produced on some specific physical and chemical parameters (i.e. a variation in the temperature may translate into a change in ε_r^*).

In [22], tables of the complex relative permittivity of dielectric reference liquids at frequencies up to 5 GHz are provided. It is observed that for the case of ethanol (e.g.), a 40ºC temperature increase (from 10ºC to 50ºC) at 1 GHz translates into an increase in the real part of the permittivity (ε_r') of a 59%, while the Loss Tangent ($\tan\delta = \varepsilon_r''/\varepsilon_r'$) experiments a 61% reduction. The same analysis, but for the case of methanol, reflects a decrease of 11.3% for ε_r' as the temperature is increased, and of 55.6% for $\tan\delta$ (Figure 1.2).

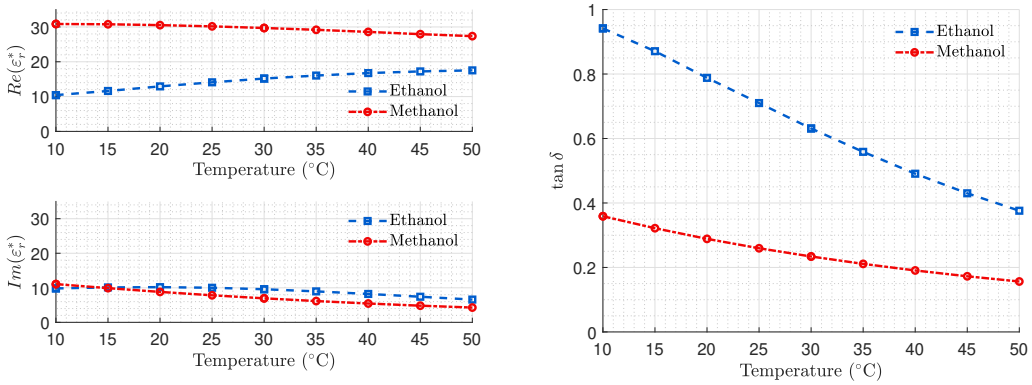

Figure 1.2: Relative Permittivity as a function of temperature at 1 GHz for ethanol and methanol [22]. Real and Imaginary part (a) and Loss Tangent (b).

For the specific case of concrete, the exothermic hydration process associated to the concrete setting causes temperature and also dielectric constant variations of the concrete mixture in the UHF (Ultra High Frequency) band [23]. The most significant temperature changes take place during the first 12 h of the reaction (Figure 1.3) [24,25].

Monitoring the changes in the dielectric constant of the concrete mixture has been proposed in [26] in a wired experimental set-up as a way to monitor the setting process. In [27, 28], RFID (Radio Frequency Identification) based sensors have been demonstrated to measure chlorine ion concentration and humidity inside concrete as a means to monitor concrete corrosion. The potentiality of wireless coupled sensors has also been shown in [29, 30] by embedding inside concrete a strain sensor electromagnetically coupled to an external antenna, and in [31], RFID technology is used to couple a concrete embedded strain gauge to an external reader to monitor 3-axis acceleration of concrete structures. Current systems, such as those in [32, 33], employ passive

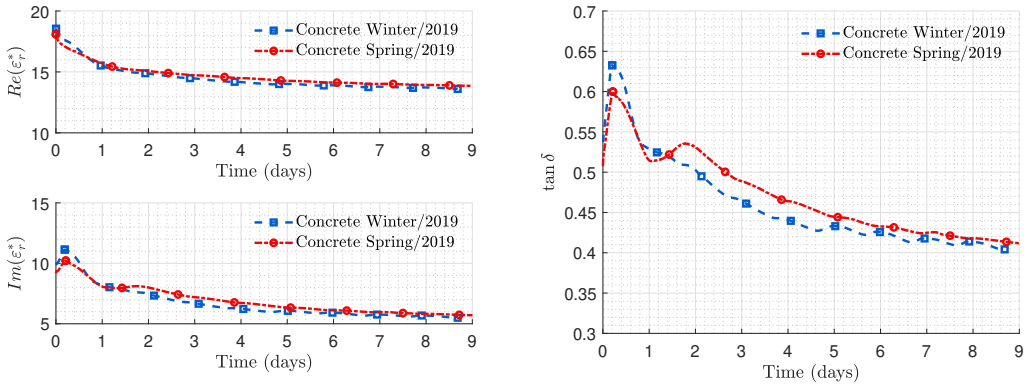

Figure 1.3: Relative Permittivity as a function of time at 0.868 GHz for a concrete sample during its hydration reaction in winter and in spring. Real and Imaginary part (a) and Loss Tangent (b).

RFID sensor T-tags to monitor the setting process of concrete. However, these systems present a poor performance (lacking of information) at the beginning of the setting reaction of concrete, where substantial changes in the dielectric properties of the material are produced, as a consequence of their probe-like design.

Antenna Impedance Coupling Factor (ICF)

The third of the previously mentioned constraints in the design of wireless sensors for operation embedded in high permittivity lossy materials is the antenna Impedance Coupling Factor (ICF) (1.2). The ICF measures the fraction of power load that is effectively transferred from the antenna terminals to the rest of the electronics, and vice versa. The design goal is to obtain a value close to one [16]. This parameter is an indicator of the losses in the communication link as a consequence of antenna impedance mismatch.

$$ICF = \frac{4Re(Z_a)Re(Z_{chip})}{\left(Re(Z_a) + Re(Z_{chip})\right)^2 + \left(Im(Z_a) + Im(Z_{chip}\right)^2} \tag{1.2}$$

In (1.2), Z_a is the antenna impedance and Z_{chip} is the input impedance at the point where the antenna is connected to the rest of the electronics.

The concept of the frequency bandwidth of an antenna radiating into a lossy medium, defined as the band for which the reflection coefficient (S_{11}) is bellow a certain value, loses interest because it is no longer a good indicator of how well the device is radiating as part of the energy may be actually dissipated into the surrounding lossy medium. The matching of the device arises a more sensitive problem and the input impedance ($Z_{in} = Z_a$) becomes more illustrative of proper antenna match [17, 34].

Additionally, the effect of medium losses is also present in the real part of the antenna impedance (R_a) through the loss resistance (R_l) (1.3a). This parameter is associated to the amount of power dissipated as ohmic losses. In a lossy environment this will mean that if the contribution of R_l to the total antenna resistance (R_a) is significant,

then not only the real part of the impedance will not be well matched, but also most of this energy will not be radiated but rather dissipated into the lossy medium. In (1.3a), R_r is the antenna radiation resistance and it is related to the power delivered to the antenna for radiation (P_r) through (1.3b). I_g is the current at the antenna terminals. The higher the impact of medium losses on the antenna impedance, the smaller the contribution of R_r to the total R_a, and therefore the smaller the radiated power [35].

$$R_a = R_r + R_l \tag{1.3a}$$

$$P_r = \frac{1}{2}|I_g|^2 R_r \tag{1.3b}$$

The aforementioned phenomenon introduces an additional level of complexity in the design of RFID antennas for these scenarios. Typically, RFID antenna impedance is characterized by a highly inductive imaginary part and a very small real part to math RFID chips' input impedance (small resistive part, highly capacitive reactance) [36].

Under these circumstances, ensuring that the effect of medium loss on antenna performance is mitigated as much as possible by means of a thorough and effective sensor design gains a significant importance.

1.3 Motivation and Objectives

Considering the current state of the art on the design of wireless sensors for propagation embedded in high permittivity lossy media, as described in the previous section, some hot topics have been identified.

There are two main concerns that have motivated this thesis:

1. **How to accurately account for the effect of the losses of a complex permittivity medium on a microwave signal propagating through it?**
2. **What additional constraints should be considered at the design stage of wireless sensors, and in particular into the sensor antenna, so the effect of the surrounding medium is mitigated?**

Some additional questions that shall be addressed throughout this thesis are:

- How can high accuracy permittivity (ε_r^*) data collection improve the design and performance of embedded wireless sensors?
- How can the effect of ε_r^* on the antenna match and signal propagation be accounted for?
- How can current scenarios for antenna measurement be upgraded to conceive measurements where the propagating medium is not always air?

- What specific design rules can improve the performance and endurance of wireless embedded sensors?

In accordance with the questions raised above, the research objectives are as follows:

1. Provide an analytic formulation of the antenna radiation and propagation in complex dielectric media.
2. Conduct a high accuracy measurement of the complex permittivity over time and frequency of several cement based materials, and compare the results with data available in the literature.
3. Evaluate the effect of medium losses on antenna match and propagating signal attenuation, and propose techniques to mitigate it.
4. Propose a novel miniaturized set-up to measure wireless devices embedded in media different than air.
5. Present two specific design examples of embedded wireless sensors, one for the concrete industry and another for biomedical applications.

1.4 Thesis Outline

Based on the objectives defined in the previous section, and in accordance with the publications **GG-I** to **GG-VII** included in Chapter 5, this thesis is structured as follows:

- **Chapter 2** is focused on the particularities of high permittivity lossy media from a microwave propagation point of view. The results obtained in [**GG-I**] for the measurement of concrete's ε_r^* over time and frequency are included and analysed. The effects of the host medium complex permittivity on antenna match and signal propagation are analysed by means of the results presented in [**GG-IV**] and [**GG-V**]. The design and final prototype of a miniaturized anechoic chamber for X-wave and embedded measurements, presented in [**GG-VII**] is also discussed.
- **Chapter 3** presents two working wireless embedded systems. The first one consists on a RFID temperature sensor for operation inside concrete published in [**GG-II**], and the second one describes a resonance-based microwave technique for sensing applications involving metallic implants in the human body, published in [**GG-III**] and [**GG-VI**] respectively.
- **Chapter 4** summarizes the main contributions and conclusions of this thesis, and outlines some lines for future research emerging from the results that have been presented.
- **Chapter 5** contains the nine articles included in this document, generated during the development of the pre-doctoral period. Articles [**GG-I**], [**GG-II**] and [**GG-III**] were the ones chosen to request the presentation of this thesis as a compendium of publications.

CHAPTER 2

High Permittivity Lossy Media

The structure of this chapter has been conceived to tackle objectives 1 to 3, as defined in the previous chapter. In Section 2.1, objective 1 is addressed by introducing the work published in [**GG-I**]. Section 2.2 attends to objective 2 by discussing the results presented in [**GG-IV**] and [**GG-V**]. While Section 2.3 examines the solution introduced in [**GG-VII**] which is linked to objective 3.

2.1 Concrete's High Accuracy Complex Permittivity Measurement

2.1.1 Theoretical Introduction

As it was introduced in Section 1.2.1, it is paramount for the proper design of wireless sensors embedded in high permittivity materials to have high accuracy data on its dielectric properties (along the operation frequency bandwidth and over time) for the case of time-variable ε_r^*. When selecting the measurement method to be employed to obtain this data, compromises should be made in terms of frequency bandwidth, measurement accuracy, need for sample preparation and feasibility to measure granular materials, among others.

For the specific application of measuring the evolution of the dielectric properties of cement based materials at microwave frequencies, it has been proposed in [**GG-I**] the use of a transmission/reflection based rectangular waveguide, propagating the fundamental mode TE_{10}, at a frequency band at which the inner dimensions of a waveguide are large enough to host a granular material. It is then Debye frequency-extended to surmount the bandwidth limitation of traditional waveguides. Measurements have been conducted for frequencies from 0.7 GHz to 1.1 GHz. These results have been then frequency-extended from 0.4 GHz to 3 GHz using a validated Debye model.

Given the correlation between the high temperatures produced during concrete's hydration process and the variation of its dielectric properties, it is possible to extract information regarding the strength and stiffness of freshly placed concrete from the time evolution of the dielectric properties [37–39]. Therefore, the relation between concrete's internal temperature and its dielectric properties will also be monitored by strategically placing several type K thermocouples connected to a data logger [40].

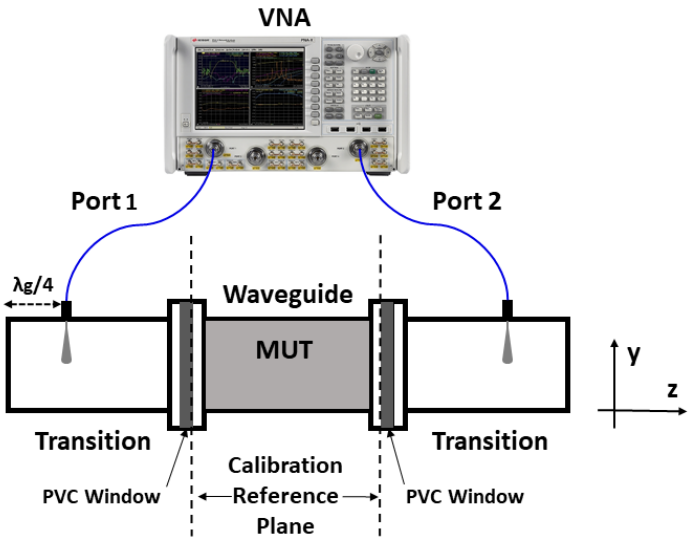

Figure 2.1: Schematic representation of a concrete permittivity measurement.

A schematic representation of the measurement configuration is shown in Figure 2.1. The relative permittivity of the analysed sample is retrieved from the measured scattering parameters ([S]) applying the Nicolson-Ross-Weir model in [41] (equations (2.1)).

$$T = \frac{S_{11} + S_{21} - \Gamma}{1 - (S_{11} + S_{21})\Gamma} \tag{2.1a}$$

$$\Gamma = A \pm \sqrt{A^2 - 1} \tag{2.1b}$$

$$A = \frac{{S_{11}}^2 - {S_{21}}^2 + 1}{2S_{11}} \tag{2.1c}$$

The transmission parameter ([T]) (equation 2.1a) for a wave propagating through the sample is equal to the propagation factor in (2.2), corresponding d to the length of the waveguide's "sample holder" inner section. The complex propagation constant γ for the TE_{10} mode (dominant mode) in a rectangular waveguide filled with a dielectric is given in 2.3, being a the inner width of the waveguide's "sample holder" section and ε_r^* the parameter to be calculated [16].

$$P = e^{-\gamma d} \tag{2.2}$$

$$\gamma = \sqrt{\left(\frac{\pi}{a}\right)^2 - \left(\frac{w}{c_0}\right)^2 \varepsilon_r^*} \tag{2.3}$$

To frequency-extend the relative permittivity results beyond the 0.4 GHz bandwidth offered by the manufactured waveguide (from 0.7 GHz to 1.1 GHz originally, and extended to 0.4 GHz to 3 GHz), the Debye relaxation model has been employed [42]. The Debye-Γ model (equation 2.4) specifically, has been demonstrated to offer an appropriate (0.45% and 0.56% error for the real and imaginary part of ε_r^*, respectively) representation of the behaviour of concrete's dielectric properties over the frequency interval of interest [43, 44].

$$\varepsilon_r^* = \varepsilon_\infty + \frac{\varepsilon_s - \varepsilon_\infty}{1 + j\frac{f}{f_r}} - j\frac{\sigma}{w} - jf\Gamma_D \tag{2.4}$$

In (2.4), the parameters ε_∞ (high-frequency permittivity limit), ε_s (static permittivity), f_r (relaxation frequency), σ (static conductivity), and Γ_D (fitting parameter) have been obtained through minimum squared error estimation. The third term in (2.4) naturally models the loss of the dielectric material [45], while the positive quantity Γ_D in the last term represents the tail of the second relaxation frequency.

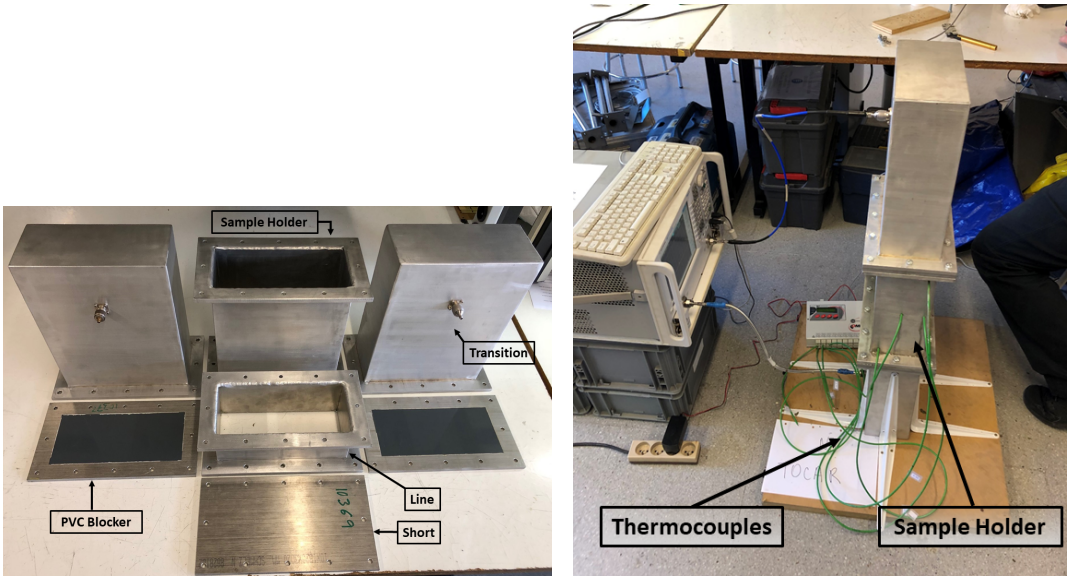

(a) (b)

Figure 2.2: Set-up of an ongoing measurement.

2.1.2 Main Results

The results included in this section have been obtained for two samples of H-25PRO concrete, each measured at a different season (winter and spring), and a sample of self-leveling mortar. Each sample has a volume of $9.2dm^3$ and has been prepared using the ratios in Table 2.1. The concrete samples have been monitored during nine days, while the sample of mortar has been monitored during six days. Measurements were taken every 5 minutes in every case. Measurements started 20 minutes after preparing the mixture, in average.

The results presented in Figure 2.3 correspond to the measured relative permittivity of concrete and mortar over time at 0.868 GHz. It is observed that the high water

Table 2.1: Sample preparation ratios of H-25PRO concrete and self-leveling mortar. These values have been computed in accordance with the data provided by the manufacturers and the EHE-08 instruction [46]. The volume of the sample is of $9.2dm^3$ and ϕ is the diameter of the aggregates.

	H-25PRO Concrete	**Self-leveling Mortar**
Water	195 l/m^3	522 l/m^3
Cement	325 l/m^3	325 l/m^3
Sand ($\phi = 0 - 4mm$)	979 l/m^3	1153 l/m^3
Gravel ($\phi = 4 - 10mm$)	801 l/m^3	-

concentration present at the beginning of concrete's setting reaction, along with the effect of the exothermic hydration reaction, generates high ε_r^* values at early stages of the process. Once passed the peak, both real and imaginary part of ε_r^* tend to decrease as the reaction stabilizes. It is of interest to call attention on the peak produced in the dielectric properties during the first 24 hours of the reaction. During this time lapse, an abrupt increase in the losses of the materials take place (Figure 2.3b), followed by a quite sharp decrease that starts stabilizing by the end of the first day of measurement. This interval coincides with the most critical moment of the hydration reaction of cement.

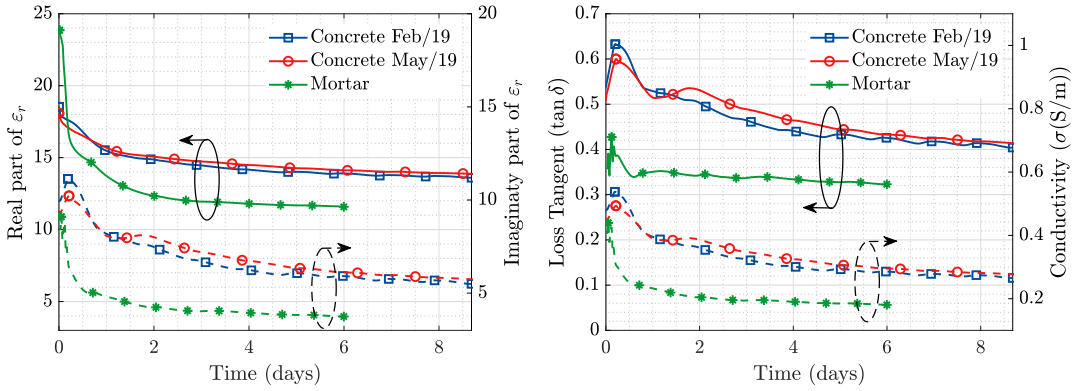

Figure 2.3: Relative Permittivity evolution over time of all measured materials at 0.868 GHz. **(a)** Real and Imaginary part of ε_r^* and **(b)** Loss Tangent ($\tan\delta = \varepsilon_r''/\varepsilon_r'$) and Electric Conductivity ($\sigma = \omega\varepsilon_0\varepsilon_r''$). Straight lines correspond to the left vertical axis, and dashed lines to the right vertical axis.

The relative permittivity values obtained with this measurement are higher (around 45% for ε_r' and 80% for ε_r'') than those reported in [5, 8, 10, 12, 13, 26, 47–50]. Figure 2.4 compares the ε_r^* values extracted with this measurement with previously published results of concrete permittivity obtained through different measurement methods (Table 2.2) either transmission/reflection based, or reflection based.

The data measured for the complex permittivity of the three analysed samples from 0.7 GHz to 1.1 GHz, has been frequency extended applying the fitted Debye model in (2.4), providing an in-band accuracy above 99.9% for both real and imaginary part of ε_r^*. Figure 2.5 displays the measured permittivity at 0.868 GHz, as well as the complex permittivity values obtained at 0.43 GHz, 0.7 GHz, 1.0 GHz, 1.25 GHz, 2.5 GHz and 3.0 GHz for the Debye-Γ model for the H-25PROv1 sample (Figure 2.5a and 2.5b), the H-25PROv2 sample (Figure 2.5c and 2.5d) and the self-leveling mortar sample (Figure 2.5e and 2.5f). The fitting parameters obtained for the Debye-Γ model at different time

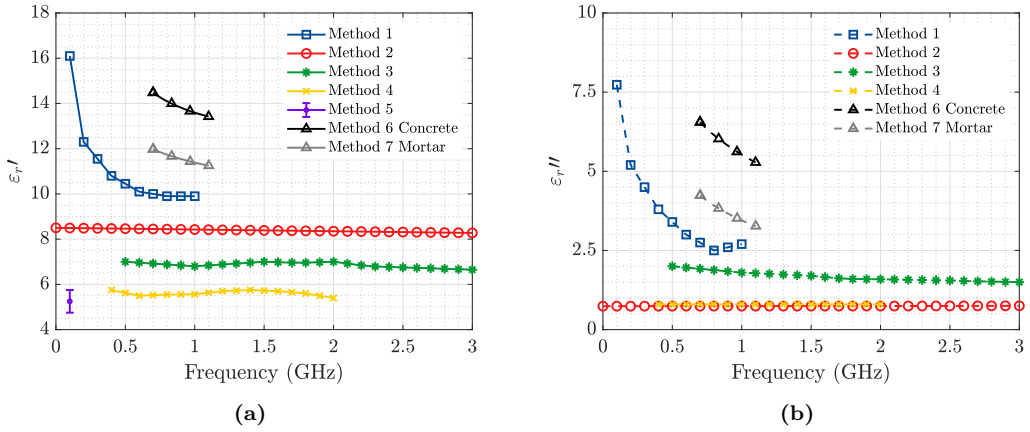

Figure 2.4: Published values of concrete relative permittivity obtained through measurements methods in Table 2.2. These data have been collected (within feasibility) for concrete samples in a stable stage of the setting process. Values measured for self-leveling mortar are also included. (a) ε_r' and (b) ε_r''.

Table 2.2: Published concrete permittivity measurement methods.

	Method	**Operation Regime**
Method 1	Coaxial Closed Cell	Tx/Rx
Method 2	Open-ended Coaxial Probe	Rx
Method 3	Free Space Measurement	Tx/Rx
Method 4	Ground Penetrating Radar (GPR)	Rx
Method 5	Time Domain Reflectometry (TDR)	Rx
Method 6/7	Waveguide Transmission Line ([**GG-I**])	Tx/Rx

instants are included in Tables 2.3 to 2.5, and they can be extended to other frequencies by applying equation (2.4). From these parameters, it is possible to notice that the most significant variation is produced in the static conductivity (σ) (see equation (2.4)), which agrees with the results presented in [51].

The results presented in [**GG-I**] are proof of the convenience of employing transmission/reflection based waveguide structures to measure high permittivity lossy granular materials. Relaxation models, such as the Debye model, can be applied to frequency-extend the complex permittivity measurement of granular materials in scenarios where it is not feasible to conduct measurements at higher frequencies. This happens, for example, when the maximum sample size required by the instrumentation is smaller than the minimum feasible sample size of the material under test.

The electromagnetic properties of concrete exhibit a stable behavior after the first week of the setting process. Nevertheless, after this amount of time, it is still required to overcome 18 dB in ohmic loss attenuation only to communicate with a device embedded 15 cm deep, while it requires 30 dB at the time instant the attenuation peak is produced.

These data can be employed to determine either penetration depths or matching of the device under the effect of the dielectric properties of the surrounding medium. Furthermore, for those applications where it is a must being able to maintain a reliable and stable communication link with an embedded device since the beginning of the setting process of concrete, it is paramount to know the exact variations that take

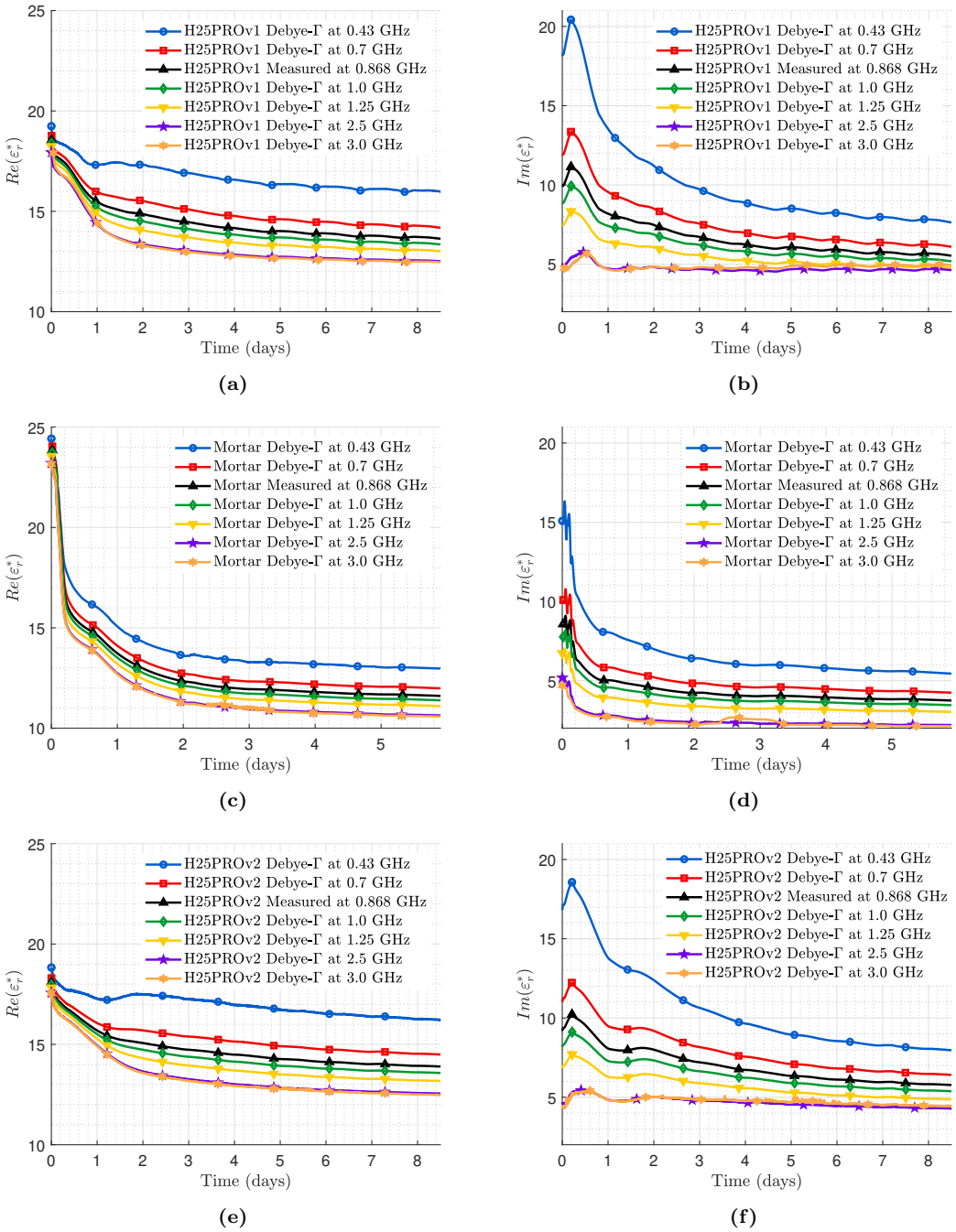

Figure 2.5: Debye-Γ frequency-extended ε_r^* of H-25PROv1 (winter) concrete sample ((a) and (b)), H-25PROv2 (spring) concrete sample ((c) and (d)) and self-leveling mortar sample ((e) and (f)) over time, for frequencies 0.43 GHz, 0.7 GHz, 0.868 GHz, 1.0 GHz, 1.25 GHz, 2.5 GHz and 3.0 GHz.

place on its relative complex permittivity, either to ensure good matching or to be able to adjust the transmission equation, hence to withstand the peak produced in the ohmic loss attenuation during the first stages of the reaction.

Table 2.3: Debye-Γ model parameters for ε_r^* of H-25PROv1 concrete sample.

Parameter	Day 1	Day 2	Day 4	Day 8
ε_∞	14.3035	13.1099	12.6258	12.3679
ε_s	19.9943	20.7391	20.6300	20.6215
f_r	0.4558	0.4776	0.4253	0.3855
σ	0.2520	0.1705	0.1068	0.0772
Γ_D	0.7733	0.8750	1.0167	1.1576

Table 2.4: Debye-Γ model parameters for ε_r^* of H-25PROv2 concrete sample.

Parameter	Day 1	Day 2	Day 4	Day 8
ε_∞	14.8216	13.4032	12.7487	12.3366
ε_s	20.7496	21.1904	20.5541	19.7675
f_r	0.3609	0.4530	0.4653	0.4543
σ	0.2512	0.1939	0.1281	0.0944
Γ_D	0.8776	0.9036	0.9366	0.9278

Table 2.5: Debye-Γ model parameters for ε_r^* of self-leveling mortar sample.

Parameter	Day 1	Day 2	Day 4
ε_∞	12.5679	11.0993	10.6094
ε_s	16.7096	14.8947	14.7421
f_r	0.5325	0.6036	0.5525
σ	0.1290	0.1076	0.0875
Γ_D	0.3474	0.2728	0.3098

2.2 Complex Permittivity Effect on Antenna Match and Signal Propagation

2.2.1 Theoretical Introduction

As it is hinted in Chapter 1, having some preliminary knowledge on the effect the dielectric properties of the surrounding medium will have on an embedded sensor, is of great use, not only from the time saving point of view, but also because under the guidance of appropriate design rules, an improved antenna design in terms of radiation efficiency, will be able to offer a better performance while consuming less power and being in general less costly.

From the results presented in [**GG-IV**] it is possible to observe how the impedance of an antenna embedded in a time-dependent lossy medium is subjected to the variations produced in the medium's complex permittivity ε_r^*. It is also seen that this variation can be seized by antenna engineers by designing devices that follow the same behaviour. Furthermore, having a better understanding of the physical processes produced in the electromagnetic field generated by the antenna, may provide more general antenna design guidelines under these circumstances.

In [**GG-V**], cylindrical mode expansions are applied to evaluate the effect on antenna

resistance and reactance of the variations produced on ε_r^*. It shows that if an electrical antenna is packaged inside a dielectric (loss free) cylinder of radius of the order of 0.1λ the major fraction of the reactive electric field will be contained inside this cylinder. Further analysis has been conducted to evaluate more precisely the role this packaging has, and the impact of its dimensions and shape, on the amount of radiated energy reaching free-space and mode excitation.

2.2.2 Main Results

The case-study of a typical meander line RFID antenna covered with a loss-free cylindrical packaging, used as an implantable device for biomedical applications, has been chosen in **[GG-V]** to evaluate the impact of the medium's relative permittivity variation on antenna impedance for several packaging diameters (Figure 2.6). Figure 2.7 displays the input impedance of the considered antenna from 0.8 GHZ to 0.9 GHz, when the surrounding medium has the relative permittivity of (a) brain ($\varepsilon_r' = 57, \tan\delta = 0.6$), (b) bone cancellous ($\varepsilon_r' = 20.9, \tan\delta = 0.32$) and (c) fat ($\varepsilon_r' = 11.3, \tan\delta = 0.2$) [52]. The isolating effect produced by the packaging is evaluated by considering the case where there is no packaging covering the antenna (Figure 2.7a), a $0.1\lambda_p$ (λ_p is the effective wavelength of the packaging material) radius packaging is placed (Figure 2.7b) and a $0.5\lambda_p$ radius packaging is placed (Figure 2.7c).

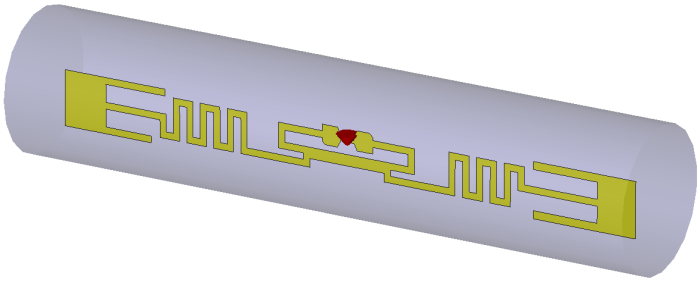

Figure 2.6: Modeled Meander Line RFID Antenna.

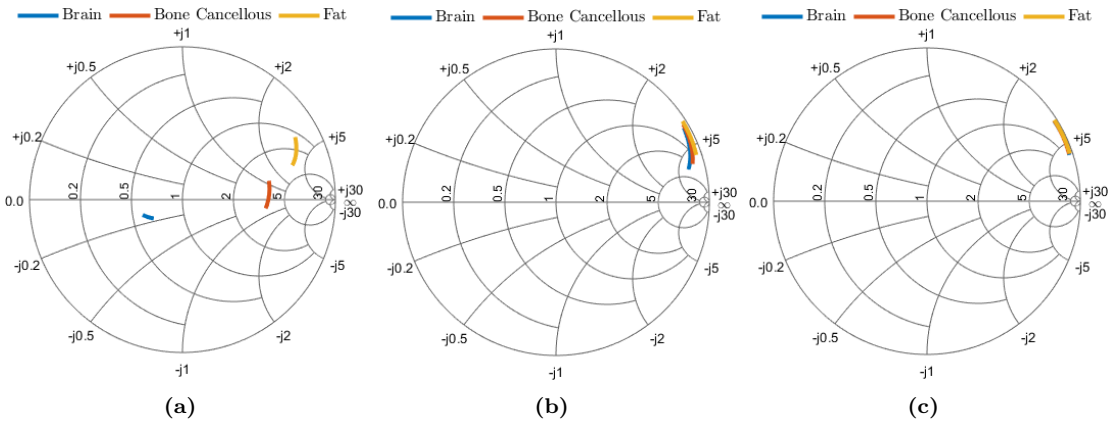

Figure 2.7: Antenna impedance from 0.8 GHz to 0.9 GHz for Brain, Bone Cancellous and Fat. (a) No packaging, (b), $0.1\lambda_p$=10.9mm radius packaging, $0.5\lambda_p$=54.6mm radius packaging

By employing a small insulation shaped as a cylindrical packaging, the effect of the change in the relative permittivity of the surrounding medium is mitigated (Figure

2.7b). By further increasing the insulation radius (Figure 2.7c), it is possible to reduce the effect of the change in the relative permittivity of the medium until it is almost neglectable.

To further evaluate packaging effect, this time on the amount of energy radiated into the free-space by the embedded device, the RFID antenna (planar Bow-Tie T-Match antenna) proposed in [34] covered with a cube-shaped packaging of dimensions $t(mm)$ x $t(mm)$ x $t(mm)$ and placed in the center of a sphere of radius $r(mm)$ with dielectric properties extracted from [**GG-I**], is analysed (Figure 2.8).

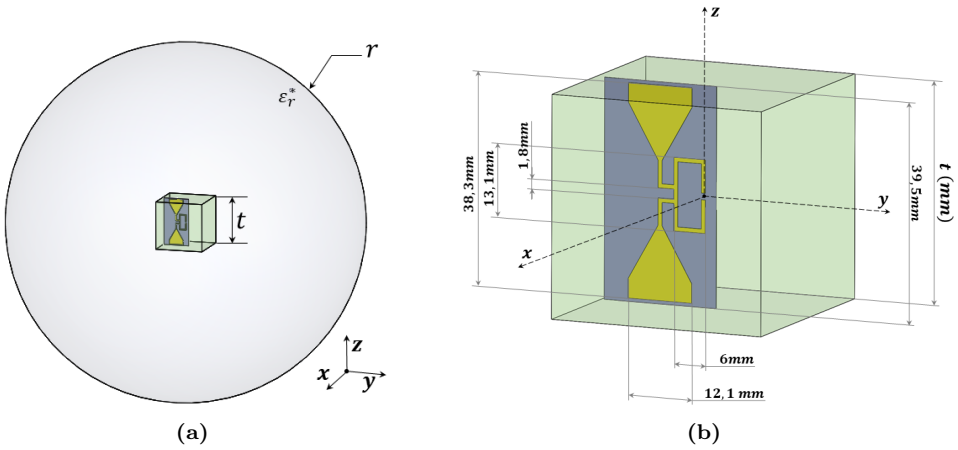

Figure 2.8: Planar Bow-Tie T-Match RFID Antenna.

In Figure 2.9 the total radiated power over frequency (i.e. the power reaching free space normalized by the input power) has been represented for the considered scenario. The study has been conducted using Finite Element Method (FEM) in Ansys HFSS, and the results validated with the canonical method based on Spherical Wave Expansions (SWE) presented by [53]. The behaviour of the total radiated power for variable concrete sphere radius (packaging size t fixed at 40 mm) is displayed in Figure 2.9a. Whereas Figure 2.9b displays the behaviour of the total radiated power for variable packaging size (concrete sphere radius r fixed at 150 mm).

It can be observed from Figure 2.9 that the frequency, the radius (r) of the embedding medium sphere, and the packaging size (t), altogether affect the value of the total radiated power. This is because, as stated in [54], the frequency and properties of concrete (ε_r^* frequency dependant) jointly determine the field region of the source where the concrete-air interface is located. Also, increasing t reduces the reactive near-field losses, which are significant for electric dipoles.

The normalized total radiated power as a function of frequency and radial distance at days 0.5, 4 and 8 of the setting reaction of concrete is represented in Figure 2.10. The case of a device embedded 50 mm into concrete is displayed Figure 2.10a, while Figure 2.10b displays a 100 mm deep device. It can be noticed that for shallow devices (i.e. r $<$ 50 mm), the optimal operation frequency is close to 1 GHz, while for devices located deeper into the embedding medium (i.e. r $>$ 100 mm) optimal operation frequencies are located in the lower part of the represented frequency range (around 0.5 GHz). Additionally, both for a shallow and a deeply embedded device, the total radiated power reaching free space at different stages of the setting reaction of concrete tends to the same value for frequencies close to the higher end of the represented band. For

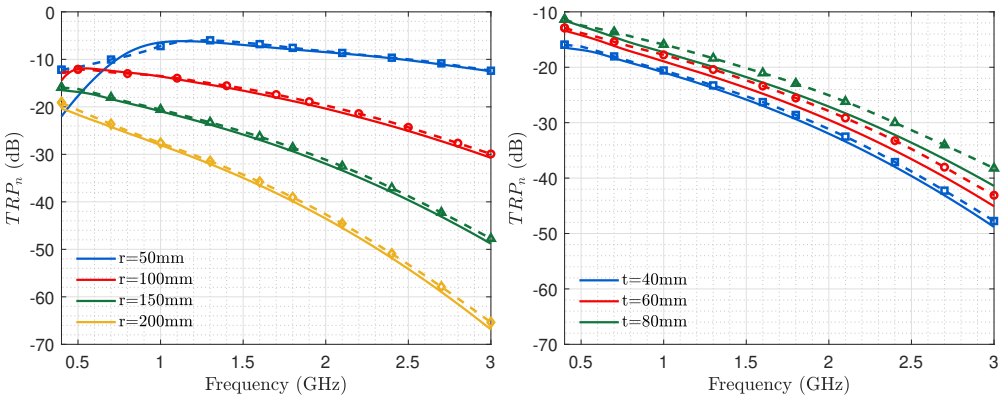

Figure 2.9: Normalized Total Radiated Power over frequency (propagating into the free-space) for variable **(a)** r (radius of the concrete sphere) (t fixed at 40 mm), and **(b)** t (packaging size) (r fixed at 150 mm). SWE results are represented in straight lines, while dashed lines represent HFSS results.

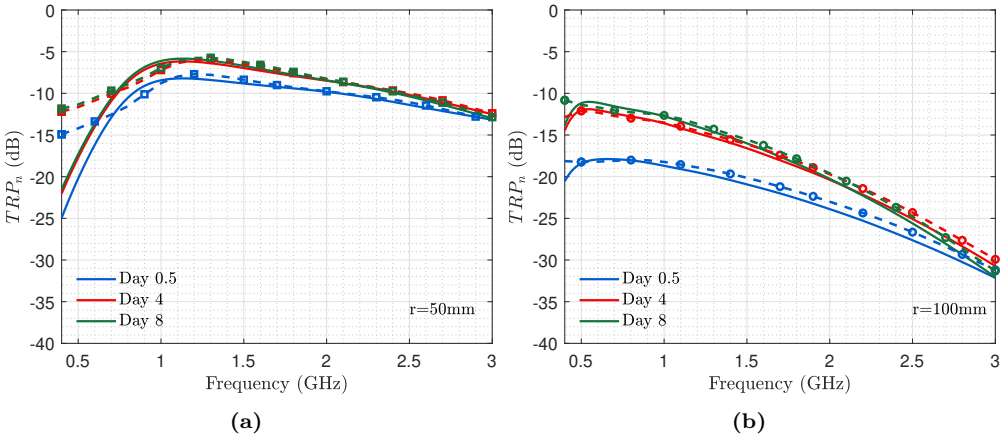

Figure 2.10: Normalized Total Radiation Power over frequency (propagating into the free-space) at days 0.5, 4 and 8 of the setting reaction of concrete with t fixed at 40 mm, for **(a)** $r = 50mm$ and **(b)** $r = 100mm$. SWE results are represented in straight lines, while dashed lines represent HFSS results.

deeply embedded devices, selecting the optimal operation frequency is critical as it would represent a performance increase in the order of 40dB, with respect to the worse case. On the other hand, this is not so critical for the case of shallow implants, where the difference would be close to 10dB.

Finally, to evaluate the impact of packaging shape and dimensions on propagation mode excitation, the power density distribution over a transverse cut in the XY plane, has been represented in Figure 2.11. This time, three different operation frequencies are analysed and both a spherical and a cube packaging are considered. It can be observed that at 0.8 GHz only the fundamental mode is excited for both cube and spherical packaging (Figure 2.11a and 2.11d). Whereas at 2.5 GHz (Figure 2.11b and 2.11e), the difference in terms of homogeneity of the power density distribution between cube and spherical packaging is indicative of the impact packaging shape start to have on mode propagation at higher frequencies. At 2.9 GHz (Figure 2.11c and 2.11f), it is observed that secondary modes are excited for both packaging geometries. At frequencies above 2.5 GHz secondary modes start being excited, and packaging geometry plays a

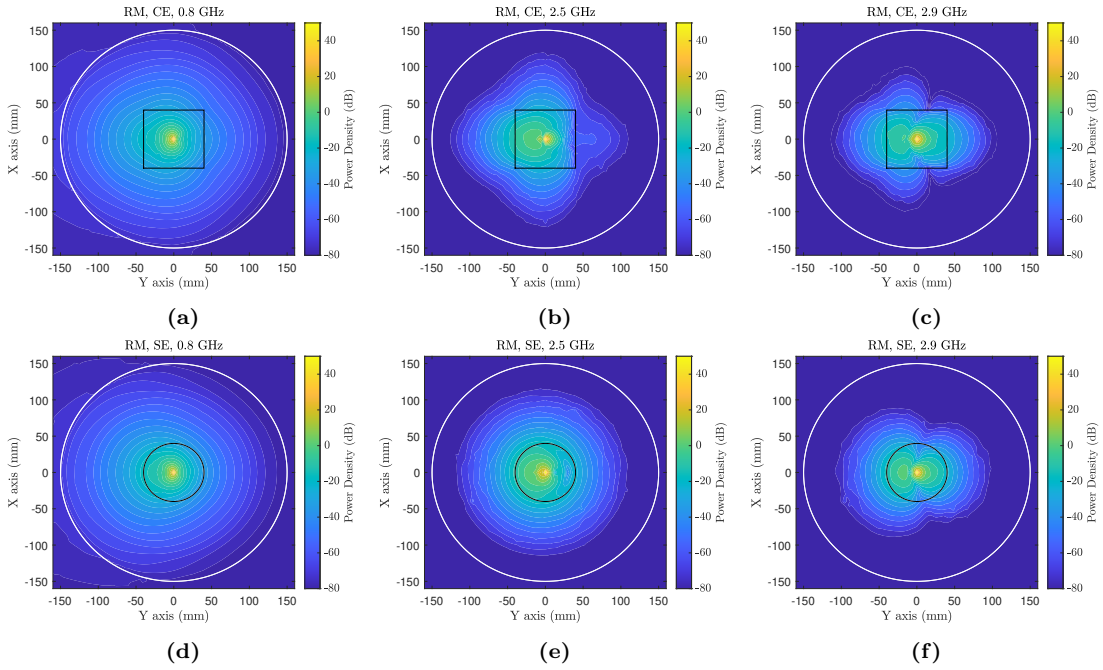

Figure 2.11: Power Density along the XY plane of the proposed model at 0.8 GHz, 2.5 GHz and 2.9 GHz. Cube packaging (CP) has been represented in (a) to (c), while Spherical packaging (SP) in (d) to (f), considering an 80 mm thickness (CP) / diameter (SP).

significant role on determining the frequency at which these modes start to appear.

2.3 X-Wave Miniaturized Anechoic Chamber (X-MAC)

2.3.1 Theoretical Introduction

As a last stage on the road-map to shed some light on the phenomenon of microwave propagation on high permittivity lossy media, the design (both mechanical and electromagnetic) of a miniaturized anechoic chamber for X-wave and embedded measurement has been conceived. This work has been fully presented in [55] and **[GG-VII]**, and it was conducted as part of a joint collaboration with M. Sellés.

The proposed miniaturized anechoic chamber in Figure 2.12, has been designed following standard guidelines for indoor anechoic chamber design [56], while remaining a cost-effective solution. The electrical design is mainly focused on isolating the set up from external interference signals and absorbing the reflections from EM signals generated inside. The mechanical design, on the other hand, has been conceived to enable a motorized 2-axis independent movement between Reference Antenna (RA) and Antenna Under Test (AUT), along with a $360^{\underline{o}}$ rotation for each device. These features equip the X-MAC to conduct 3D near-field to far-field measurements of the two port network full scattering matrix characterization, as well as a projection onto the far-field of the AUT's electromagnetic field.

The propagation scenario in Figure 2.12 can be described as the problem of two

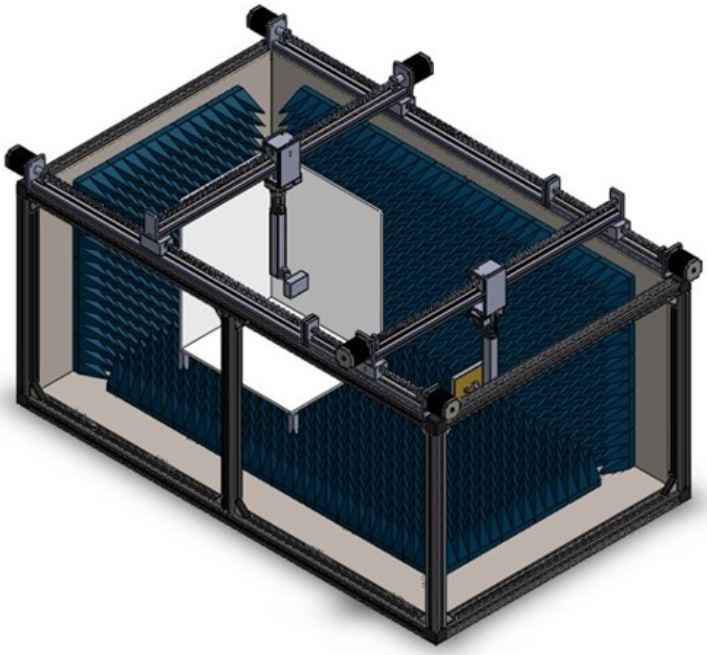

Figure 2.12: CAD Design of the X-Wave Miniaturized Anechoic Chamber.

sources (RA and AUT) with spherical wave propagation, each one propagating in a medium with different dielectric properties. Hence, the problem of an heterogeneous propagation path. The transmission equation based on the classical model for spherical wave propagation in (2.5a), was conceived to describe the propagation path between two radiating elements placed in air [35]. This equation, can be easily readjusted to describe the propagation path these two elements would have if they were placed in a medium with a different permittivity instead. It is done by replacing the phase constant (β) for the propagation constant ($\gamma = \alpha + j\beta$), where (α) is the attenuation constant of the medium, and (λ_0) by the effective wavelength of the medium ($\lambda_e = \lambda_0/\sqrt{\varepsilon_r'}$) [16].

Nevertheless, when only one of the antennas is placed inside the embedding medium, this equation does not provide an accurate representation of the behaviour of the propagation path between antennas. In this case, the Huygens principle allows to tackle this problem as the problem of the propagation of two sources, one (real) with origin at one of the antennas, and the other one (equivalent aperture) with origin at the medium interface. In this way, it is possible to make an analytical representation that describes more accurately the current propagation scenario ((2.5b) and (2.5c)).

$$S_{21} = Ae^{-jk_0(d_{AUT}+d_{RA})}\left(\frac{\lambda_0}{4\pi(d_{AUT}+d_{RA})}\right) \tag{2.5a}$$

$$S_{12A1} = Ae^{-\alpha_{MUT}d_{AUT}}e^{-jk_0(d_{AUT}+d_{RA})}\left(\frac{\lambda_0}{4\pi(d_{AUT}+d_{RA})}\right) \tag{2.5b}$$

$$S_{12A2} = Ae^{-\alpha_{MUT}d_{AUT}}e^{-jk_0d_{RA}}e^{-jk_{MUT}d_{AUT}}\left(\frac{\lambda_0}{4\pi d_{RA}}\right)\left(\frac{\lambda_{MUT}}{4\pi d_{AUT}}\right) \tag{2.5c}$$

$$A = \sqrt{G_{RA}G_{AUT}\rho^2_{air-MUT}\frac{Re(Z_{RA})}{Re(Z_{AUT})}} \tag{2.5d}$$

Equation (2.5b) applies the conception of the classical model for spherical wave propagation to the transmission coefficient of the current scenario (Approximation 1), while equation (2.5c) represents the proposed propagation analytic model (Approximation 2). In (2.5), λ_0 and λ_{MUT} are the wavelength in air and in the embedding medium, respectively. d_{RA} is the distance from the RA to the interface with the medium, while d_{AUT} is the equivalent parameter with respect to the AUT. α_{MUT} is the attenuation constant of the medium (1.1c), k_0 is the phase constant in air and k_{MUT} the phase constant in the lossy medium [16]. G_{RA} and G_{AUT} are the gains of the RA and the AUT respectively, $\rho_{air-MUT}$ is the transmission coefficient at the interface between the medium and air (2.6), and $Re(Z_{RA})$ and $Re(Z_{AUT})$ are the real part of the RA and the AUT's input impedance.

$$\rho_{air-MUT} = 1 + \frac{1 - \sqrt{\varepsilon'_r}}{1 + \sqrt{\varepsilon'_r}} \tag{2.6}$$

From the results presented in the following section, it will be possible to observe that depending on the dielectric properties of the embedding medium, the behaviour of the S_{12} parameter will be closer to either Approximation (2.5b) or (2.5c).

2.3.2 Main Results

For the general case of two elementary electric sources at 0.868 GHz one embedded in a medium of permitivity ε_r^* and the other one in air, separated a distance $d_T = d_{RA} + d_{AUT}$, the transmission coefficient (calculated using the Finite Element Method in Ansys HFSS) as a function of d_{RA} is as depicted in Figure 2.13 for three different propagation media. It can be observed that the higher the losses in medium, the better the fit provided by Approximation (2.5c) to describe the behaviour of the S_{12} parameter. It is also noticed that the classical expression for spherical wave propagation in (2.5b) does not provide an accurate representation of the considered propagation scenario.

The manufactured miniaturized anechoic chamber is depicted in Figure 2.14, and its main mechanical and electrical parameters are summarized in Table 2.6. All non-motorized parts have been designed and manufactured in-house using 3D printing techniques in PLA ($\varepsilon_{rPLA} = 2.5, \tan\delta = 0.004$). The motorized movement of both linear and rotary stages, as well as Keysight's n5247a PNA operation, are software controlled from an unified program written in MatLab. The interference generated by the cables and other metallic parts in the measurement is removed by software using time gating techniques.

The costs of classical anechoic chambers are often in the order of a quarter of a million dollars, today's less pricey alternatives range the 100 thousand dollars [57]. The proposed miniaturized anechoic chamber lowers these figures by a factor of 10, presenting itself as a cost-effective solution for in-house measurement of embedded wireless devices.

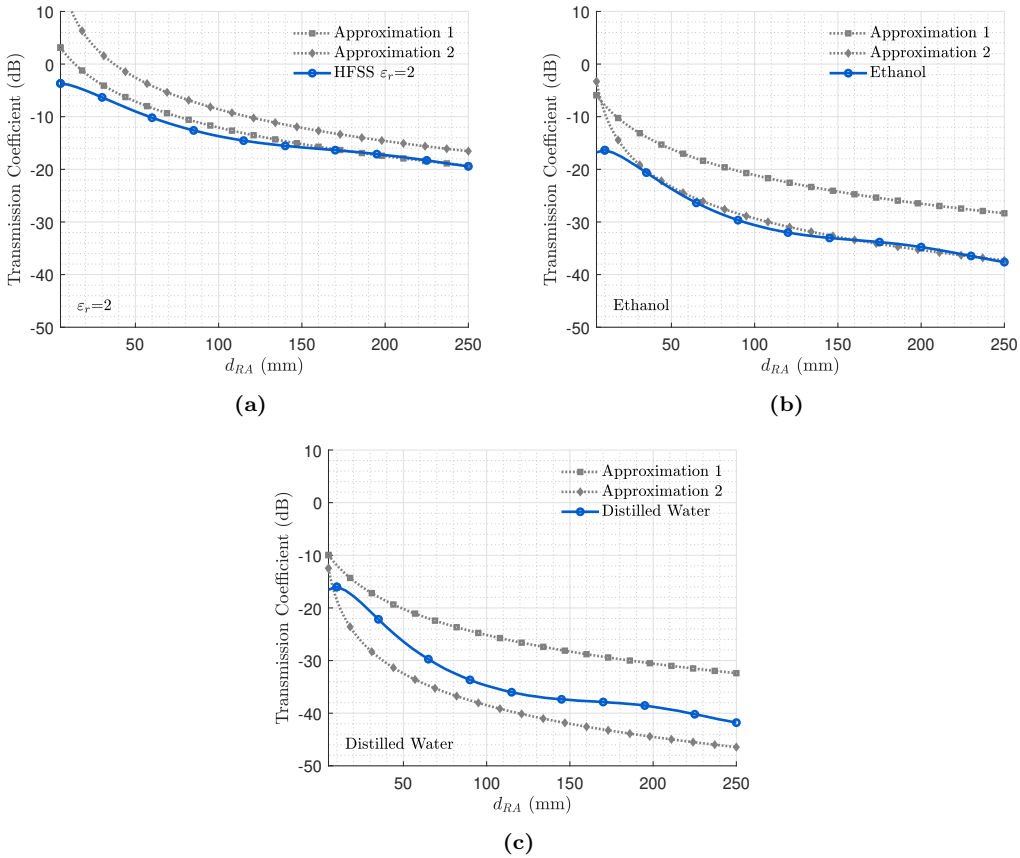

Figure 2.13: Transmission Coefficient between the RA and the AUT at 0.868 GHz obtained from HFSS, Approximation (2.5b) and Approximation (2.5c): **(a)** $\varepsilon_r^* = 2$, **(b)** $\varepsilon_r^* = 15.15 - j9.99$, Ethanol, and **(c)** $\varepsilon_r^* = 80.89 - j5.64$, Distilled Water.

Table 2.6: X-MAC Mechanical and Electrical Features.

Parameter	**Description**
MECHANICAL PARAMETERS	
Rotation Stages	19.6 N load capacity, 0.1° positioning accuracy and maximum rotation speed of 30°/*sec*.
Linear Stages	25 kg maximum load capacity, 0.05 mm precision accuracy and maximum speed of 250mm/sec.
ELECTRICAL PARAMETERS	
Radiation Absorbing Material	20 dB and 55dB reflection attenuation at 0.8 GHz and 50 GHz, respectively
Rotary Joints	DC to 50 GHz frequency range and connector type 2.4 mm.
RF Cables	DC to 50 GHz frequency range, connector type 2.4 mm Male and 5.64 dB/m attenuation at 50 GHz.
Operation Frequency	0.8 GHz to 50 GHz

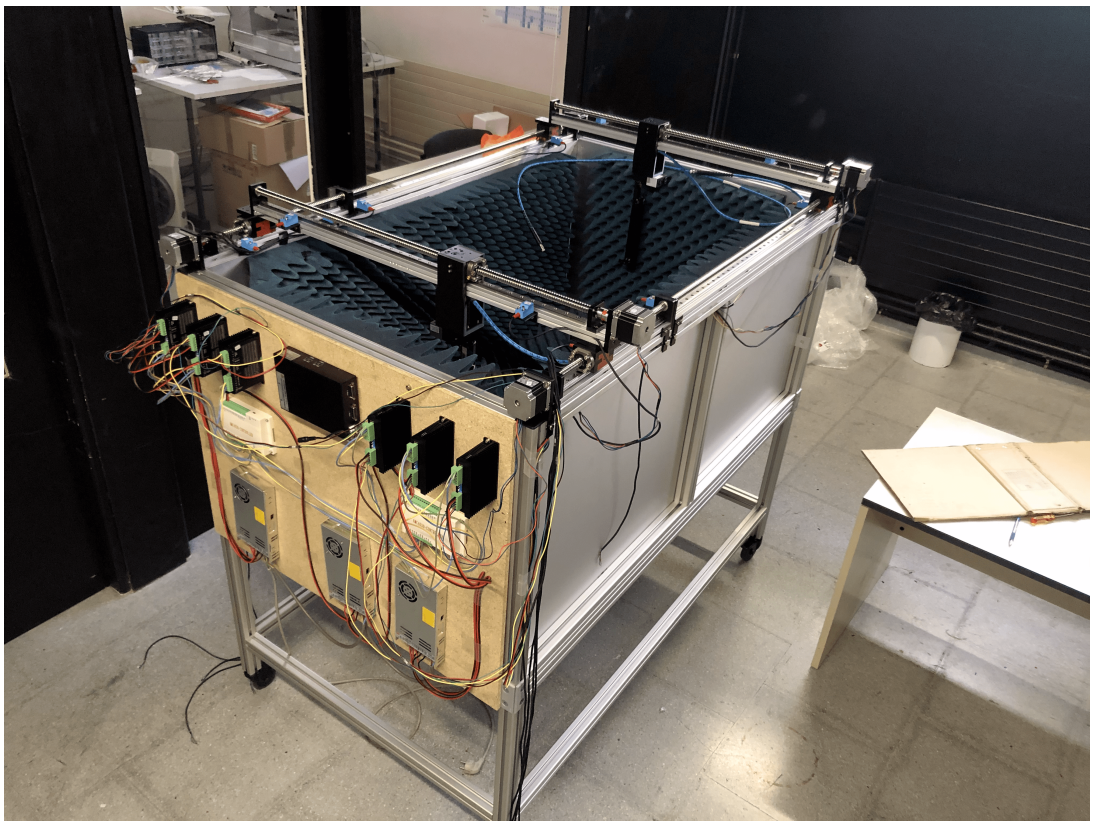

Figure 2.14: Manufactured X-Wave Miniaturized Anechoic Chamber.

CHAPTER 3

Wireless Sensor Design

The structure of this chapter has been conceived to tackle objective 4 defined in Chapter 1. In Section 3.1, the work published in [**GG-II**] describing the application of a wireless RFID temperature sensor for concrete setting monitoring, is presented. Section 3.2 discusses the results presented in [**GG-III**] and [**GG-VI**] for a resonance-based microwave technique for body implant sensing.

3.1 RFID Temperature Sensor for Concrete Setting Monitoring

3.1.1 Theoretical Introduction

The small-size low-cost RFID sensor for operation at 0.868 GHz presented in this section, has been designed to be embedded in concrete and to monitor its setting process. This work has been conducted in collaboration with WitekLab [58].

The operation principle is based on the known correlation between temperature peaks that occur in the concrete mixture and the evolution of the hydration process [24, 25]. The sensor is designed to sample the temperature and record a temperature log that can be wirelessly read be a commercial RFID reader. Due to its small size and low cost, these sensors can be embedded into the concrete while it is poured. As large changes in the dielectric constant and high losses are expected during the initial stages of concrete setting, one of the major sensor design challenges is that it should be able to properly operate and transmit the measured data while embedded in a lossy changing medium.

To this end, and based on the insights gained from [**GG-I**], [**GG-IV**], [**GG-V**] and [**GG-IX**], the RFID sensor has been designed as a T-match Bow Tie antenna wrapped around a PLA cylinder and covered using a PLA packaging to mitigate the effect of concrete's time changing dielectric properties on the antenna impedance coupling factor

(1.2). The sensor is based on the EM4325 Integrated Circuit that provides the RFID front end, data memory, and integrated temperature sensor [59].

The RFID wireless system to monitor the internal temperature of the concrete sample during the setting reaction is structured as depicted in the block diagram in Figure 3.1. The RFID sensor is inserted in the concrete mixture during the pouring stage. A commercial RFID reader formed by a circularly polarized patch antenna and a reader ID eNUR-10W from Nordic is placed outside the concrete. The RFID reader is software controlled to make systematic readings of the temperature registered by the previously embedded wireless sensor [60].

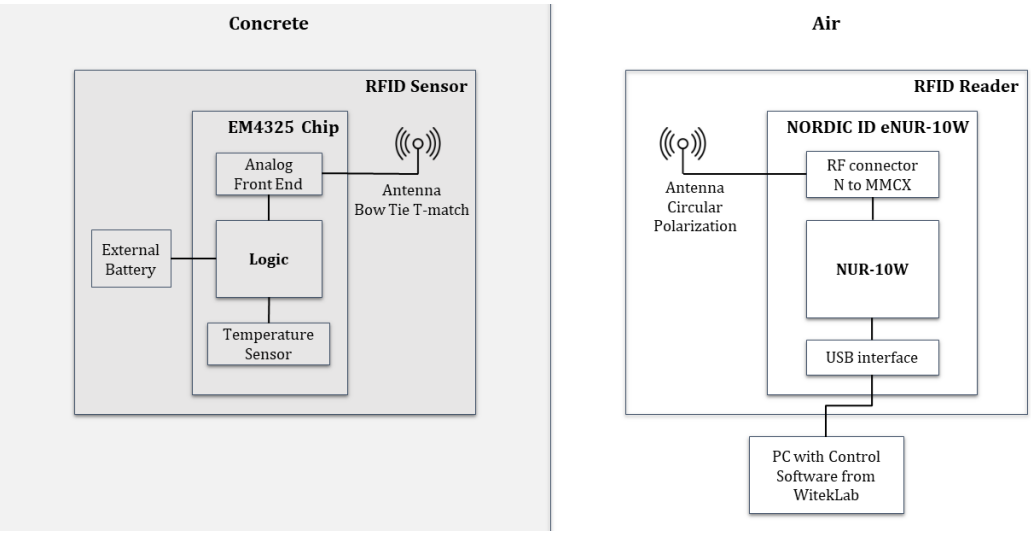

Figure 3.1: Block diagram of the RFID-based system for wireless temperature monitoring.

The propagation loss between a RFID sensor located inside a concrete structure, and a RFID reader placed outside is represented through (3.1). This expression, extracted from **[GG-VII]**, has been conceived from the classical approximation for free-space spherical wave propagation, considering that there are several propagation media with relative permittivities much higher than air in the propagation path between the receiving and transmitting antenna.

$$\frac{P_R}{P_T} = -20\log(\frac{4\pi d_{air}}{\lambda_{air}}) - 20\log(\frac{4\pi d_{MUT}}{\lambda_{MUT}}) - L_{MUT} + e_r - L_{CP} \tag{3.1}$$

In (3.1), the first two terms account for the free-space spherical wave propagation in air ($L_0(dB)$) and inside the embedding medium (concrete) ($L_{0MUT}(dB)$), respectively. L_{MUT} represents losses due to the ohmic attenuation of concrete, e_r is the reflection efficiency (computed according to [35]) and it accounts for the losses at the interface between both media, and L_{CP} are the circular to linear polarization losses.

3.1.2 Main Results

The proposed RFID sensor is represented in Figure 3.2. For the case of a bow tie antenna (electric antenna) matched to the rest of the electronics by means of a T-match structure, electric current densities are higher in the region closer to the feeding

point. Therefore, the T-match section of the antenna, if exposed to the embedding medium, would be more susceptible to its complex permittivity variations than the bow tie section would be. Hence, a "Front Cover" (see Figure 3.2) placed on top of the T-match, plays the role of the "packaging" described in Section 2.2.

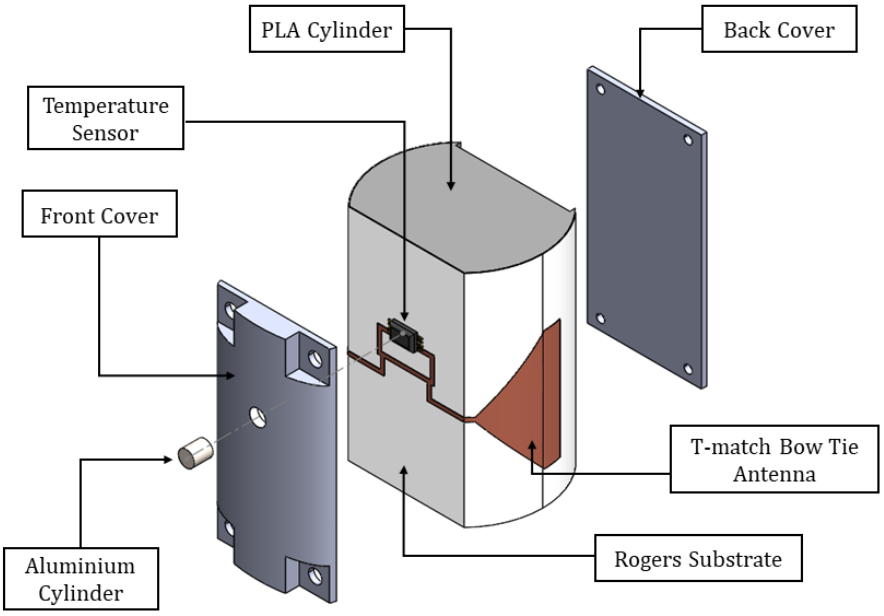

Figure 3.2: Proposed wrapped RFID sensor with a T-match Bow Tie antenna.

The results included in Figure 3.3, obtained using CST Microwave Studio, represent the Impedance Coupling Factor (1.2) of the RFID sensor for real part relative permittivities ranging between 4 and 18 (this corresponds to the ε'_r variation experienced by concrete during the setting reaction) at 0.868 GHz. Despite the changes produced in the antenna impedance as consequence of the relative permittivity variations in the embedding medium, the ICF is always above 0.4 for the expected dielectric permittivity evolution of the concrete sample.

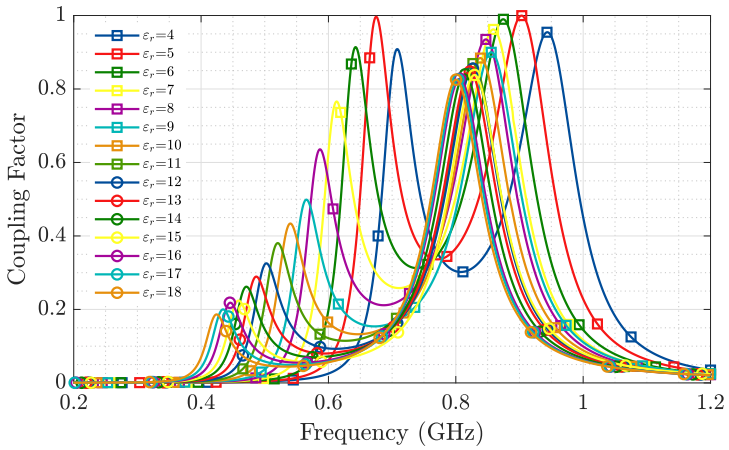

Figure 3.3: Antenna impedance coupling factor between the wrapped bow tie T-match antenna and the RFID-IC for ε'_r between 4 and 18.

Using the Debye-Γ model presented in [**GG-I**], it is possible to extract the ε^*_r values

corresponding to a concrete sample at 0.868 GHz at days 0.5, 1, 2, 4 and 8 of the setting reaction. Using those, all communication link parameters for the current scenario can be calculated (Tables 3.1 and 3.2). The radiation efficiency e_{rad} in Table 3.1 represents the ratio of the power radiated over total input power, and it has been obtained from CST. The parameter $L_{TMUT}(dB)$ in Table 3.2 accounts for the total propagation loss in the embedding medium ($L_{MUT}(dB) + L_{0MUT}(dB)$).

Table 3.1: RFID communication link parameters.

Parameter	Value	Description
P_R	-31 dBm	Sensitivity of the EM4325 chip.
P_T	30 dBm	Output Power of the Nordic eNUR reader.
G_T	9 dBi	Gain of the RFID Reader Antenna.
D_R	2.95 dBi	Directivity of the RFID Sensor Antenna.
e_{rad}	0.4	Radiation Efficiency of the RFID Sensor Antenna.
d_{MUT}	0.15 m, 0.02 m	Propagation distance inside concrete medium.
λ_{Air}	0.345 m	Wavelength in Free Space ($\varepsilon_r = 1$).
L_{CP}	3 dB	Polarization Missmatch Losses.

Table 3.2: Concrete propagation parameters for $d_{MUT} = 0.15m$ and $0.02m$.

Parameter	Day 0.5	Day 1	Day 2	Day 4	Day 8
ε_r	16.8 - j10	15.5 - j9.8	15 - j8.9	14.2 - j6.2	13.7- j5.7
λ_r (m)	0.084	0.088	0.089	0.092	0.093
α_{MUT}(dB/cm)	1.95	1.6	1.5	1.3	1.19
L_{MUT}(dB) (0.15m / 0.02m)	29.25/3.9	24/3.2	22.5/3	19.5/2.6	17.85/2.38
L_{0MUT}(dB) (0.15m / 0.02m)	27.02/9.52	26.62/9.12	26.52/9.02	26.23/8.73	26.14/8.64
L_{TMUT}(dB) (0.15m / 0.02m)	56.27/13.42	50.62/12.32	49.02/12.02	45.73/11.33	43.99/11.02
e_r (dB)	-6.73	-6.43	-6.3	-6.09	-5.96

From Table 3.1, the dynamic range of the current scenario can be extracted (i.e. $68dB$), by considering the transmission power of the RFID reader (P_T), the sensitivity of the RFID sensor (P_R), and the gain of both transmitting and receiving antennas. The analytical results presented in Figure 3.4 represent the propagation loss in the considered scenario over distance in air (d_{air}) computed through equation (3.1). These provide an estimation of the maximum distance where the external RFID reader can be placed with respect to the concrete-air interface, by considering that the maximum propagation loss would correspond to the available dynamic range. Hence, at the beginning of the setting reaction, the reader should be placed no further than 10 cm from the medium interface, while at the eighth day of setting the mixture has dried enough that it is possible to place the reader over 1 m away from the embedding medium interface.

The manufactured prototype is depicted in Figure 3.5. In-field measurement of these prototypes were conducted at PRMOSA's (one of Spain's major concrete manufacturers) testing facilities (Figure 3.6) using a concrete sample equivalent to the one in [**GG-I**], poured in a series of wooden containers of dimensions 30 x 30 x 30 cm and 2 cm

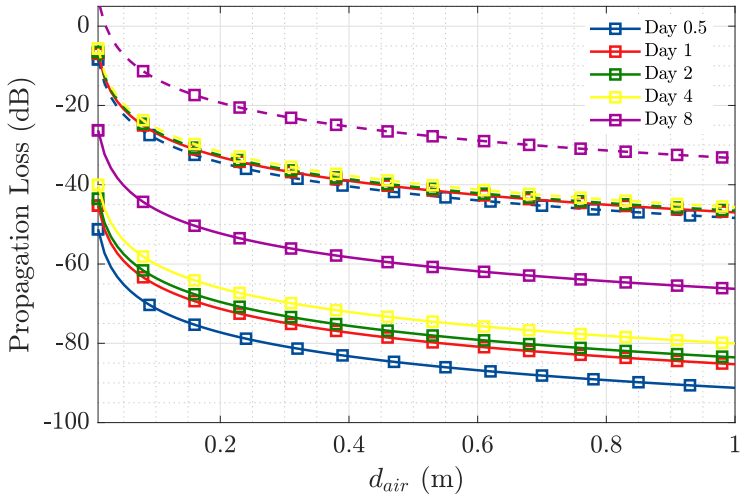

Figure 3.4: Dynamic range over d_{air} at 0.868 GHz, for days 0.5, 1, 2, 4, and 8 of concrete's setting reaction, for a sensor embedded 0.15 m (d_{MUT}) inside concrete (straight lines), and one embedded 0.02 m (dashed lines).

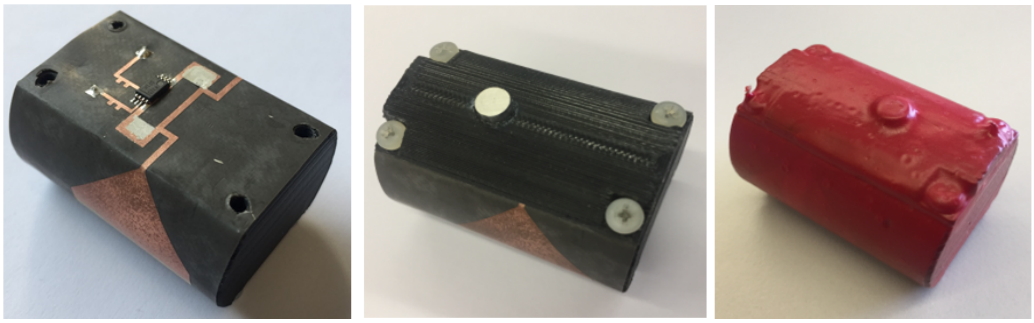

(a) **(b)** **(c)**

Figure 3.5: Manufactured RFID Temperature Sensor: (**a**) RFID sensor without packaging; (**b**) assembled sensor; and (**c**) sensor after protection layer.

thickness. The green cables in Figure 3.6 are thermocouples inserted right next to the sensors and attached to a data logger, to later correlate the temperature reading made by each one of the sensors to the one registered by the corresponding thermocouple.

The results presented in Figure 3.7 correspond to the temperature measured by one of the embedded sensors, compared to the one made by the corresponding thermocouple. The temperature measured by an additional thermocouple set to register the external temperature has also been included in Figure 3.7. From these results, it is possible to state that the temperature measurement made by the embedded sensor is an accurate representation of the actual temperature curve produced during the setting reaction of concrete. The oscillations present in all three temperature curves correspond to the variations produced during the day-night temperature cycle, as they take place in a 24 hour period. In the top right figure within Figure 3.7, the differential temperature for both the thermocouple and the RFID sensor placed inside the concrete sample has been represented. This is done by subtracting the room temperature effect, therefore mitigating the aforementioned day-night temperature cycle.

(a) (b)

Figure 3.6: In-field measurement at PROMSA: (**a**) Location of the embedded RFID sensors and (**b**) layout of the whole measurement scenario.

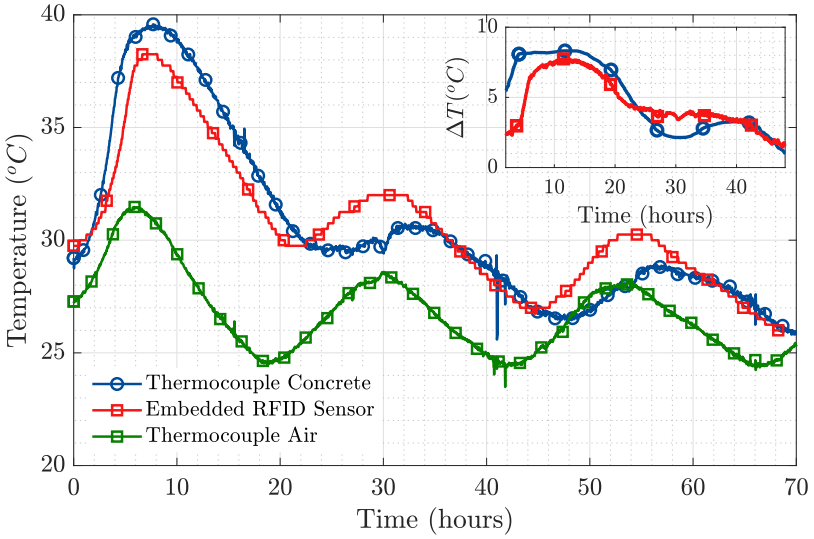

Figure 3.7: Temperature measured by the RFID sensor compared to temperature from the thermocouples. Top right Figure: Differential temperature inside concrete, removing the effect of room temperature.

The results of the peak temperature values achieved during the first hours of the hydration reaction in Figure 3.7, are in good agreement with those presented by [32,33] obtained using semi-embedded T-tag RFID sensors and also validated using thermocouples. The presented RFID sensor has also proven to remain well matched throughout the variations produced in the dielectric properties of the medium (validating the results presented in Figure 3.3 for the antenna Impedance Coupling Factor) and not interfering with the evolution of the setting process as it is fully wireless.

The good agreement between the temperature read obtained with the thermocouples and that obtained with the RFID sensor, and specially the fact that it was possible to maintain a stable communication link between the embedded sensor and the external reader, are proof of the feasibility of transmitting a microwave signal in this kind of scenario without it being interfered by the attenuation and changing dielectric properties

inherent of cement-based materials.

3.2 Biological Implant Microwave Sensing

3.2.1 Theoretical Introduction

The resonance-based monitoring technique presented in [**GG-III**] permits to sense devices and prostheses implanted inside the human body by using microwave wireless inspection. These results have been obtained as part of a collaboration with S. Amorós and the Research Institute German Trias i Pujol.

These devices, despite their different geometries and composition, have in common dimensions up to some tens of millimeters that when in a biological environment with permittivities around the 50s may have an electromagnetic resonance into the UHF (0.3 GHz to 3.0 GHz) frequency band.

The change of some of these implanted devices (IDs) characteristics over time, may compromise their functionality. These changes may be triggered by wear corrosion, breakdowns, adherence of biological tissues, etc. This would most likely result in operational malfunctioning and, in most cases, a change in its electrical parameters, which will result in a change of its resonant frequency. UHF signals with a convenient dynamic range and appropriate antenna probes are able to penetrate some tens of cm into the body and interact with those devices giving a scattering response that may be strongly influenced by the electrical resonance of the ID, therefore, allowing to monitor the state of the device.

In [**GG-III**], it is proposed to use implants as signal scattering devices and to detect any physical variation produced in the implant based on the corresponding variation of its scattering signature. This technique is able to extract the signature contained in the resonance frequency of the backscattered signal produced by the target device. This frequency depends on the electrical length of the device and may be used to detect, position and monitor changes in devices having electrical dimensions in the range of cm and depths of several centimetres.

The generic scenario supporting the resonance-based monitoring principle is presented in Figure 3.8. The ID is modeled as a generic electric dipole-based antenna. The scenario consists on a bistatic geometry with the transmitting (Tx) and receiving (Rx) probe antennas represented by the two dielectrically filled enlarged gap ridged horn (EGRH) antennas from [**GG-VIII**], and the ID is represented as a cylindrical object of length l_{ID}, located at a distance $\vec{r}_{TD}$ and $\vec{r}_{RD}$ from Tx and Rx probes respectively, all of it immersed into a dielectric medium of permittivity $\varepsilon_r^*(r)$ supposed to be low frequency dispersive in the range of the ID resonance. $P_T = |a_T|^2$ and $P_R = |b_R|^2$ are the transmitted and received power into the Tx and Rx respectively, Z_{in}^{ID} is the impedance of the ID when fed into a virtual port, and Z_{LD}^{ID} is a virtual impedance loading the device's port, that will model the operational state of the ID.

In a complex scenario, as those found in real situations, far-field conditions and homogeneous-space propagation do not meet, and the conventional radar formulation

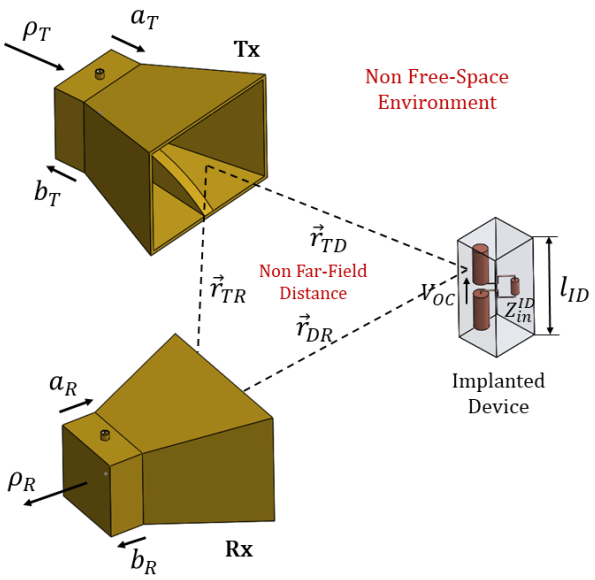

Figure 3.8: General Scenario.

is not applicable. In consequence, an approach based on the reciprocity theorem is needed [61]. The signal b_R measured into the receiving antenna may be expressed as equation (3.2) [62]. Where V_{OC}^{TD} and V_{OC}^{RD} are the open-ended circuit voltages at the port of the ID when illuminated by the Tx or Rx (reciprocity-based) antennas that may respectively be expressed as the product of the incident field E_{inc}^{TD} and E_{inc}^{RD} into the ID produced by the Tx and Rx and the ID effective high (h_{eff}).

$$\begin{aligned}\rho_{TR}^{ID} = \frac{b_R}{a_R} &= \frac{V_{OC}^{TD} V_{OC}^{RD}}{2P_T} \frac{1}{Z_{in}^{ID} + Z_{LD}^{ID}} \\ &= \frac{h_{eff}^2 E_{inc}^{TD} E_{inc}^{RD}}{2P_T} \frac{1}{Z_{in}^{ID} + Z_{LD}^{ID}}\end{aligned} \tag{3.2}$$

For the proof of concept of the principle we will consider a cylindrical electric dipole (thin conducting cylinder) of length l_{ID}, with its first resonant frequency (half wave dipole) at f_{res}^{ID}. The input impedance Z_{in}^{ID} may be approached, provided that the Tx/Rx antennas are significantly distant and/or the medium has a certain amount of loss (as it would be the case for most of the media of interest), by its self-impedance Z_{11}^{ID}. It is then possible to express the self-impedance of the electric dipole immersed into a medium of permittivity ε_r^* at a frequency f around its resonance frequency (f_{res}^{ID}), as [63]:

$$Z_{in}^{ID} \cong Z_{11}^{ID} = \left(73 + j43 \frac{\frac{f l_{ID} \sqrt{\varepsilon_r^*}}{c_0} - 0.45}{0.05}\right) \Omega \tag{3.3}$$

where c_0 is the speed of light in vacuum, and for which $Z_{in}^{ID} = 73 + j0$ at $l_{ID} = 0.475\lambda_e$ (i.e. the resonance frequency), where a minimum into the input impedance is obtained. Substituting (3.3) into (3.2) we may then calculate the frequency response of

the system, $\rho_{TR}^{ID}(f)$ for which a resonant maximum is obtained at the resonance, f_{res}^{ID}. The representation of this frequency response will give us the necessary information to diagnose the actual state of the resonance and, in consequence, the state of the implant.

As a first analytic approach, a cylindrical implant with a length $l_{ID} = 20$ mm and distances $r_{TD} = r_{RD} = r_{TR} = r_{TRD} = 50$ mm into a uniform medium of permittivity $\varepsilon_r^* = 50$ with a frequency span from 0.3 to 1.2 GHz is considered. In this example, the Tx and Rx antennas are supposed to be broad-band biconical dipoles (with a radiation resistance $R_a^{TR} = 75\ \Omega$ and a broad flat frequency covering the range of the ID resonance f_{res}^{ID}), while the implant itself resonates at a frequency of 0.85 GHz. In this specific example, because the far-field equations may be used (uniform medium and far-field distances), the expression for $\rho_{TR}^{ID}(f)$ may be analytically written as:

$$\rho_{TR}^{ID} \cong -\frac{25 l_{ID}^2}{R_a^{TR}\varepsilon_r}\left(\frac{e^{-j21f(GHz)\sqrt{\varepsilon_r}r_{TRD}}}{r_{TRD}}\right)^2\left(\frac{1}{1+j\left(40f(GHz)\sqrt{\varepsilon_r}l_{ID}-5.3\right)}\right) \tag{3.4}$$

In a similar way ρ_{TR}^{DR}, the signal traveling directly from the Tx to the Rx that may be calculated with the Friis equation [35] into the homogeneous background medium.

Figure 3.9 represents the frequency response, between 0.3 and 1.2 GHz where a single resonance may be considered, of the Tx-ID-Rx system through the relation, $\rho_{TR}^{ID}(f)$, for two states: (a) short-circuited ($Z_{LD}^{ID} = 0.0$), where the ID is supposed to work properly as a 20 mm cylindrical continuous element, and (b) open-circuited ($Z_{LD}^{ID} = 1000$), where the ID is supposed to be broken in the middle as two shorter 10 mm elements in which the actual value of 10 mm represents the remaining structural backscattering.

For a real application, as it is seen in the next section, the measured magnitude will be the superposition of two signals: (a) the signal Tx-ID-Rx, with (b) the direct signal Tx-Rx, resulting into a differential pattern ($\rho_{TR}^{ID} - \rho_{TR}^{DR}$) in which resonance will appear as a minimum (Figure 3.9).

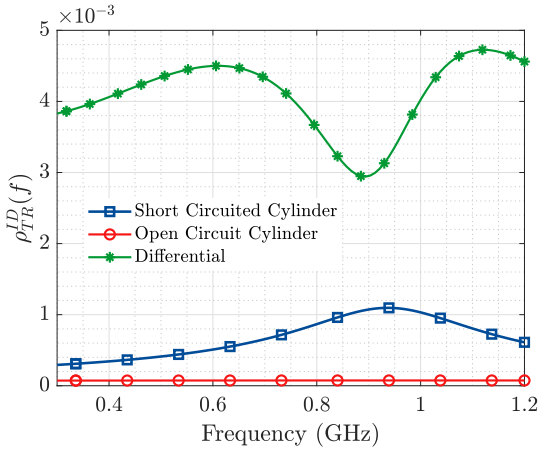

Figure 3.9: $\rho_{TR}^{ID}(f)$ of a 20 mm conducting cylinder representing the ID. The resonance is distinguished when the ID is fully operational (continuous object or $Z_{LD}^{ID} = 0$), from a non-operational state (breakdown or $Z_{LD}^{ID} = 1000$). The interferent differential signal is also reported.

3.2.2 Main Results

The technique described in the previous section for differential resonance sensing is now first tested through simulations conduced using CST Microwave Studio, then through *ex-vivo* experimental measurements with two enlarged gap ridged horn (EGRH) antennas from [**GG-VIII**] integrated in the set up in Figure 3.10 and filled with a phantom mimicking the permittivity of biological tissue ($\varepsilon'_r = 57, \tan\delta = 0.6$ at 0.8 GHz) [64] (results presented in [**GG-VI**]), and it is finally tested at an *in-vivo* scenario where swine animals were implanted with a coronary stent and the EGRH antennas in [**GG-VIII**] were used in a bistatic geometry equivalent to the one in Figure 3.8 (results presented in [**GG-III**]).

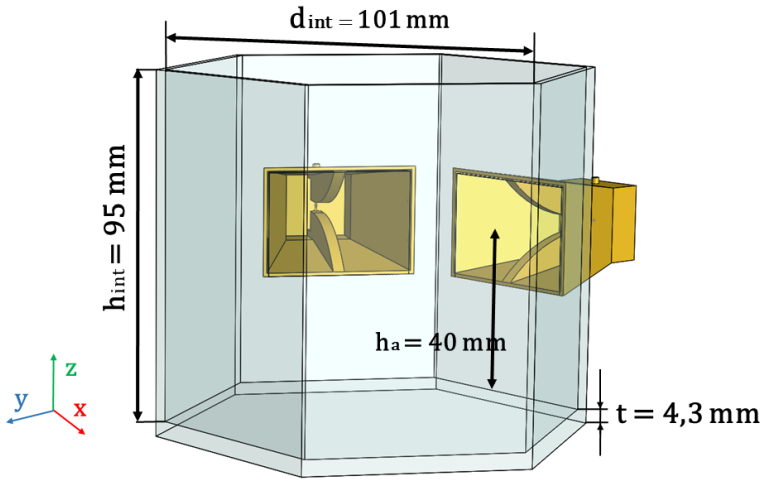

Figure 3.10: Schematic of the experimental set up for *ex-vivo* measurements.

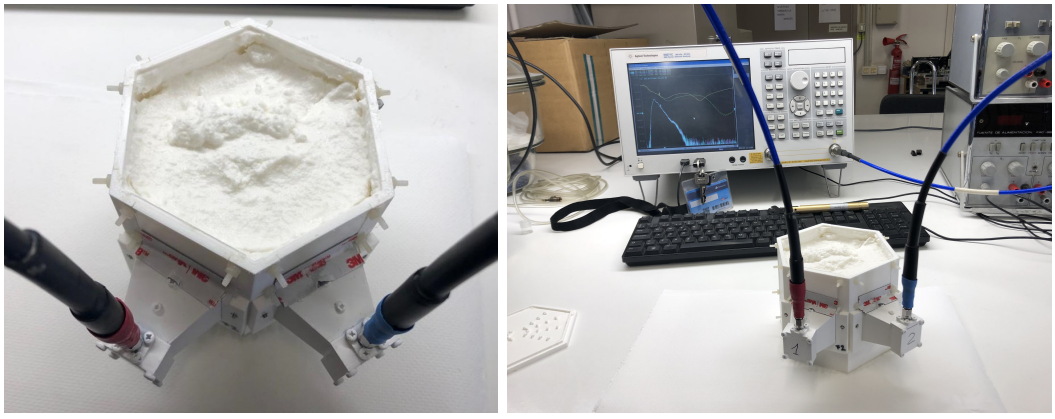

(a) **(b)**

Figure 3.11: *ex-vivo* measurement conducted at the laboratory.

In Figure 3.13 the simulated joint E-field distribution of both EGRH antennas, transverse to the aperture plane of the antennas, is represented at 0.8 GHz (estimated resonance frequency of the considered ID) for the case when no implant is present in the scenario (Figure 3.13a), and for an implanted device placed in front of the aperture of one of the antennas (Figure 3.13b), clearly showing the influence of the implant. We can also observe the importance of placing the probe antennas in such a way that the implant is located inside the crossing region of the field distribution radiated by both

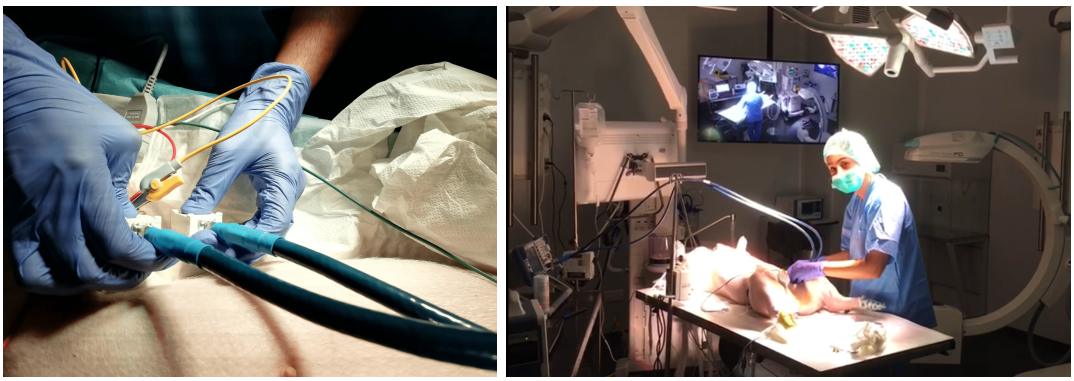

(a) (b)

Figure 3.12: *in-vivo* measurement at the Research Institute German Trias i Pujol.

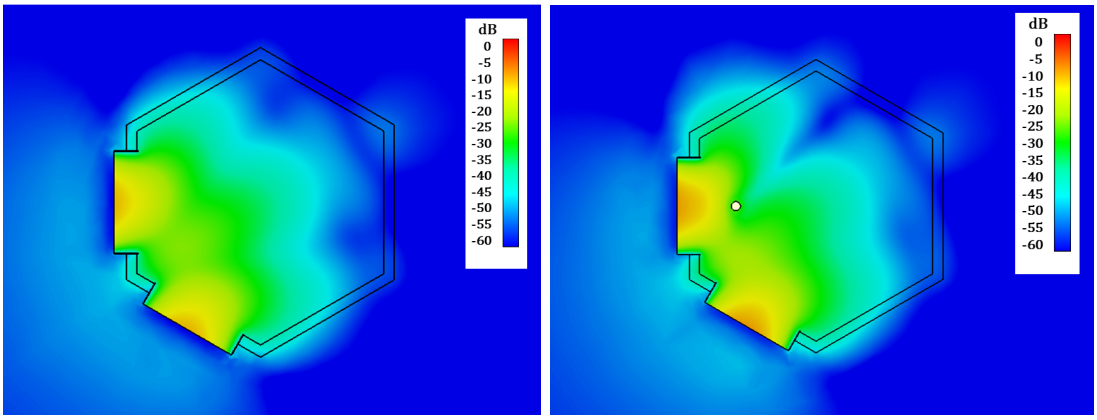

(a) (b)

Figure 3.13: Simulated joint E-field distribution into the transverse plane of the EGRH antennas at 0.8 GHz. (**a**) no ID, and (**b**) Frontal ID.

(Tx and Rx) antennas, which contributes to ID sensing.

The results corresponding to CST simulations and *ex-vivo* measurements have been obtained for an aluminum rod of 24 mm length and 4 mm diameter, parallel to the orientation of the E-field radiated by the EGRH antennas, and for different positions along the y axis (see Figure 3.10).

Figure 3.14a, 3.14c and 3.14e represent the magnitude of the transmission coefficient (S_{12}) in (dB) for CST simulation, *ex-vivo* measurement and *in-vivo* measurement, respectively. Whereas in Figure 3.14b, 3.14d and 3.14f, the results presented in the frequency domain have been time-converted applying the IFFT, and represented as a function of time for the CST simulation, the *ex-vivo* measurement and the *in-vivo* measurement, respectively.

In the representation of the S_{12} parameter for the baseline scenario (no ID), both in simulated and measured results, a steady slope with a maximum around 0.5 GHz is observed. When the ID is placed in front of the Tx and Rx, a modification in the S_{12} in the shape of a "resonance" is produced (Figure 3.14a, 3.14c and 3.14e). When the metallic rod is sequentially shifted, the frequency at which this "resonance" is produced and its depth variate as well (Figure 3.14a and 3.14c). The occurrence of this

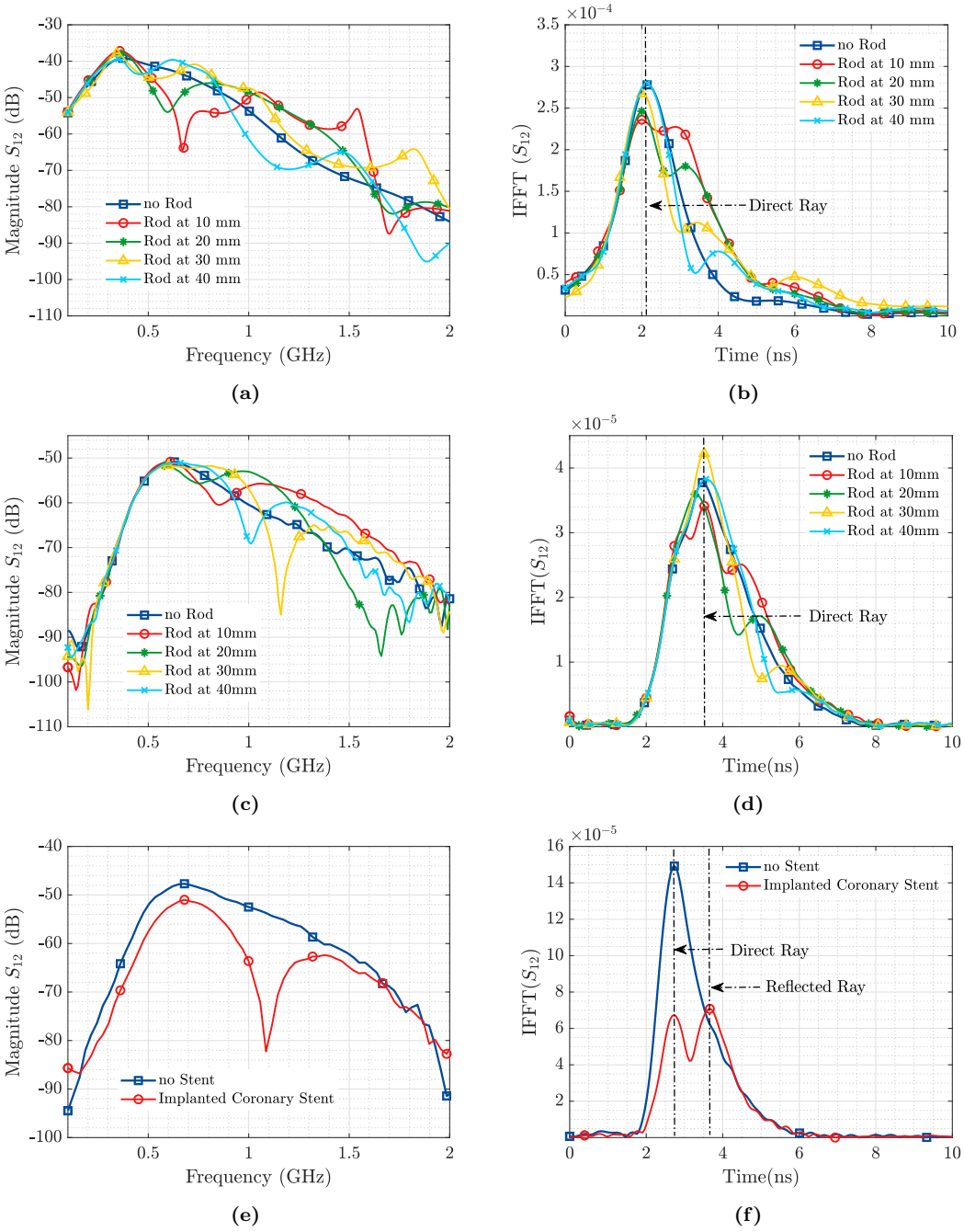

Figure 3.14: Transmission coefficient and Inverse Fourier Transform for: **(a)** and **(b)** CST Studio simulations, **(c)** and **(d)** *ex-vivo* measurements and **(e)** and **(f)** *in-vivo* measurements.

resonance indicates the capability to detect the presence of a resonant object implanted in a biological material. While the change of its frequency and depth triggered by a variation of its distance to the Tx and Rx antennas mean that it is also possible to locate the ID.

A more evident representation of the aforementioned phenomenon is observed when the transmission coefficient is time converted (Figure 3.14b, 3.14d and 3.14f). For the case where no ID is present in the scenario, it is possible to notice a single maximum in $IFFT(S_{12})$, which corresponds to the direct ray between the Tx and Rx EGRH

antennas. However, when the ID is introduced, two maximums are observed. The first one corresponds to the direct ray (from Tx to Rx), while the second one corresponds to a reflected ray generated by the presence of the resonant metallic implant. It is of interest to notice that all direct rays peak at the same time instant, meanwhile, the reflected rays achieve their maximum later (at a time corresponding with its actual position) as they are placed further from the Tx/Rx antennas (Figure 3.14b and 3.14d). The amplitude of the reflected ray decreases as the distance to the Tx/Rx antenna increases, as the amount of losses to cope with increase with the distance.

Regrading the *in-vivo* experiment, the propagation conditions present in this case, although similar, slightly variate with respect to the *ex-vivo* scenario. Before arriving to the implant, the signal transmitted by the Tx EGRH antenna must go through a layer of skin, fat and muscle, and then through the bone of the rib cage. This propagation conditions along with the lack of knowledge on the precise location and orientation of the stent, required a limited surface and angular scan. The flexibility and sensitivity of the technique allowed a proper disposition of the Tx/Rx probes which at the end permitted to obtain robust results.

When the exact position of an implanted device is known, then a variation produced in its scattering response will be linked to a change of the ID's characteristics (wear corrosion, breakdowns, adherence of other tissues, etc.). This can be further exploited for the benefit of medical diagnose of patients with medical implants.

CHAPTER 4

Conclusions and Future Work

The work conducted throughout this thesis has been mainly focused on shedding some light on some of the fundamental aspects to consider when designing wireless sensors intended for operation embedded in materials with high complex permittivity and high losses.

To that end, it has been demonstrated in Section 2.1 the importance of relaying on robust high accuracy measurement methods for the characterization of the dielectric properties of these materials. The specific example of measuring the dielectric properties of concrete based materials using a rectangular waveguide in transmission/reflection operation regime has been used to contrast these results with others where only reflection based methods or less accurate ones, had been employed.

The possibility of applying relaxation models, such as the Debye model, to frequency extend the complex permittivity measurement of granular materials, such as concrete or mortar, in scenarios where it is not feasible to conduct measurements at higher frequencies, has been validated.

For the specific case of concrete's dielectric properties, it has been observed that after the first week of the setting process, the electromagnetic properties exhibit a stable behaviour. Nevertheless, after this amount of time, it is still necessary to overcome 18 dB in ohmic loss attenuation only, to communicate with a device embedded 15 cm deep, while it requires 30 dB at the time instant when the maximum attenuation is produced (about 12 hours after pouring).

The results presented in [**GG-I**] are of great interest for wireless applications involving devices embedded in concrete. These data can be employed either to determine penetration depths or matching of the device under the effect of the dielectric properties of the surrounding medium. Furthermore, for those applications where it is a must being able to sustain a reliable and stable communication link with an embedded device since the beginning of the setting reaction of concrete, it is paramount to know the exact variations that take place on its relative complex permittivity, either to en-

sure good matching or to be able to adjust the transmission equation and, therefore, to withstand the peak produced in the ohmic loss attenuation during the first stages of the process.

As it is discussed in Section 2.2, the effect of medium losses (ε_r'') on antenna impedance match impacts mostly the antenna radiation efficiency (e_{rad}). This is because the radiation resistance of the antenna decreases considerably when exposed to medium losses as a large part of the antenna's resistance is actually expressed as loss resistance (R_l) instead. This phenomenon is most noticeable for the case of RFID antennas, as they typically have a very small radiation resistance. The use of a packaging layer has been studied and a basic packaging thickness of 0.1λ is recommended as an effective technique to isolate the antenna from the surrounding medium and hence mitigate its effect. This packaging also contributes to maximizing the amount of radiated power from the embedded device that reaches free space.

The particular case of dipole-like antennas small in terms of wavelength has been studied to validate the possibility of designing a proper packaging to minimize the antenna reactance changes due to changes in the dielectric medium. It has been shown that for a realistic RFID antenna embedded in different biological media the antenna reactance can be stabilized. Additionally, as the diameter of the packaging increases, the value tends to be more stable.

The specific geometry and size of this packaging plays a determinant role in the excitation of non-desired secondary modes above certain frequencies. The results presented in Section 2.2 provide insights on the frequencies at which these modes start to appear and how proper packaging selection may prevent this undesired behaviour.

Additionally, insights on optimal operation frequency for either shallow or deeply embedded sensors are provided considering the maximum power radiated into free space from an embedded device for different packaging sizes and embedding medium depths. These results can be used at design stage of wireless embedded sensors to derive information regarding optimal operation frequency, specially for the case of shallow devices. Link budget estimation is also feasible, once known the specific operation scenario and frequency.

In Section 2.3, a novel cost-effective miniaturized anechoic chamber has been presented as a suitable solution to conduct in-lab measurements of the manufactured prototypes operating embedded in the targeted medium.

The aforementioned recommendations, concerning the design of wireless devices for embedded operation, have been applied to two in-field experiments: one for a wireless RFID temperature sensor embedded in concrete, and the other one for the detection of resonant stents implanted in the coronary artery of swine animals using microwave probes.

The results presented in [**GG-II**] are proof of the possibility of employing wireless technology to remotely monitor physical and chemical processes produced during the setting reaction of concrete, using temperature measurements as a proxy for the evaluation of a hydration process that occurs during the setting of concrete. This information is of great use at constructions sites to reduce construction time, as well as for safety purposes such as building's structural strength monitoring.

The reading distances obtained during in-field measurements were in line with the propagation attenuation values employed for propagation loss over distance in air estimation. This is proof of the importance of having accurate available data to characterize the propagation conditions present in a given scenario.

Whereas in [**GG-III**], a novel technique for body implant sensing has been analytically presented and validated through simulations, experimental measurements of a phantom mimicking the dielectric properties of biological tissue and, finally, by conducting an *in-vivo* measurement on a coronary stent implanted in a swine animal. It has been possible to extract information regarding the presence and location of medical implants from the resonant scattering produced by the device itself, with no need to make any modifications in the implant. The resonance-based microwave technique with the EGRH antennas has detected implanted devices up to 4 cm deep measured with a general purpose laboratory instrument. This range could be extended to 10 cm (we should not find implanted devices placed much deeper in real human body exploration) with an enhanced SNR (Signal to Noise Ratio) produced with the adequate featured instrumentation.

As a summary, the results presented throughout this thesis attempt to transmit the following message: when faced with the challenge of designing a wireless sensor to work embedded in a high permittivity medium, (1) start by making sure you have good data on the medium's relative permittivity, or have it measured if you don't, (2) use a quick tool such as cylindrical or spherical wave expansions to obtain insights on the optimal operation frequency given a specific scenario and implantation depth, (3) using these tools, make sure that no undesired modes are being excited, (4) do not forget to use a packaging layer, which should be thicker or thinner depending on the particular dielectric properties of the medium, (5) make an assessment of the expected link budget, (6) you can now start evaluating your model in the electromagnetic simulation tool of your choice, and (7) making in-lab high accuracy measurements of your prototype where semi-real embedding medium conditions are represented is highly recommended before conducting any in-field tests.

4.1 Future Work

There are some open questions and research lines linked to the presented work worth of further investigation. Some of those are listed in this section:

- Although the method presented in [**GG-I**] to characterize the dielectric properties of granular materials such as concrete provides very accurate results, and by using the proposed Debye-Γ model it is possible to frequency extend these results and therefore overcome the narrowband constraint, this method may not be practical in circumstances where taking a sample of the medium is not feasible (i.e. in-field ε_r^* characterization). It would be quite useful a transmission/reflection based method with a probe like geometry, that while preserving the high accuracy of Tx/Rx methods, could be used in the field to get fast complex permittivity measurements.

- With respect to the presented miniaturized anechoic chamber (X-MAC), although

the entire mechanical layout has been completed at the time, and the fundamental stages of the automatized mechanical movement have been implemented, and some preliminary measurements have been conducting with very promising results, there is still some work ahead to fully integrate the automatic control of the X-MAC's mechanical movement and to create specific routines describing given measurement scenarios.

- A more accurate expression to describe the link equation between an embedded device and an external antenna, than the approximations presented in Section 2.3 should be provided. This expression, could be based on the reciprocity theorem presented by Lorentz in [65].

CHAPTER 5

Publications

Publication I

5.1 [GG-I] Debye Frequency-Extended waveguide Permittivity Extraction for High Complex Permittivity Materials: Concrete Setting Process Characterization

Publication: González-López, G., Blanch, S., Romeu, J., & Jofre, L. (2019). Debye frequency-extended waveguide permittivity extraction for high complex permittivity materials: Concrete setting process characterization. IEEE Transactions on Instrumentation and Measurement, 69(8), 5604-5613.

Publication II

5.2 [GG-II] Wireless Sensing of Concrete Setting Process

Publication: González-López, G., Romeu, J., Cairó, I., Segura, I., Ikumi, T., & Jofre-Roca, L. (2020). Wireless Sensing of Concrete Setting Process. Sensors, 20(20), 5965.

sensors

MDPI

Letter

Wireless Sensing of Concrete Setting Process

Giselle González-López [1,*], Jordi Romeu [1], Ignasi Cairó [2], Ignacio Segura [3,4], Tai Ikumi [3,4] and Lluis Jofre-Roca [1]

1 School of Telecommunication Engineering, Universitat Politècnica de Catalunya, 08034 Barcelona, Spain; romeu@tsc.upc.edu (J.R.); luis.jofre@upc.edu (L.J.-R.)
2 WitekLab, 08910 Badalona, Spain; ignasi@witeklab.com
3 Department of Civil and Environmental Engineering, Universitat Politècnica de Catalunya, 08034 Barcelona, Spain; ignacio.segura@upc.edu (I.S.); tai.ikumi@smartengineeringbcn.com (T.I.)
4 Smart Engineering, 08034 Barcelona, Spain
* Correspondence: giselle.gonzalez@upc.edu

Received: 16 September 2020; Accepted: 19 October 2020; Published: 21 October 2020

Abstract: An RFID-based wireless system to measure the evolution of the setting process of cement-based materials is presented in this paper. The system consists of a wireless RFID temperature sensor that works embedded in concrete, and an external RFID reader that communicates with the embedded sensor to extract the temperature measurement conducted by the embedded sensor. Temperature time evolution is a well known proxy to monitor the setting process of concrete. The RFID sensor consisting of an UWB Bow Tie antenna with central frequency 868 MHz, matched to the EM4325 temperature chip through a T-match structure for embedded operation inside concrete is fully characterized. Results for measurements of the full set up conducted in a real-scenario are provided.

Keywords: RFID; concrete setting; relative permittivity; embedded

1. Introduction

Concrete is the most widely used construction material in the world. Appropriate monitoring of its setting process is necessary to guarantee that it has reached the required structural strength. Having reliable procedures to assess the state of the setting process on-site and in a non-invasive way, can be helpful in speeding up the construction process through an accurate prediction of formwork stripping, post-tensioning, and opening pavement to traffic times. This is also true in the manufacturing of precast concrete structures in which demolding can be done once the setting process is advanced to the point that the structure can self-sustain and as a consequence molds can be reused at a higher pace and production can increase.

In [1], it is shown that the exothermic hydration process associated to the concrete setting causes temperature and also dielectric constant variations of the concrete mixture in the UHF (Ultra High Frequency) band. Monitoring the changes in the dielectric constant of the concrete mixtures has been proposed in [2] in a wired experimental set-up as a way to monitor the setting process. In [3,4], RFID (Radio Frequency Identification) based sensors have been demonstrated to measure chlorine ion concentration and humidity inside concrete as a means to monitor concrete corrosion. The potentiality of wireless coupled sensors has also been shown in [5,6] by embedding inside the concrete a strain sensor electromagnetically coupled to an external antenna, and in [7], RFID technology is used to couple a concrete-embedded strain gauge to an external reader to monitor 3-axis acceleration of concrete structures. Current systems, such as those in [8,9], employ passive RFID sensor T-tags to monitor the setting process of concrete. However, these systems present a poor performance at the beginning of the setting reaction of concrete, where substantial changes in the dielectric properties of the material are produced, as consequence of their probe-like based design.

In this paper a small-size low-cost RFID sensor designed to be embedded into concrete to monitor the setting process is presented. The operation principle is based on the known correlation between temperature peaks that occur in the concrete mixture and the evolution of the hydration process. When cement, water, aggregate, and additives are mixed together, a significant heat increase occurs due to the exothermic process in the reaction between cement and water (hydration reaction), once the strong exothermic process is completed (1–3 h) the temperature decreases and stabilizes providing an estimation of the mechanical strength reached by the concrete sample. Hence, by measuring the temperature evolution of a concrete sample it is possible to assess the maturity and therefore the strength of a concrete sample throughout its setting process. The most significant temperature changes take place during the first 12 h of the reaction [10,11].

The sensor is designed to sample the temperature and record a temperature log that can be wireless read by a commercial RFID reader. The analysis of the temperature evolution provides an indication of the setting process of the concrete. Due to its small size and low cost, sensors can be embedded into the concrete while it is poured. Its data logging features allow an asynchronous reading of the sensors. As shown in [1], in the initial stages of the concrete setting large changes in its dielectric constant and high losses are expected. In consequence, one of major challenges is designing a sensor that is able to properly operate and transmit the measured data embedded in a heavily lossy changing medium. To this end a specific bow-tie broad band antenna conformed to a cylinder has been designed to offer both low-profile integration in the sensor and more stable operation in front of medium changes. The sensor is based on the EM4325 Integrated Circuit that provides the RFID front end, data memory, and integrated temperature sensor.

The paper is organized as follows: Section 2 contains a detailed description of the RFID-based wireless system for temperature monitoring, including details on the design of the RFID sensor for embedded operation at 868 MHz and the RFID reader, as well as analytical results for the propagation loss in the considered scenario. In Section 3, results corresponding to the in-field measurement have been included.

2. RFID-Based System for Wireless Temperature Monitoring

The RFID wireless system to monitor the internal temperature of concrete sample during the setting reaction is structured as depicted in the block diagram in Figure 1. During the pouring stage of concrete, the RFID sensors consisting of an EM4325-IC (Integrated Circuit) temperature sensor matched to a bow-tie broad band antenna and conformed around a 3D printed PLA structure with a cylindrical shape, are poured inside the concrete mixture as part of the aggregates. A commercial RFID reader formed by a circularly polarized patch antenna and a reader ID eNUR-10W from Nordic is placed outside the concrete. This RFID reader is software controlled to make systematic readings of the temperature registered by the wireless sensors previously placed inside the concrete sample. A detailed description of the main design features of the RFID sensor and reader, as well as an analytic study of the propagation path between the external antenna and embedded device, are provided in this section. The block diagram in Figure 1 illustrates the operation principle of the RFID system. Further technical information of the EM4325 chip and the NORDIC ID eNUR-10W reader can be found in [12,13], respectively.

2.1. Wireless RFID Temperature Sensor

When designing a RFID sensor to work embedded in a medium whose properties change over time, there are certain constrains that must be taken into account as they will have an impact on the performance of the device that cannot be neglected.

From an industrial point of view, it is desired to come up with a design that is as compact and small as possible. In the construction industry for example, robustness is a must, as a device embedded in a block of concrete has to withstand a tremendous amount of weight and pressure. Taking this into account, a thin planar design is quickly off the table, and a shift towards a more “rock-like” device is

preferred as it mimics the shape of aggregates already present in concrete mixtures. A considerable amount of water will be present at the first stages of the setting process of concrete, so it is important to assure that the device is waterproof to prevent damage on the electronics. Nevertheless, the main goal of this device is to monitor the temperature of the surrounding medium, which implies that the sensor must be exposed to the medium somehow for accurate temperature measurement. RFID tags, typically operate as passive devices, which means that they are powered by the RF energy transmitted from a reader. However when they incorporate "sensing" capabilities, working in battery operated mode generally provides more processing capabilities and higher reading range and reliability. The RFID sensor layout must be then designed in a way that simultaneously ensures compactness and robustness, isolation, and an accurate temperature measurement.

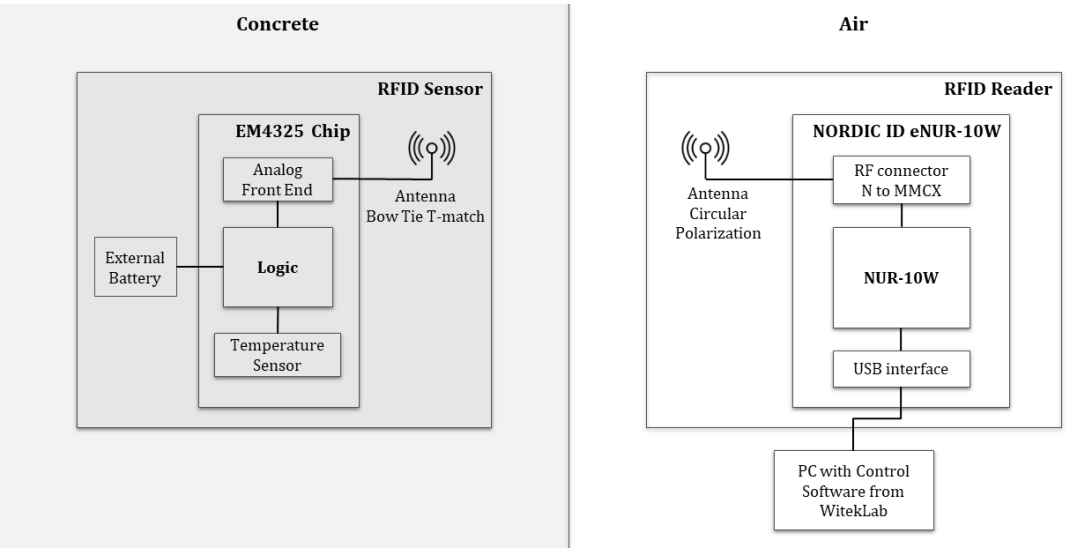

Figure 1. Block Diagram of the RFID-based system for wireless temperature monitoring.

The EM4325 RFID chip is a Radio Frequency Identification Integrated Circuit from EM Microelectronic that can be either battery powered or beam powered by RF (Radio Frequency) energy transmitted from a reader. In a Battery Assisted Passive (BAP) configuration, the EM4325 chip offers better sensitivity (−30 dBm) that translates into a superior reading range, compared to purely passive operation. When designing sensors intended to operate inside of lossy materials, as it is the case of concrete, maximizing the Dynamic Range (DR) between the transmitting and receiving antenna is of great interest to cope with the high propagation losses produced as a consequence of concrete's attenuation. This can be either achieved by increasing the transmission power, or as done in this case, by improving the sensitivity of the embedded passive device. The integrated temperature sensor supports temperatures in the range of −40 °C to +60 °C, which widely covers typical concrete temperatures reached during placement [12].

The EM4325 RFID chip does not include the capability of storing temperature measurements. Meaning that these should either be acquired on demand, or by installing a micro-controller. For the current application, the chip has been configured to operate as a radio-frequency front-end and to perform on demand temperature readings when requested by the external reader.

This chip, when configured in BAP operation mode, has an input impedance of $6.5 - j172\,\Omega$. In accordance, the RFID antenna conceived to operate matched to the EM4325 chip, is designed to provide a $6.5 + j172\,\Omega$ impedance at its input. To provide the required low resistance and high reactance input impedance, a T-match structure is employed between the bow-tie antenna and RFID chip [14,15].

In order to provide the aforementioned required compactness and robustness, the proposed design is printed on top of a bendable substrate of 0.125 mm thickness from Rogers ($\varepsilon_{rRT5880} = 2.2$).

This is then wrapped around the external walls of a semi-holed 3D printed PLA cylinder with a diamter of 30 mm. To provide a planar section to place the RFID chip and for isolation purposes, a vertical slice is made on the wall of the cylinder where both the EM4325 RFID chip and the T-match section of the antenna are placed. The removed section is then placed back on top, covering the electronics and isolating it from the surrounding medium. In this way, we are able to protect the electronics from the high water concentration present in the concrete mixture at the beginning of the setting reaction. An additional advantage of placing back on top of the T-match the removed PLA section, is that it enables a reduction of the T-match dimensions, as PLA's relative permittivity is higher than air's ($\varepsilon_{rPLA} = 2.5$), hence contributing to the compactness of the sensor. A 3V battery is placed inside the PLA cylinder, connected to the RFID chip through biasing lines, for BAP operation. The proposed RFID sensor is represented in Figure 2.

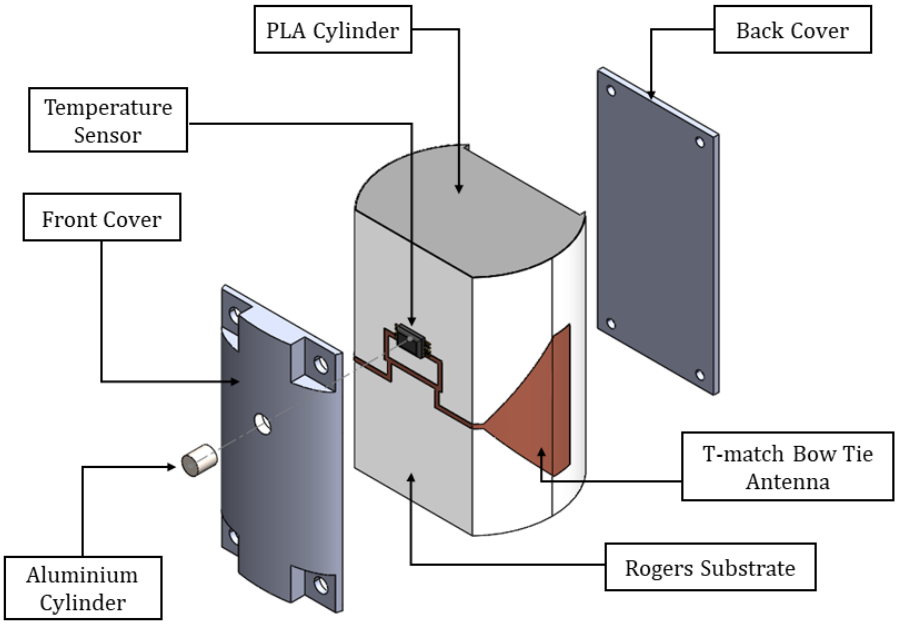

Figure 2. Wrapped RFID antenna. Bow tie with T-match.

An important factor when assessing the performance of the antenna is the Impedance Coupling Factor (ICF), computed as:

$$ICF = \frac{4Re(Z_a)Re(Z_{chip})}{\left(Re(Z_a) + Re(Z_{chip})\right)^2 + \left(Im(Z_a) + Im(Z_{chip})\right)^2}. \quad (1)$$

where Z_a is the antenna impedance and Z_{chip} is the impedance of the RFID chip, $6.5 - j172\,\Omega$ in this case. The Impedance Coupling Factor measures the fraction of power that is effectively transferred from the antenna to the RFID chip (and vice versa), and the design goal is to obtain a value close to one.

Figure 3 represents the the behavior of the proposed T-match bow-tie antenna in terms of input impedance and Coupling Factor, when placed in the embedding scenario. These results have been obtained through EM (Electromagnetic) simulations using CST Microwave Studio, considering the nominal value for the embedding medium's relative permittivity $\varepsilon_r = 6 - j0.36$ at 0.868 GHz.

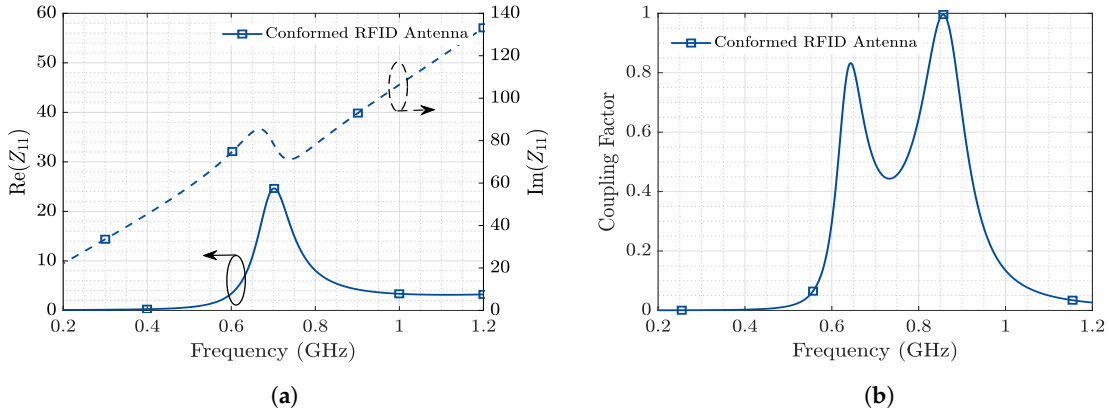

(**a**) (**b**)

Figure 3. Antenna parameters: (**a**) Input impedance. Re(Z_{11}) left vertical axis and Im(Z_{11}) right vertical axis and (**b**) impedance coupling factor.

It is known from [1] that the real part of the relative permittivity of concrete throughout the setting reaction varies exhibiting maximum values around $\varepsilon_r' = 18$ at the beginning of the reaction and lowering to $\varepsilon_r' = 11$ by the eighth day of the process. With this phenomenon in mind, the Impedance Coupling Factor between the wrapped T-match bow-tie antenna and the RFID-IC has been evaluated for real part relative permittivities ranging between 4 and 18 (Figure 4).

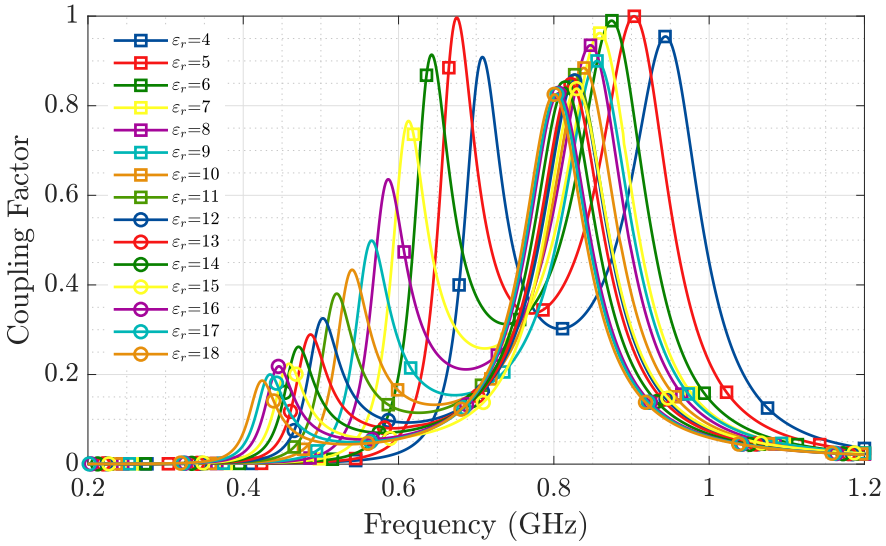

Figure 4. Antenna impedance coupling factor between the wrapped bow tie T-match antenna and the RFID-IC for ε_r between 4 and 18.

Figure 4 shows that at the operation frequency of 868 MHz, despite the changes produced in the sensor's antenna impedance as a consequence of the permittivity variations in the embedding medium, the Impedance Coupling Factor is above 0.4 for the expected dielectric permittivity evolution of the concrete sample throughout its setting process.

To enable the temperature sensing capability of the chip, a small hole is drilled on the section of the cylinder that acts as a "cover" for the T-match and chip. This hole is placed right on top of the chip and has dimensions equivalent to those of the sensor. Then a small aluminum cylinder is placed right on top of the temperature sensor (Figure 5b). One face of the aluminum cylinder is left exposed to the external medium while the other one is laying on the surface of the chip where a thermal conductive paste is applied in advance. The walls of this aluminum cylinder are glued to the cover to ensure fixation. Aluminum's good thermal conductivity makes it a suitable choice to act as an interface between the temperature sensor and embedding medium.

To assure that the whole device is completely isolated from the surrounding medium, the sensor is dipped in a liquid solution of PlastiDip and an air-dry rubber solution is applied to provide at the same time for protection and isolation to the RFID sensor. Figure 5 displays the final manufactured prototype. The main technical features of the proposed RFID temperature sensor are summarized in Table 1.

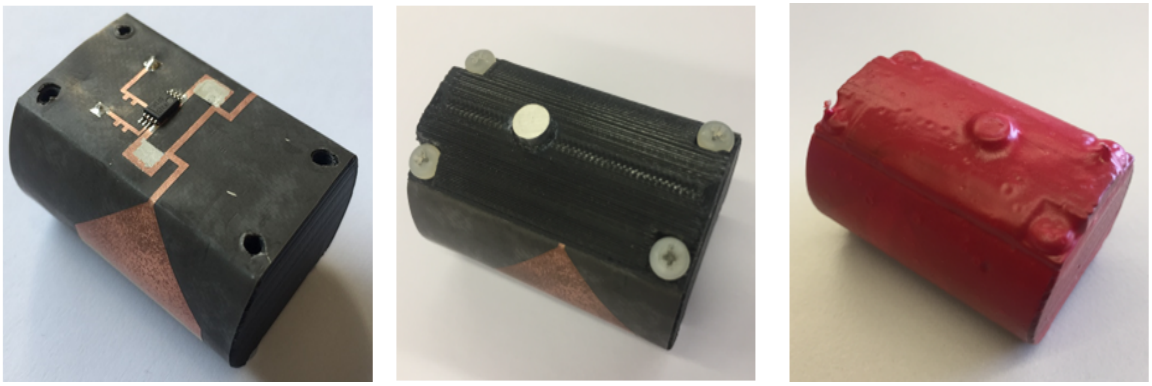

(**a**) (**b**) (**c**)

Figure 5. Manufactured RFID Temperature Sensor: (**a**) RFID sensor without cover; (**b**) assembled sensor; and (**c**) sensor after protection layer.

Table 1. Technical features of the RFID temperature sensor.

Parameter	Value	Description
Dimensions	41.2 mm × 30 mm	Height × Diameter of the RFID sensor.
Volume	0.0172 m^3	Volume of the RFID sensor.
Weight	23 g	Weight of the RFID sensor.
Temperature range	−40 °C to +60 °C	Temperature range of the RFID sensor.
Temperature Accuracy	±1 °C	Temperature accuracy of the EM4325 chip.
Z_{EM4325}	$6.5 - j172\,\Omega$	Input impedance of the EM4325 chip in BAP mode.
Antenna Radiation Pattern	Dipole-like (Omnidirectional)	Shape of the Bow Tie T-match antenna radiation pattern in azimuth.
Device Consumption	15.9 µW	Power consumption per reading of the EM4325 RFD chip.

2.2. RFID Reader

The Nordic ID eNUR-10W reader Figure 6a is one of Nordic ID modules for embedded RFID solutions. It is a cost-effective alternative to both fixed and high-end mobile RFID readers with multiple antennas. It is available as a Surface-Mount Device (SMD) component, or mounted on a PCB (Printed Circuit Board) for easier integration. The frequency of operation ranges from 865.6 MHz to 867.6 MHz in Europe, complying with the regulations from the European Telecommunications Standards Institute (ETSI). Regarding power consumption, this reader has an operating power of 4.3 W, and the typical supply voltage is 3.6 VDC, even though it admits voltages from 3.4 to 5.5 VDC at its input. The output power is 30 dBm, and it is adjustable in 1dB steps [13].

The patch antenna connected to the Nordic eNUR reader has a 9 dBi gain and a bandwidth ranging from 840 MHz to 960 MHz (Figure 6b). It has circular polarization, which introduces a loss due to a polarization mismatch of 3 dB as the antenna of the RFID tag has linear polarization. However, due to the random placement of the sensor during the pouring process using a circular polarized reader antenna helps prevent miss-detection due to high polarization losses that could occur in the case of using a linear polarized antenna.

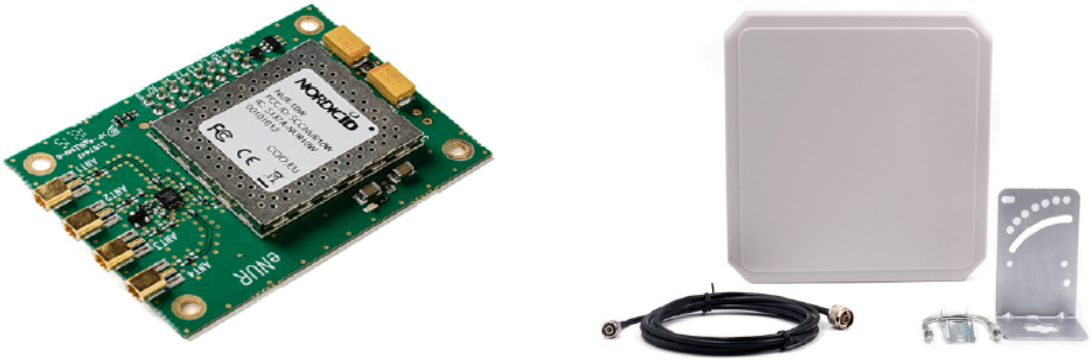

(**a**) (**b**)

Figure 6. RFID Reader: (**a**) Nordic ID eNUR RFID reader and (**b**) antenna of the eNUR reader.

2.3. Monitoring Software

The software in charge of establishing, controlling, and monitoring communication between the reader and RFID sensor has been developed by WiTekLab following Nordic ID semiconductors' recommendations for the development of software solutions for their RFID Embedded Reader Modules.

When the reader is connected to the computer and powered on, the control software scans for tags within the reading distance of the RFD reader, and displays parameters such as tag configuration, sensor data, and current temperature. As the EM4325 sensor does not have the capability of storing temperature measurements, the software tracks the temperature readings of a given tag, and stores it on a CSV file in the computer.

2.4. Propagation Loss between the RFID Reader and the Embedded RFID Sensor

The propagation loss between a RFID sensor located inside a concrete structure, and a RFID reader placed outside is represented through Equation (2). This expression, extracted from [16], has been conceived from the classical approximation for free-space spherical wave propagation, considering that there are several propagation media with relative permitivities much higher than air in the propagation path between the receiving and transmitting antenna:

$$\frac{P_R}{P_T} = -20\log\left(\frac{4\pi d_{air}}{\lambda_{air}}\right) - 20\log\left(\frac{4\pi d_{MUT}}{\lambda_{MUT}}\right) - L_{MUT} + e_r - L_{CP} \quad (2)$$

In (2), the first two terms account for the free-space spherical wave propagation in air ($L_0(dB)$) and inside the embedding medium (concrete) ($L_{0MUT}(dB)$), respectively. L_{MUT} represents losses due to the attenuation of concrete, e_r is the reflection efficiency (computed according to [14]) and it accounts for the losses at the interface between the mediums, and L_{CP} are the circular to linear polarization losses.

We have extracted from [1] the relative permittivity values measured at 868 MHz for a concrete sample at days 0.5, 1, 2, 4, and 8 of the setting reaction. Tables 2 and 3 summarize all communication link parameters, while Figure 7 represents the propagation loss in the considered scenario over distance d_{air} computed through Equation (2). The radiation efficiency (e_{rad}) in Table 2, has been obtained from the simulations conducted in CST of the proposed RFID sensor. This parameter represents the ratio of the power radiated over the total input power [14]. The parameter L_{TMUT}(dB) in Table 3 accounts for the total propagation loss in the embedding medium (L_{MUT}(dB) + L_{0MUT}(dB)).

From Table 2, we can extract that the dynamic range of the current scenario, considering the transmission power of the RFID reader (P_T), the sensitivity of the RFID sensor (P_R), and the gain of both transmitting and receiving antennas, is of −68dB. The analytical results presented in Figure 7 provide an estimation of the maximum distance where the external RFID reader can be placed with respect to the interface with the concrete medium, considering that the maximum propagation loss

would correspond to the available dynamic range. Hence, at the beginning of the setting reaction, the reader should be placed no further than 10 cm from the medium interface, while at the eighth day of setting the mixture has dried enough that it is possible to place the reader over 1 m away from the embedding medium's interface.

Table 2. RFID communication link parameters.

Parameter	Value	Description
P_R	−31 dBm	Sensitivity of the EM4325 chip.
P_T	30 dBm	Output Power of the Nordic eNUR reader.
G_T	9 dBi	Gain of the RFID Reader Antenna.
D_R	2.95 dBi	Directivity of the RFID Sensor Antenna.
e_{rad}	0.4	Radiation Efficiency of the RFID Sensor Antenna.
d_{MUT}	0.15 m, 0.02 m	Propagation distance inside concrete medium.
λ_{Air}	0.345 m	Wavelength in Free Space ($\varepsilon_r = 1$).
L_{CP}	3 dB	Polarization Missmatch Losses.

Table 3. Concrete propagation parameters for d_{MUT} = 0.15 m and 0.02 m

	ε_r	λ_r (m)	α_{MUT} (dB/cm)	L_{MUT} (dB) (0.15 m/0.02 m)	L_{0MUT} (dB) (0.15 m/0.02 m)	L_{TMUT} (dB) (0.15 m/0.02 m)	e_r (dB)
Day 0.5	16.8 − j10	0.084	1.95	29.25/3.9	27.02/9.52	56.27/13.42	−6.73
Day 1	15.5 − j9.8	0.088	1.6	24/3.2	26.62/9.12	50.62/12.32	−6.43
Day 2	15 − j8.9	0.089	1.5	22.5/3	26.52/9.02	49.02/12.02	−6.3
Day 4	14.2 − j6.2	0.092	1.3	19.5/2.6	26.23/8.73	45.73/11.33	−6.09
Day 8	13.7 − j5.7	0.093	1.19	17.85/2.38	26.14/8.64	43.99/11.02	−5.96

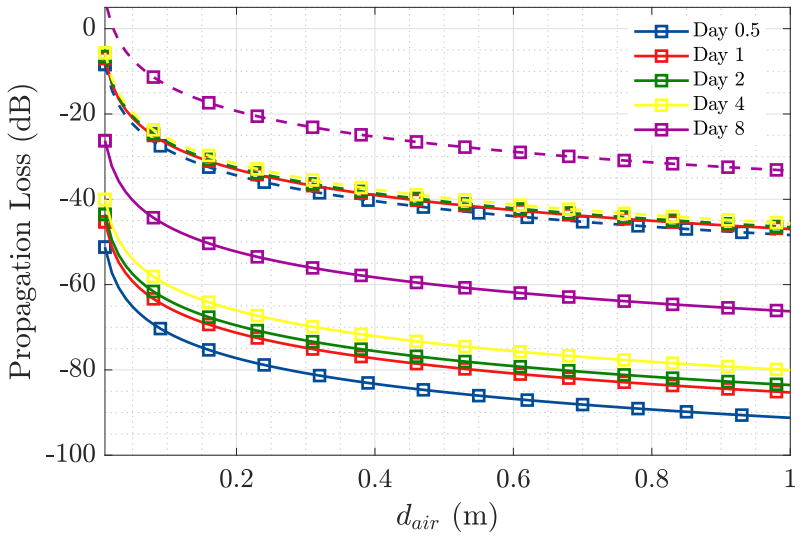

Figure 7. Dynamic range over d_{air} at 868 MHz, for days 0.5, 1, 2, 4, and 8 of concrete's setting reaction, for a sensor embedded 0.15 m (d_{MUT}) inside concrete (straight lines), and one embedded 0.02 m (dashed lines).

3. In-Field Measurements

The RFID temperature sensor characterized in the previous section (Figure 5), has been tested in a real life scenario at PROMSA's (one of Spain's major concrete manufacturers) testing facilities.

These facilities have been conceived to conduct controlled concrete manufacturing and sampling at room temperature. The concrete mixture employed in the measurement was prepared in the moment, tested for a previously predetermined consistency, and poured in a series of wooden containers of dimensions 30 × 30 × 30 cm and 2 cm thickness. The concrete mixture was the same as the one corresponding to the relative permittivity values mentioned in Table 3.

Figure 8 depicts the scenario of the in-field measurement. On the left (Figure 8a), it is possible to observe the RFID sensors before being fully convered by the concrete, placed one vertically and the other horizontally, to asses the viability of having linearly polarized embedded antennas, and a circularly polarized external antenna. The green cables are thermocouples inserted right next to the position of the sensors and attached to a data logger, to later compare the temperature reading made by each one of the sensors and correlate it to the one registered by the corresponding thermocouple. The whole layout of the measurement scenario can be observed in Figure 8b. The Nordic ID eNUR RFID reader is software controlled through a computer and it is connected to the patch antennas in the background, which are aimed towards the wooden containers where the RFID sensors are to be embedded.

(**a**) (**b**)

Figure 8. In-field measurement at PROMSA: (**a**) Location of the embedded RFID sensors and (**b**) layout of the whole measurement scenario.

A total of four sensors were placed inside two wooden containers. Two sensors were inserted at the center of each container (s1 and s2, d_{MUT} = 0.15 m), another one was placed at mid-height next to one corner (s3, d_{MUT} = 0.02 m), and the last one at the top corner of one of the containers (s4, d_{MUT} = 0.02 m).

At the beginning of the measurement, it was only possible to detect the sensor placed on the corner of the container (s4), by placing the reader's antenna right next to the interface with the container. The input power received at the time from this sensor was −62 dBm. Twenty-four hours later, the sensor located at mid-height next to the corner (s3) was also detected. At this time, the input power received from this sensor was −60 dBm, while the one received from s4 had risen to −50 dBm.

The sensors located at the center of the concrete containers (s1 and s2) were not detected during this test. We were able to retrieve them after concrete compression tests had been conducted, and it was possible to find out that the concrete's chemical corrosive effect had in fact damaged the isolating rubber covering the sensors, water had then leaked to the electronics and permanently damaged the sensor.

The results exhibited in Figure 9 correspond to the temperature measured by sensor s4, compared to the temperature measurement made by the corresponding thermocouple. The temperature measured by an additional thermocouple set to register the external temperature has also been included in Figure 9. From the results in Figure 9, we are able to say that the temperature measurement made by our embedded wireless RFID temperature sensor is a faithful representation of the actual temperature curve produced during the setting reaction of concrete. It is possible to notice

that the oscillations present in all three temperature curves correspond to the variations produced during the day-night temperature cycle, as they happened in a 24 h period. In the top right figure within Figure 9, the differential temperature for both the thermocouple and the RFID sensor placed inside the concrete sample have been represented. This is done by subtracting the room temperature effect, therefore mitigating the aforementioned day-night temperature cycle.

The results of the peak temperature values achieved during the first hours of the hydration reaction in Figure 9, are in good agreement with those presented by [8,9] obtained using semi-embedded T-tag RFID sensors and also validated using thermocouples. The presented RFID sensor has also proven to remain well matched throughout the variations produced in the dielectric properties of the medium (validating the results presented in Figure 4 for the antenna Impedance Coupling Factor) and not interfering with the evolution of the setting process as it is fully wireless.

The good agreement between the temperature read obtained with the thermocouples and that obtained with the RFID sensor, and the fact that it was possible to maintain a stable communication link between the embedded sensor and the external reader, are proof of the feasibility of transmitting a microwave signal in this kind of scenario without it being interfered by the attenuation and changing dielectric properties inherent of cement-based materials. These results are in agreement with those presented in [17], where the anti-interference performance of RFID systems has been studied for soil-, water-, and metal-covered sensors. Additionally, network based communication methods as those proposed in [18–20], can be a suitable solution in high interference scenarios.

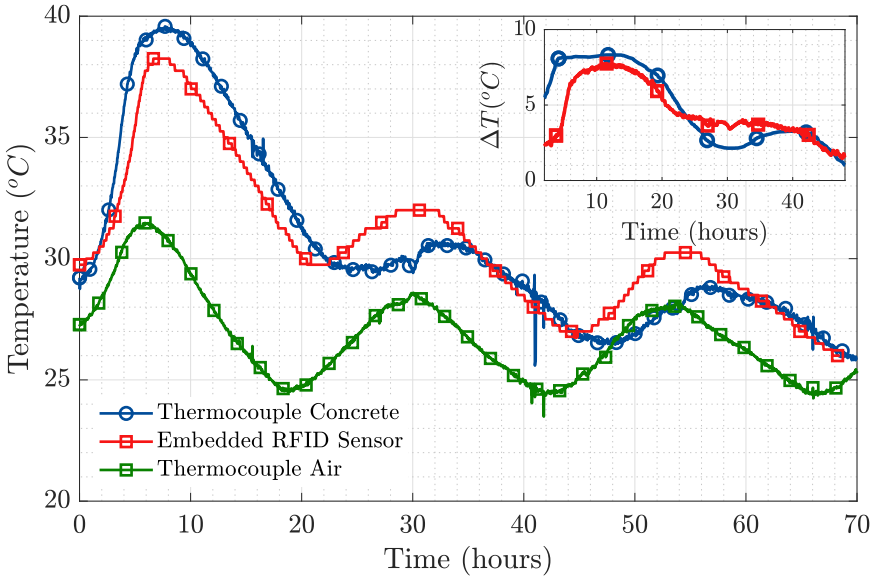

Figure 9. Main Figure: Temperature measured by the RFID sensor compared to temperature from the thermocouples. Top right Figure: Differential temperature inside concrete, removing the effect of room temperature.

Once validated, the feasibility of the proposed RFID system for wireless monitoring of the setting reaction produced in concrete over time at 0.868 GHz, it could be of interest for potential designers to compare the attenuation parameter L_{TMUT} (see Table 3) obtained from the results presented in [1], at 0.43 GHz, 0.868 GHz (this paper), and 2.45 GHz. These are typical frequencies in the ISM band employed in sensing applications. Table 4 displays the total propagation loss in the embedding medium (L_{TMUT}) for the three considered frequencies at several time instants along the setting reaction. From these results, it may be concluded that for the same communication link parameters (transmitted power, sensitivity, and antenna gain), the selected operation frequency is a critical parameter to take into account when designing RFID systems to operate embedded in high permittivity lossy materials. For the presented scenario, and in terms of the propagation loss, RFID solutions operating

at frequencies below 0.868 GHz (e.g., 0.43 GHz) may be achievable, while those having an operation frequency above 0.868 GHz (e.g., 2.45 GHz) may not be considered feasible. When size constrains are taken into consideration, 0.868 GHz seems to be a reasonable choice for these applications.

Table 4. Concrete propagation parameters for d_{MUT} = 0.15 m and 0.02 m at 0.43 GHz, 0.868 GHz, and 2.45 GHz.

L_{TMUT}(dB) @(0.15 m/0.02 m)	f = 0.43 GHz	f = 0.868 GHz	f = 2.45 GHz
Day 0.5	44.24/6.77	56.27/13.42	82.8/24.62
Day 1	39.14/5.93	50.62/12.32	76.67/23.37
Day 2	36.23/5.55	49.02/12.02	78.44/23.3
Day 4	33.25/4.99	45.73/11.33	77.28/23
Day 8	31.79/4.67	43.99/11.02	78.06/23.02

4. Conclusions

The results presented in this manuscript are proof of the possibility of employing wireless technology to remotely monitor the physical and chemical processes produced during the setting reaction of concrete using temperature measurements as a proxy for the evolution of a hydration process that occurs during the setting of concrete. This information can be of use at construction sites to reduce construction time, as well as for safety purposes such as building's structural strength monitoring.

The reading distances obtained during in-field measurements were in line with the propagation attenuation values employed for propagation loss over distance in air estimation. This means that available data to describe this communication scenario accurately represents the real propagation conditions.

The results presented in this paper for the proposed RFID sensor validate its adequacy for remote wireless monitoring of the hydration reaction of concrete during its curing process by means of a stable temperature measurement conducted with a fully-embedded wireless RFID sensor. The wide band capabilities of the presented device make it possible to set up a precise and stable communication link with an external reader from the beginning of the hydration reaction, which validates that the sensor remains well matched despite the change produced in the dielectric properties of a concrete mixture throughout the setting reaction.

This system using active RFID technology can be easily adapted to integrate further sensors to the electronics of the embedded device (e.g., moisture sensor) and conduct a broader characterization of the physical and chemical properties of the concrete sample. By tuning the energy consumption of the RFID device, it is also possible to conduct long term monitoring of the medium. The same wireless system can also be used in other construction materials such as self-leveling mortar for similar purposes.

5. Patents

The patent entitled "SISTEMA DE TRANSMISIÓN ENTRE UN MEDIO DE TRABAJO Y UN MEDIO DE DESTINO CON DIFERENTES PERMITIVIDADES" with application number P202030087 is currently being processed.

Author Contributions: Conceptualization, J.R., G.G.-L., L.J.-R. and I.C.; methodology, J.R., G.G.-L., L.J.-R. and I.C.; validation, G.G.-L., J.R., L.J.-R., I.C., T.I. and I.S.; formal analysis, G.G.-L., J.R. and L.J.-R.; resources, J.R., L.J.-R., I.C. and I.S.; data acquisition, G.G.-L., I.C., T.I. and I.S.; funds acquisition, J.R., L.J.-R., I.C. and I.S.; writing—original draft preparation, G.G.-L. and J.R.; writing—review and editing, J.R., L.J.-R., I.C., T.I. and I.S. All authors have read and agreed to the published version of the manuscript.

Funding: This work was supported by the Spanish "Comision Interministerial de Ciencia y Tecnologia" (CICYT) under projects PID2019-107885GB-C31 / AEI / 10.13039/501100011033, MDM2016-0600, and by the "Unidad de Excelencia María de Maeztu", 2017–2020.

Acknowledgments: We would like to sincerely thank PROMSA, and specially Jorge Altet (R+D Director), Elena Colomina (Innovation Manager) and Iris Márquez (R+D Technician), for their tremendous help and support during the measurement campaign, for letting us borrow their facilities, and for guaranteeing top quality concrete aggregates to conduct the measurements.

Conflicts of Interest: The authors declare no conflict of interest.

References

1. González-López, G.; Blanch, S.; Romeu, J.; Jofre, L. Debye Frequency-Extended Waveguide Permittivity Extraction for High Complex Permittivity Materials: Concrete Setting Process Characterization. *IEEE Trans. Instrum. Meas.* **2019**, *69*, 5604–5613. [CrossRef]
2. Cataldo, A.; De Benedetto, E.; Cannazza, G. Hydration Monitoring and Moisture Control of Cement-Based Samples Through Embedded Wire-Like Sensing Elements. *IEEE Sens. J.* **2015**, *15*, 1208–1215. [CrossRef]
3. Zhou, S.; Sheng, W.; Deng, F.; Wu, X.; Fu, Z. A Novel Passive Wireless Sensing Method for Concrete Chloride Ion Concentration Monitoring. *Sensors* **2017**, *17*, 2817. [CrossRef] [PubMed]
4. Zhou, S.; Deng, F.; Yu, L.; Li, B.; Wu, X.; Yin, B. A Novel Passive Wireless Sensor for Concrete Humidity Monitoring. *Sensors* **2016**, *16*, 1535. [CrossRef] [PubMed]
5. Ozbey, B.; Erturk, V.B.; Demir, H.V.; Altintas, A.; Kurc, O. A Wireless Passive Sensing System for Displacement/Strain Measurement in Reinforced Concrete Members. *Sensors* **2016**, *16*, 496. [CrossRef] [PubMed]
6. Ramos, A.; Girbau, D.; Lazaro, A.; Villarino, R. Wireless concrete mixture composition sensor based on time-coded UWB RFID. *IEEE Microw. Wirel. Compon. Lett.* **2015**, *25*, 681–683. [CrossRef]
7. Jayawardana, D.; Liyanapathirana, R.; Zhu, X. RFID-Based Wireless Multi-Sensory System for Simultaneous Dynamic Acceleration and Strain Measurements of Civil Infrastructure. *IEEE Sens. J.* **2019**, *19*, 12389–12397. [CrossRef]
8. Liu, Y.; Deng, F.; He, Y.; Li, B.; Liang, Z.; Zhou, S. Novel concrete temperature monitoring method based on an embedded passive RFID sensor tag. *Sensors* **2017**, *17*, 1463. [CrossRef] [PubMed]
9. Manzari, S.; Musa, T.; Randazzo, M.; Rinaldi, Z.; Meda, A.; Marrocco, G. A passive temperature radio-sensor for concrete maturation monitoring. In Proceedings of the 2014 IEEE RFID Technology and Applications Conference (RFID-TA), Tampere, Finland, 8–9 September 2014; pp. 121–126.
10. Gartner, E.; Young, J.; Damidot, D.; Jawed, I. Hydration of Portland cement. *Struct. Perform. Cem.* **2002**, *2*, 57–113.
11. Narmluk, M.; Nawa, T. Effect of fly ash on the kinetics of Portland cement hydration at different curing temperatures. *Cem. Concr. Res.* **2011**, *41*, 579–589. [CrossRef]
12. EM Microelectronic, 18000-63 Type C (Gen2) and 18000-63 Type C/18000-64 Type D (Gen2/TOTAL) RFID IC. Available online: https://www.emmicroelectronic.com/product/epc-and-uhf-ics/em4325 (accessed on 16 September 2020)
13. NORDIC ID NUR-10W RFID MODULES. Available online: https://www.nordicid.com/device/modules/ (accessed on 16 September 2020)
14. Balanis, C.A. *Antenna Theory: Analysis and Design*; John Wiley & Sons: Hoboken, NJ, USA, 2016.
15. Cardama, Á.; Jofre, L.; Rius, J.M.; Romeu, J.; Blanch, S.; Ferrando, M. Antenas. *Ed. UPC* **2002**, *8032*.
16. Sellés, V.; Miquel, G.L.G.; Jofre, L. Embedded Sensor Transmission Optimization with a X-Wave mini-Anechoic Chamber. In Proceedings of the 2020 XXXV Simposium Nacional de la Unión Científica Internacional de Radio (URSI Málaga, 2020), Málaga, Spain, 2–4 September 2020.
17. Lin, Y.; Meng, L.; Jin, C.; Shuang, L. Design and Anti-Interference Ability Analysis of RFID Positioning System for Mine Locomotive. In Proceedings of the 2017 IEEE International Conference on Computational Intelligence and Computing Research (ICCIC), Coimbatore, India, 14–16 December 2017; pp. 1–4.
18. Fu, X.; Yao, H.; Postolache, O.; Yang, Y. Message forwarding for WSN-Assisted Opportunistic Network in disaster scenarios. *J. Netw. Comput. Appl.* **2019**, *137*, 11–24. [CrossRef]
19. Fu, X.; Yao, H.; Yang, Y. Cascading failures in wireless sensor networks with load redistribution of links and nodes. *Ad Hoc Netw.* **2019**, *93*, 101900. [CrossRef]

20. Fu, X.; Yao, H.; Yang, Y. Modeling Cascading Failures for Wireless Sensor Networks With Node and Link Capacity. *IEEE Trans. Veh. Technol.* **2019**, *68*, 7828–7840. [CrossRef]

Publication III

5.3 [GG-III] Resonance-Based Microwave Technique for Body Implant Sensing

Publication: González-López, G., Jofre Roca, L., Amorós García de Valdecasas, S., Rodríguez-Leor, O., Gálvez-Montón, C., Bayés-Genís, A., & O'Callaghan, J. (2019). Resonance-Based microwave technique for body implant sensing. Sensors, 19(22), 4828.

sensors

MDPI

Article

Resonance-Based Microwave Technique for Body Implant Sensing

Giselle González-López [1,*,†], Lluis Jofre Roca [1,†], Susana Amorós García de Valdecasas [1], Oriol Rodríguez-Leor [2,3,4], Carolina Gálvez-Montón [2,5], Antoni Bayés-Genís [2,3,4,5] and Joan O'Callaghan [1]

1 School of Telecommunication Engineering, Universitat Politècnica de Catalunya, 08034 Barcelona, Spain; luis.jofre@upc.edu (L.J.R.); susana.amoros@upc.edu (S.A.G.d.V.); joano@tsc.upc.edu (J.O.C.)
2 CIBERCV, Instituto de Salud Carlos III, 28029 Madrid, Spain; oriolrodriguez@gmail.com (O.R.-L.); cgalvez@igtp.cat (C.G.-M.); abayesgenis@gmail.com (A.B.-G.)
3 Heart Institute (iCor), Germans Trias i Pujol University Hospital, 08916 Badalona, Spain
4 Department of Medicine, Universitat Autònoma de Barcelona, 08193 Barcelona, Spain
5 ICREC Research Program (Health Science Research Institute Germans Trias i Pujol), Can Ruti Campus, 08916 Badalona, Spain
* Correspondence: giselle.gonzalez@tsc.upc.edu
† These authors contributed equally to this work.

Received: 14 October 2019; Accepted: 4 November 2019; Published: 6 November 2019

Abstract: There is an increasing need for safe and simple techniques for sensing devices and prostheses implanted inside the human body. Microwave wireless inspection may be an appropriate technique for it. The implanted device may have specific characteristics that allow to distinguish it from its environment. A new sensing technique based on the principle of differential resonance is proposed and its basic parameters are discussed. This technique allows to use the implant as a signal scattering device and to detect changes produced in the implant based on the corresponding change in its scattering signature. The technique is first tested with a canonic human phantom and then applied to a real in vivo clinical experiment to detect coronary stents implanted in swine animals.

Keywords: microwave sensing; biosensing; object localization; implant; differential resonance; stent; non-ionizing; phantom; relative permittivity

1. Introduction

There is an increasing use of body tiny implants and human prostheses known as implanted devices (ID) with varying geometries and compositions [1], but having in common dimensions up to some tens of millimeters that when used in a biological environment with permittivities around the 50 s may have an electromagnetic resonance into the UHF (0.3–3.0 GHz) frequency band.

These IDs may change some characteristics over time in such a way that their functionality may be compromised. These changes may be triggered by wear corrosion, breakdowns, adherence of biological tissues, etc. This would most likely result in operational malfunctioning and, in most cases, a change in its electrical parameters, which will result in a change of its resonant frequency. Examples of these IDs may include metal stents (usually covered by drug-eluding substances) [2], which currently are the preferred solution for the treatment of IHD (Ischemic Heart Disease) [3], pins and screws in orthopedics and craniofacial surgery, and artificial joints [4,5], with typical lengths ranging from 1 to 30 cm. These, when implanted in regions of the human body with permittivities between 4 and 57, produce a resonance in the UHF region.

UHF signals with a convenient dynamic range and appropriate antenna probes [6] are able to penetrate some tens of cm into the body and interact with those devices giving a scattering response

that may be strongly influenced by the electrical resonance of the ID, therefore, allowing to monitor the state of the device. In order to obtain a proper diagnostic, it is necessary to have a clear signature of the scattered signal, as the one produced by a change of the resonant frequency.

Current solutions for pre-clinical identification of some of the previously mentioned conditions are either invasive, ionizing or require complex procedures. This is the case of intravascular ultrasound (IVUS) [7], X-ray angiography (XRA) [8] or intravascular optical coherence tomography (OCT) [9]. High-frequency solutions have been within the scope of many studies, however, in most cases, they are just able to detect superficial implants [10] or require the previous incorporation in the implant of an electronic chip [11].

In this paper, we propose to use implants as signal scattering devices and to detect any physical variation produced in the implant based on the corresponding variation of its scattering signature. The presented technique is able to extract the signature contained in the resonance frequency of the backscattered signal produced by the target device. We show that this frequency depends on the electrical length of the device and may be used to detect, position and monitor changes in devices having electrical dimensions in the range of cm and depths of several centimetres.

In Section 2, we present the analytic formulation of the presented scenario and the technique to extract the resonance. In Section 3, we apply the technique to a body phantom hexagonal geometry, by means of a monostatic or a bistatic scattering measurement. A parametric analysis in terms of the IFFT (Inverse Fast Fourier Transform) of the detection capabilities of the proposed technique is then performed. In Section 4, we apply the technique to a coronary stent implanted in a swine animal. Finally, in Section 5, some conclusive remarks are presented.

2. Resonant Scattering Produced by the Implanted Device (ID)

In this section, the basic diagram and expressions supporting the resonance-based monitoring principle are presented. The ID is modeled, without a loss of generality, as a generic electric dipole-based antenna with a virtual port defined somewhere in its structure from which a resonance frequency may be defined.

The generic scenario, shown in Figure 1, consists of a bistatic geometry with the transmitting (Tx) and receiving (Rx) probe antennas represented by two dielectrically filled ridge horn antennas [6], and the ID is represented as a cylindrical object of length l_{ID}, located at a distance $\vec{r}_{TD}$ and $\vec{r}_{RD}$ from Tx and Rx probes respectively, all of it immersed into a dielectric medium of permittivity $\varepsilon_r(r)$, supposed to be low frequency dispersive in the range of the ID resonance. Let $P_T = |a_T|^2$ and $P_R = |b_R|^2$ be the transmitted and received power into the Tx and Rx respectively, Z_{in}^{ID} the impedance of the ID when fed into a virtual port, and Z_{LD}^{ID} a virtual impedance loading the device's port, that will model the operational state of the ID.

In a complex scenario, as those found in real situations, far-field conditions and homogeneous-space propagation do not meet, and the conventional radar formulation is not applicable. In consequence, an approach based on the reciprocity theorem is needed [12]. The signal b_R measured into the receiving antenna may be expressed as [13]:

$$\begin{aligned} \rho_{TR}^{ID} &= \frac{b_R}{a_R} = \frac{V_{OC}^{TD} V_{OC}^{RD}}{2P_T} \frac{1}{Z_{in}^{ID} + Z_{LD}^{ID}} \\ &= \frac{h_{eff}^2 E_{inc}^{TD} E_{inc}^{RD}}{2P_T} \frac{1}{Z_{in}^{ID} + Z_{LD}^{ID}} \end{aligned} \tag{1}$$

where V_{OC}^{TD} and V_{OC}^{RD} are the open-ended circuit voltages at the port of the ID when illuminated by the Tx or Rx (reciprocity-based) antennas that may respectively be expressed as the product of the incident field E_{inc}^{TD} and E_{inc}^{RD} into the ID produced by the Tx and Rx (reciprocity-based) and the ID effective high (h_{eff}).

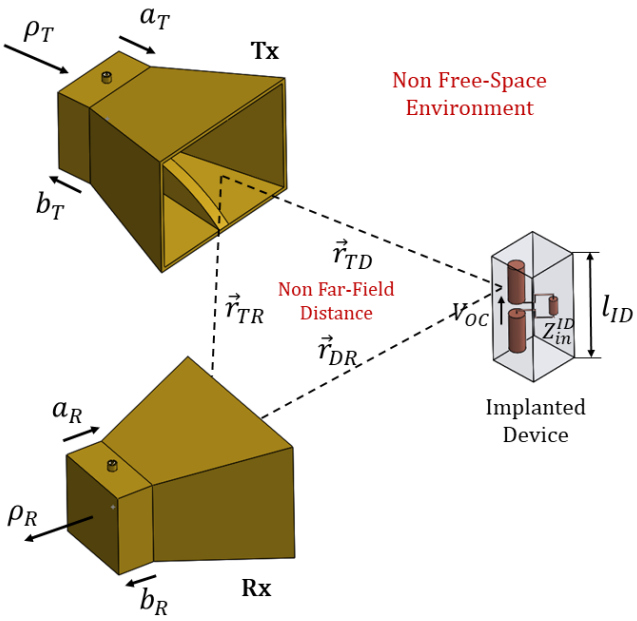

Figure 1. General Scenario.

For the prove of concept of the principle we will consider a cylindrical electric dipole (thin conducting cylinder) of length l_{ID}, with its first resonant frequency (half wave dipole) at f_{res}^{ID}. The input impedance Z_{in}^{ID} may be approached, provided than the Tx/Rx antennas are significantly distant and/or the medium has a certain amount of loss as it would be the case for most of the media of interest, by its self-impedance Z_{11}^{ID}. It is then possible to express the self-impedance of the electric dipole immersed into a medium of permittivity ε_r at a frequency f around its resonance frequency (f_{res}^{ID}), as [14]:

$$Z_{in}^{ID} \cong Z_{11}^{ID} = \left(73 + j43\frac{\frac{f l_{ID}\sqrt{\varepsilon_r}}{c_0} - 0.45}{0.05}\right)\Omega \tag{2}$$

where c_0 is the velocity of light in vacuum, and for which $Z_{in}^{ID} = 73 + j0$ at the resonance frequency, where a minimum into the input impedance is obtained. Substituting (2) into (1) we may then calculate the frequency response of the system, $\rho_{TR}^{ID}(f)$ for which a resonant maximum is obtained at the resonance, f_{res}^{ID}. The representation of this frequency response will give us the necessary information to diagnose the actual state of the resonance and, in consequence, the state of the implant.

As a first analytic approach, a cylindrical implant with a length $l_{ID} = 20$ mm and distances $r_{TD} = r_{RD} = r_{TR} = r_{TRD} = 50$ mm into a uniform medium of permittivity $\varepsilon_r = 50$ with a frequency span from 0.3 to 1.2 GHz is considered. In this example, the Tx and Rx antennas are supposed to be broad-band biconical dipoles (with a radiation resistance $R_a^{TR} = 75\ \Omega$ and a broad flat frequency covering the range of the ID resonance f_{res}^{ID}, while the implant itself resonates at a frequency of 0.85 GHz. In this specific example, because the far-field equations may be used (uniform medium and far-field distances), the expression for $\rho_{TR}^{ID}(f)$ may be analytically written as:

$$\rho_{TR}^{ID} \cong -\frac{25 l_{ID}^2}{R_a^{TR}\varepsilon_r}\left(\frac{e^{-j21f(GHz)\sqrt{\varepsilon_r}r_{TRD}}}{r_{TRD}}\right)^2 \times \frac{1}{1 + j\left(40f(GHz)\sqrt{\varepsilon_r}l_{ID} - 5.3\right)} \tag{3}$$

In a similar way ρ_{TR}^{DR}, the signal traveling directly from the Tx to the Rx that may be calculated with the Friis equation [15] into the homogeneous background medium.

Figure 2 represents the frequency response, between 0.3 and 1.2 GHz where a single resonance may be considered, of the Tx-ID-Rx system through the relation, $\rho_{TR}^{ID}(f)$, for two states: (a) short-circuited ($Z_{LD}^{ID} = 0.0$), where the ID is supposed to work properly as a 20 mm cylindrical continuous element, and (b) open-circuited ($Z_{LD}^{ID} = 1000$), where the ID is supposed to be broken in the middle as two shorter 10 mm elements in which the actual value of 10 mm represents the remaining structural backscattering.

For a real application, as it is seen in the next section, the measured magnitude will be the superposition of two signals: (a) the signal Tx-ID-Rx, with (b) the direct signal Tx-Rx, resulting into a differential pattern ($\rho_{TR}^{ID} - \rho_{TR}^{DR}$) in which resonance will appear as a minimum (Figure 2).

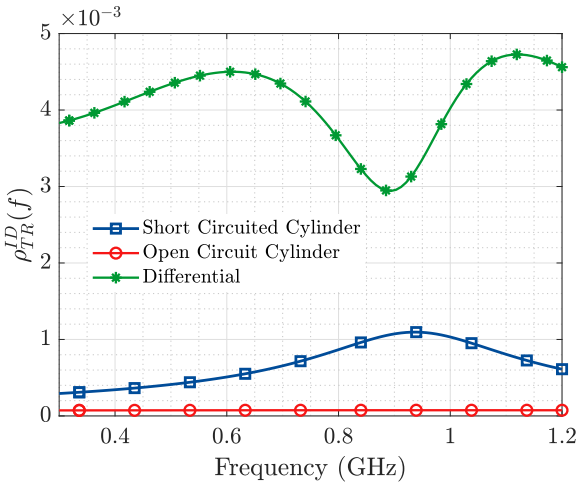

Figure 2. $\rho_{TR}^{ID}(f)$ of a 20 mm conducting cylinder representing the ID. The resonance is distinguished when the ID is fully operational (continuous object or $Z_{LD}^{ID} = 0$), from a non-operational state (breakdown or $Z_{LD}^{ID} = 1000$). The interferent differential signal is also reported.

3. Numerical and Experimental Validation

The technique described in the previous section for difference resonance sensing of IDs in a biological material is tested first through simulations conducted in CST Studio, and then through experimental measurements conducted with two ridged horn antennas [6], integrated in the measurement set up in Figure 3 and filled with a phantom mimicking the permittivity of biological tissue which values have been extracted from [16].

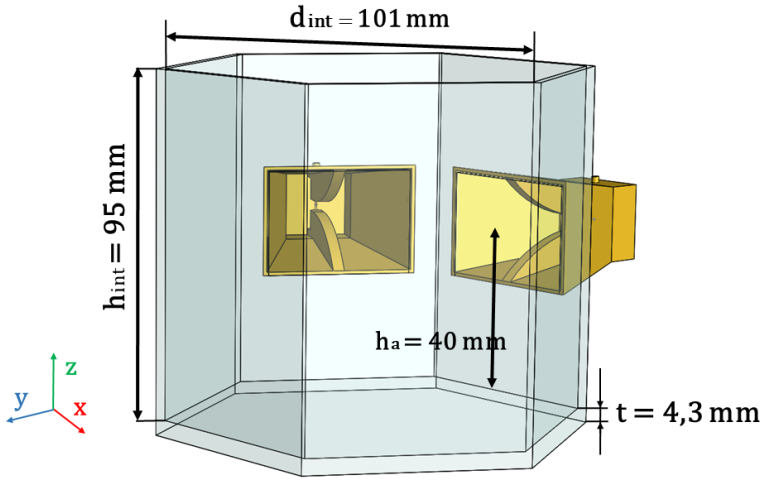

Figure 3. Schematic of the Experimental Measurement Set Up.

This hexagonal set up has been manufactured in PLA (polylactic acid) using 3D printing technology to perfectly host the horns. The hexagonal shape allows to recreate the layout the antennas would have in an in vivo scenario. The dimensions of the hexagonal box are: inner diameter $d_{int} = 101$ mm, inner height $h_{int} = 95$ mm, wall thickness $t = 4.3$ mm and 35 mm height h_a from the bottom of the set up to the antenna.

At simulation stage, the ridged horn antennas in [6] integrated on the hexagonal set up in Figure 3, have been modeled using CST Studio. The phantom material filling the horns and the set up has been defined according to [16] ($\varepsilon'_r = 57$ and $\tan\delta = 0.6$ at 0.8 GHz). It must be considered that the resonance frequency of the ID must fall within the operational bandwidth of the horns (0.5 GHz to 3 GHz [6]). Also, the ID must be aligned parallel to the vertical E-field radiated by the antennas for optimal detection.

In Figures 4 and 5 the simulated joint E-field distribution of both horn antennas, transverse to the aperture plane of the antennas, is represented at 0.8 GHz (estimated resonance frequency of the considered ID) for the case when no implant is present in the scenario (Figure 4), and for an implanted device placed in front of the aperture of one of the antennas (Figure 5), clearly showing the influence of the implant. We can also observe the necessity of placing the probe antennas in such a way that the implant is located inside the crossing region of the field distribution radiated by both (Tx and Rx) antennas, which contributes to ID sensing.

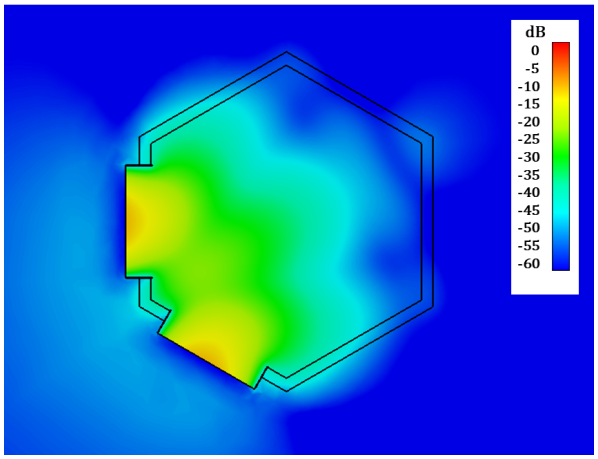

Figure 4. Simulated joint E-field distribution into the transverse plane of the horn antennas at 0.8 GHz. No ID.

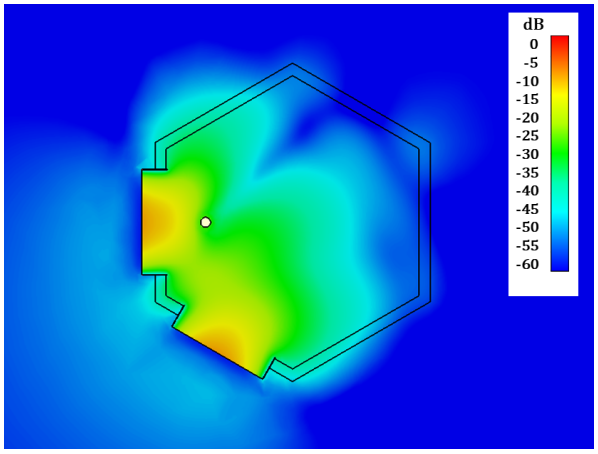

Figure 5. Simulated joint E-field distribution into the transverse plane of the horn antennas at 0.8 GHz. Frontal ID.

The results exhibited in this section correspond to the simulation/experimental measurement of an alumina rod of 24 mm length and 4 mm diameter (parallel to the E-field radiated by the horn antennas) for different positions along the y axis (see Figure 3), as a mean to asses the variation introduced by the resonant object in the scattering matrix ([S]) of the Tx and Rx antennas. Baseline results (no Rod) for the medium without the ID are also included. These measurements exhibit a repeatability error, computed according to the standard deviation of the mean, below 0.04 within the frequency band of interest.

Figures 6 and 7 represent the magnitude of the transmission coefficient (S_{12}) in (dB) simulated and measured respectively, as a function of frequency. Because of the high ohmic loss present in this kind of media (in the order of 2 dB/cm), it is possible to extract better information from the transmission (bistatic measurement) than from the reflection parameters (monostatic measurement). In Figures 8 and 9 the results presented in the frequency domain have been time-converted applying the IFFT.

From the representation of the S_{12} parameter for the baseline scenario (no ID), in both simulated and measured results, a steady slope with a maximum around 0.5 GHz is observed, which is in agreement with the results presented in [6]. When the ID is placed in front of the Tx and Rx, a modification in the S_{12} in the shape of a "resonance" is produced. When the metallic rod is sequentially shifted, the frequency at which this "resonance" is produced and its depth variate too, as illustrated both in the simulation (Figure 6) and the ex-vivo measurement (Figure 7). The occurrence of this resonance indicates the capability to detect the presence of a resonant object implanted in a biological material. While the change of its frequency and depth triggered by a variation of its distance to the Tx and Rx antennas mean that it is also possible to locate the ID.

When these figures for the transmission coefficient are transformed to the time domain (Figures 8 and 9), a more evident representation of the aforementioned phenomenon is observed. For the case where no ID is present in the scenario, it is possible to notice a single maximum in $IFFT(S_{12})$ which corresponds to the direct ray between the Tx and Rx EGRH antennas. However, when the ID is introduced, two maximums are observed. The first one corresponds to the direct ray (from Tx to Rx), while the second one corresponds to a reflected ray generated by the presence of the resonant metallic implant. It is of interest to notice that all direct rays peak at the same time instant, meanwhile, the reflected rays achieve their maximum later (at a time corresponding with its actual position) as they are placed further from the Tx/Rx antennas. The amplitude of the reflected ray decreases as the distance to the Tx/Rx antenna increases, as the amount of losses to cope with increase in the distance.

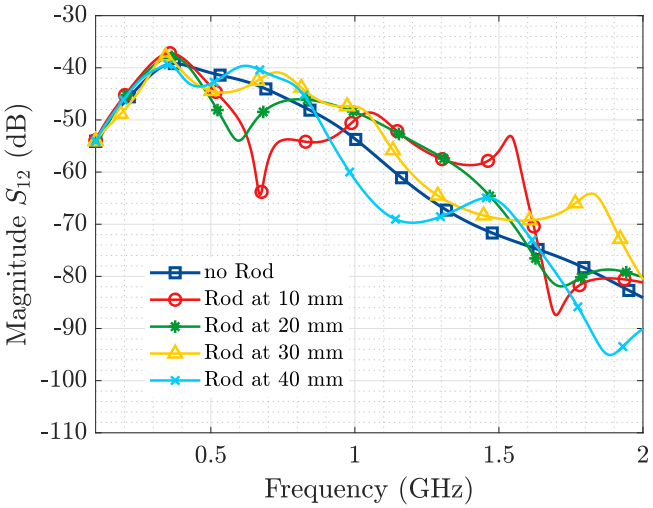

Figure 6. Metallic Rod Detection. Simulation S_{12}.

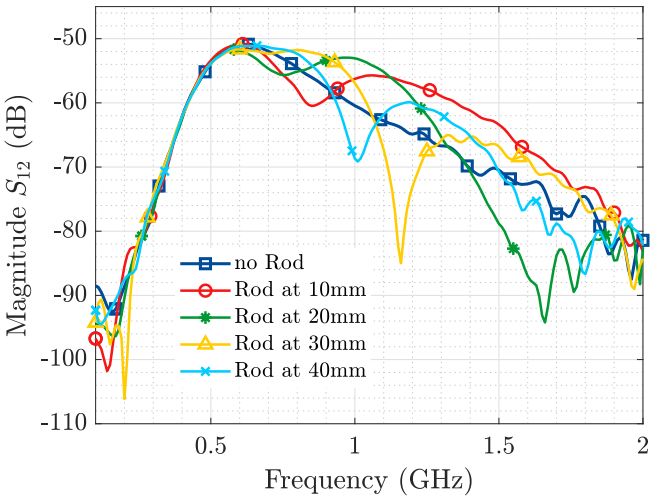

Figure 7. Metallic Rod Detection. Experimental measurement S_{12}.

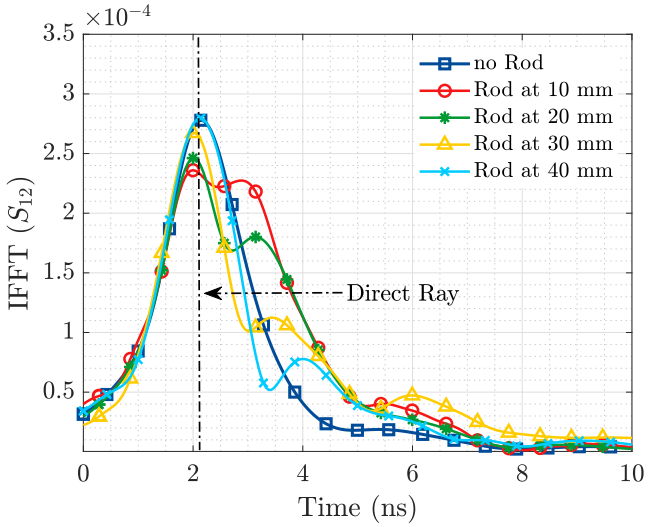

Figure 8. Metallic Rod Detection. Simulation IFFT.

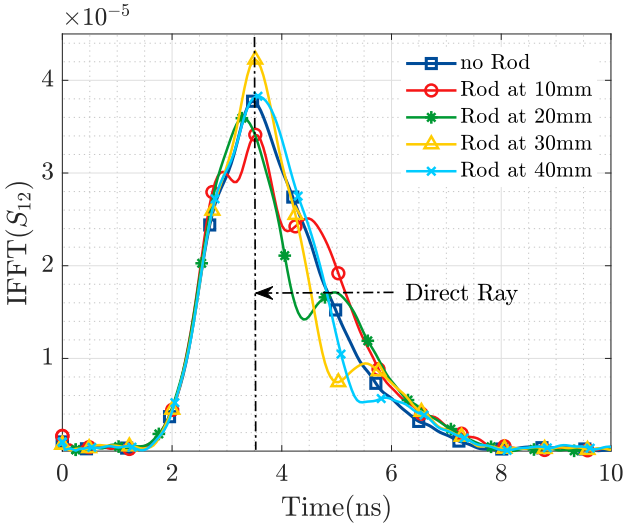

Figure 9. Metallic Rod Detection. Experimental measurement IFFT.

The 1.4 ns time shift between IFFT of the ex vivo experimental measurement and the CST simulation is associated to the time-delay introduced by the 0.3 m teflon coaxial cables employed at measurement stage.

4. In-Field In Vivo Measurement of Implanted Coronary Stent

After validating the applicability of the resonance-based microwave technique for body implant sensing with simulations and experimental measurements, we were able to test its performance in an in vivo scenario. A swine animal implanted with a coronary stent has been measured using the aforementioned procedure. Figure 10 depicts the display of the antennas on the side of the pig's rib cage, aiming to the implanted stent, with a bistatic geometry equivalent to the one in Figure 3.

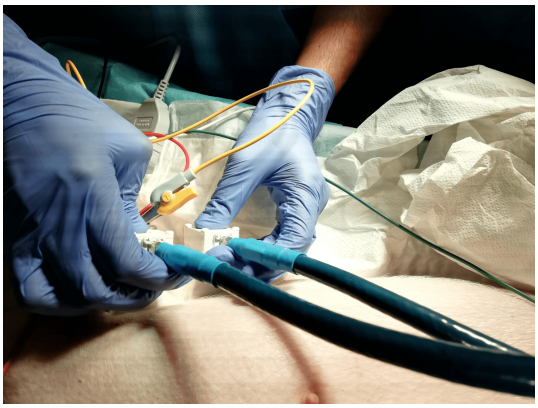

Figure 10. In vivo measurement.

The propagation conditions present during the in vivo measurement, although similar, slightly variate with respect to the ex-vivo scenario. Before arriving to the implant, the signal transmitted by the Tx horn antenna must go through a layer of skin, fat and muscle, and then through the bone of the rib cage. This propagation conditions along with the lack of knowledge on the precise location and orientation of the stent, required a limited surface and angular scan. The flexibility and sensitivity of the technique allowed a proper disposition of the Tx/Rx probes which at the end permitted to obtain robust results.

From Figure 11, it is observed that we are able to detect the presence of the ID from the information in the magnitude of the transmission coefficient, while Figure 12 displays in the time domain the reflection produced by the presence of the stent. Based on the results of Figures 11 and 12, and the geometry of the applied probes in Figure 10, an approximate depth of 3 cm with respect to the plane of the horn antennas may be estimated.

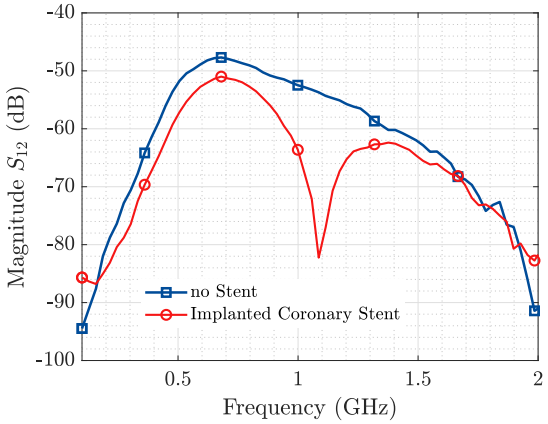

Figure 11. Coronary Stent Sensing. S_{12}.

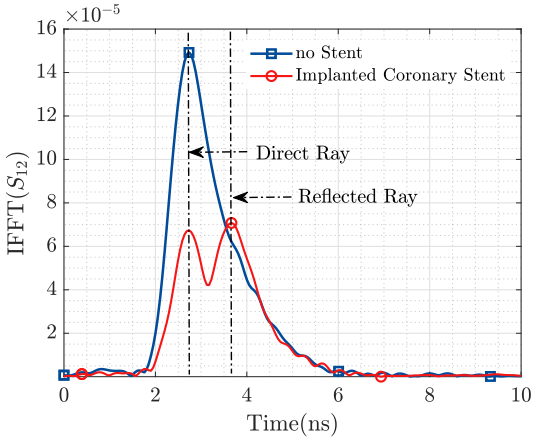

Figure 12. Coronary Stent Sensing. IFFT.

5. Conclusions

A novel technique for sensing of body implants has been analytically presented and validated through simulations, experimental measurements of a phantom mimicking the dielectric properties of biological tissue and, finally, by conducting an in vivo measurement on a coronary stent implanted in a swine animal model.

It is possible to extract information regarding the presence and location of medical implants from the resonant scattering produced by the device itself, with no need to make any modification in the implant.

From the results obtained during the experimental measurements, it is possible to say that the resonance-based microwave technique with the EGRH antennas has detected IDs up to 4 cm deep measured with a general purpose laboratory instrument. This range could be extended to 10 cm (we should not find IDs placed much deeper in real human body exploration) with an enhanced SNR (Signal to Noise Ratio) produced with the adequate featured instrumentation.

Author Contributions: Conceptualization, L.J.R., G.G.-L. and J.O.C.; methodology, L.J.R., G.G.-L. and S.A.G.d.V.; validation, L.J.R., G.G.-L. and S.A.G.d.V.; formal analysis, L.J.R. and G.G.-L.; resources, L.J.R., O.R.-L., C.G.-M., A.B.-G. and J.O.C.; data acquisition, G.G.-L., S.A.G.d.V., O.R.-L. and C.G.-M.; funds acquisition, L.J.R. and J.O.C.; writing—original draft preparation, L.J.R. and G.G.-L.; writing—review and editing, L.J.R. and J.O.C.

Funding: This work was supported by the Spanish "Comision Interministerial de Ciencia y Tecnologia" (CICYT) under projects TEC2016-78028-C3-1-P, MDM2016-0600, and by the "Unidad de Excelencia María de Maeztu", 2017–2020.

Conflicts of Interest: The authors declare no conflict of interest.

References

1. Group, I. *Implantable Medical Devices Market: Global Industry Trends, Share, Size, Growth, Opportunity and Forecast 2019–2024*; IMARC Services Private Limited: Noida, Uttar Pradesh, India, 2019; p. 104.
2. Garg, S.; Serruys, P.W. Coronary stents: Current status. *J. Am. Coll. Cardiol.* **2010**, *56*, S1–S42. [CrossRef] [PubMed]
3. Wong, N.D. Epidemiological studies of CHD and the evolution of preventive cardiology. *Nat. Rev. Cardiol.* **2014**, *11*, 276–289. [CrossRef] [PubMed]
4. Hermawan, H.; Ramdan, D.; Djuansjah, J.R. Metals for biomedical applications. In *Biomedical Engineering—From Theory to Applications*; IntechOpen Limited: London, UK, 2011; pp. 411–430.
5. Guglielmotti, M.; Olmedo, D.G.; Cabrini, R.L. Research on implants and osseointegration. *Periodontol. 2000* **2019**, *79*, 178–189. [CrossRef] [PubMed]
6. Rashid, S.; Jofre, L.; Garrido, A.; Gonzalez, G.; Ding, Y.; Aguasca, A.; O'Callaghan, J.; Romeu, J. 3-D Printed UWB Microwave Bodyscope for Biomedical Measurements. *IEEE Antennas Wirel. Propag. Lett.* **2019**, *18*, 626–630. [CrossRef]

7. Bangalore, S.; Bhatt, D.L. Coronary intravascular ultrasound. *Circulation* **2013**, *127*, e868–e874. [CrossRef] [PubMed]
8. Anderson, R.D.; Pepine, C.J. Coronary angiography: Is it time to reassess? *Circulation* **2013**, *127*, 1760–1762. [CrossRef] [PubMed]
9. McCabe, J.M.; Croce, K.J. Optical coherence tomography. *Circulation* **2012**, *126*, 2140–2143. [CrossRef] [PubMed]
10. Arauz-Garofalo, G.; López-Domínguez, V.; Hernàndez, J.M.; Rodríguez-Leor, O.; Bayés-Genís, A.; O'Callaghan, J.M.; García-Santiago, A.; Tejada, J. Microwave spectrometry for the evaluation of the structural integrity of metallic stents. *Med. Phys.* **2014**, *41*, 041902. [CrossRef] [PubMed]
11. Occhiuzzi, C.; Contri, G.; Marrocco, G. Design of implanted RFID tags for passive sensing of human body: The STENTag. *IEEE Trans. Antennas Propag.* **2012**, *60*, 3146–3154. [CrossRef]
12. Bolomey, J.C.; Capdevila, S.; Jofre, L.; Romeu, J. Electromagnetic modeling of RFID-modulated scattering mechanism. Application to tag performance evaluation. *Proc. IEEE* **2010**, *98*, 1555–1569. [CrossRef]
13. Capdevila, S.; Jofre, L.; Romeu, J.; Bolomey, J.C. Multi-loaded modulated scatterer technique for sensing applications. *IEEE Trans. Instrum. Meas.* **2013**, *62*, 794–805. [CrossRef]
14. Cardama, Á.; Jofre, L.; Rius, J.M.; Romeu, J.; Blanch, S.; Ferrando, M. *Antenas*; Edicions de la Universitat Politècnica de Catalunya: Barcelona, Spain, 2002.
15. Balanis, C.A. *Antenna Theory: Analysis and Design*; John Wiley & Sons: Hoboken, NJ, USA, 2016.
16. Mohammed, B.; Abbosh, A.; Henin, B.; Sharpe, P. Head phantom for testing microwave systems for head imaging. In Proceedings of the 2012 Cairo International Biomedical Engineering Conference (CIBEC), Giza, Egypt, 20–22 December 2012; pp. 191–193.

Publication IV

5.4 [GG-IV] Variable Capacitive Antenna Loading for Embedded RFID Sensors

Publication: González, G., Jofre, L., Romeu, J., & Cairó, I. (2019, March). Variable capacitive antenna loading for embedded RFID sensors. In 2019 13th European Conference on Antennas and Propagation (EuCAP) (pp. 1-5). IEEE.

ATTENTION¡¡
Pages 79 to 83 of the thesis, containing the article mentioned above are available at the editor's web
https://ieeexplore.ieee.org/document/8739840

Publication V

5.5 [GG-V] Antenna Packaging for In-Body Applications

Publication: Romeu, J., González-López, G., Blanch, S., & Jofre, L. (2020, March). Antenna packaging for in-body applications. In 2020 14th European Conference on Antennas and Propagation (EuCAP) (pp. 1-5). IEEE.

ATTENTION¡¡
Pages 85 to 89 of the thesis, containing the article mentioned above are available at the editor's web
https://ieeexplore.ieee.org/document/9135889

Publication VI

5.6 [GG-VI] Optimal Probe Geometry for Microwave Monitoring during in-Lab ex-vivo Measurements

Publication: González-López, G., de Valdecasas, S. A. G., & Jofre, L. (2020, March). Optimal Probe Geometry for Microwave Monitoring during in-Lab ex-vivo Measure- ments. In 2020 14th European Conference on Antennas and Propagation (EuCAP) (pp. 1-4). IEEE.

ATTENTION¡¡
Pages 91 to 94 of the thesis, containing the article mentioned above are available at the editor's web
https://ieeexplore.ieee.org/document/9135888

Publication VII

5.7 [GG-VII] Embedded Sensor Transmission Optimization with a X-Wave mini-Anechoic Chamber

Publication: Sellés Valls, M., González-López, G. & Jofre, L. (2020). Embedded Sensor Transmission Optimization with a X-Wave mini-Anechoic Chamber. XXXV Simposium Nacional de la Unión Científica Internacional de Radio, Málaga, Spain.

Embedded Sensor Transmission Optimization with a X-Wave mini-Anechoic Chamber

Miquel Sellés Valls[(1)], Giselle González-López[(1)], Lluis Jofre[(1)]
miquelselles.valls@gmail.com, giselle.gonzalez@upc.edu, luis.jofre@upc.edu
[(1)] Group ComSensLab, Department of Signal Theory and Communications, Technical University of Catalonia (UPC), Barcelona, Spain.

***Abstract*—The electromagnetic and mechanical design of a measurement set up intended to operate as a X-Wave (microwave, millimeter-wave and terahertz) miniaturized anechoic chamber for small antenna system and embedded device measurement is presented. The transmission coefficient equation between a Reference Antenna (RA) and an Antenna Under Test (AUT) is optimized for the considered scenario. Target applications include but are not limited to measurement of embedded RFID sensors for operation in different ISM bands and mmWave antenna measurement.**

The design and validation of two RAs, with resonance frequencies 0.892 GHz and 50 GHz is presented, along with a proposed AUT. Numerical validation of the proposed set up is provided by means of analytic and EM simulations at 0.892 GHz and 50 GHz.

I. Introduction

Current solutions to measure the electromagnetic properties of antennas are both large in size and costly. Classical anechoic chambers are quite suitable to measure big antenna prototypes (operating from the UHF to X band). Nevertheless, they are not the more adequate choice to measure some of the today's most trendy antenna systems, which are either small in size or high in frequency [1].

Additionally to this, there is an uprising interest in the design of antenna systems able to operate embedded in different kind of media. This is for example the case of RFID sensors to measure the properties of cement-based materials [2], implanted devices (IDs) inside the human body [3]–[5], or sensors to monitor the dielectric properties of fermenting alcohols [6], among other applications. When we arrive at the measurement stage of these sort of devices, we find that current measurement set ups are not the most suitable option as they are intended to measure devices that operate in air. It is not feasible to fill an anechoic chamber with concrete for example, nor to temporarily place a concrete block with an embedded DUT (Device Under Test) inside. However, these kind of materials have in common one property that makes more feasible the measurement process of embedded antennas in a miniaturized set up: they have high valued relative permittivities (ε_r), so the distance at which the Far-Field distance condition is met is reduced by the square root of the relative permittivity of the medium.

As mentioned before, the next generation of mobile communications (5G) is particularly characterized by the migration towards higher frequencies in the so-called millimeter band. This means that mm-band antennas have sizes in the order of a few millimeters or a few centimeters, which implies that Far-Field conditions are met at short distances from the AUT [7]. Hence, reducing the dimensions of the measurement chamber becomes a viable option also for this scenario.

Current trends in the design of anechoic chambers move towards the miniaturization of the set ups, and appeal to OTA (Over The Air) test methods for the measurement of mmWave user equipment, using either direct far-field, indirect far-field or near-field to far-field transformation measurement techniques [8]. The design proposed in this paper, takes advantage of the inherent electromagnetic propagation features of high permittivity media and mmWave propagation, to customize the design Concepcion of classical space-hungry anechoic chambers to today's state of the art applications, while removing the barrier of their prohibitive prices.

The mini-anechoic chamber proposed in this paper uses a planar and circular exploring geometry to conduct near field measurements of a two port network constituted by the RA and the AUT, for the full characterization of the scattering matrix of the network and the projection onto the far-field of the electromagnetic field radiated by the AUT.

As it is implied in [2], when the classical model for spherical wave propagation [7] is applied in a transmission scenario where one of the antennas is located in an embedding medium, it does not provide an accurate representation of the behaviour of the propagation path between antennas. In this paper, a more suitable expression for this scenario is provided.

Details on the design of both the RA and the AUT, as well as the design procedure of the proposed mini-anechoic chamber, are included in Section II. In Section III, analytic and experimental results obtained through simulations are provided to evaluate the X-Wave measurement capabilities of the set up. Some conclusions regarding the results and insights on the upcoming work are included in Section IV.

II. Design of the mini-anechoic chamber

In this section, a description of the design of both the RAs and the AUT is included. The design and functionalities of the proposed mini-anechoic chamber are described, as well as the propagation model used to evaluate the scenario.

A. Reference Antenna Design

The design of the RAs has been conceived to offer a robust performance in the frequency bandwidth of the targeted application. In the current scenario, the ISM band at 0.868 GHz and 0.915 GHz typically used for RFID applications and the mmWave band at 50 GHz , have been selected to test the presented set up.

Two rectangular patch antennas (see Figure II.1), with central frequencies $f_c = 0.892$ and 50 GHz (4x1 lineal

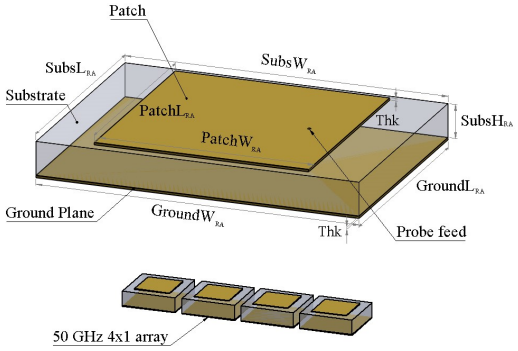

Fig. II.1: RA isometric view. Dimensions expressed in millimeters are: $SubsH_{RA}$ = 15, $SubsW_{RA}$ = $GroundW_{RA}$ = 144, $SubsL_{RA}$ = $GroundL_{RA}$ = 105, $PatchW_{RA}$ = $PatchL_{RA}$ = 95.6, $CoaxPosX_{RA}$ = 30, $CoaxPosY_{RA}$ = 0

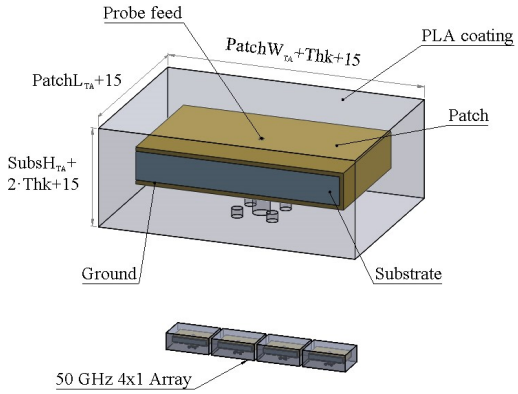

Fig. II.2: AUT with coating. Dimensions expressed in millimeters are: $SubsH_{TA}$ = 7, $SubsW_{TA}$ = $GroundW_{TA}$ = $PatchW_{TA}$ = 50, $SubsL_{TA}$ = $GroundL_{TA}$ = $PatchL_{TA}$ = 31, $CoaxPosX_{TA}$= 0, $CoaxPosY_{TA}$ = 0, $CoatW_{TA}$ = $CoatL_{TA}$ = $CoatH_{TA}$ = 7 .5.

array) respectively, fed with a coaxial probe from underneath, have been designed using PMMA (Poly-methyl methacrylate, $\varepsilon_r = 2.6 - j0.0026$ at 1 GHz) as substrate, and with a (91%) and a 1mm thickness brass patch and ground plane [9].

B. Design of the Antenna Under Test (AUT)

As AUT (in Figure II.2), a patch antenna for embedded operation covering the frequency band from 0.868 GHz to 0.915 GHz has been designed. This antenna has been coaxial fed through the ground plane, as in the case of the RA, but unlike the previous one, the AUT has been designed to present a bidirectional behaviour to be in line with the performance expected from sensing devices. As in the previous case, the patch and the ground plane are made with brass, while the substrate is manufactured in PLA ($\varepsilon_r = 2.5$ and $\tan\delta = 0.004$ at 1 GHz) using 3D printing technology. The bidirectional capabilities of the AUT are met by introducing a short circuit between the ground plane and the patch. An equivalent procedure shall be followed for the design of the twin 50 GHz AUT.

The embedding medium chosen for the validation of the proposed AUT is ethanol, with relative permittivity $\varepsilon_r = 16.3 - j9.85$ at 1 GHz. The inherent effect generated by the losses of the medium on the radiation efficiency (η_{rad}) of the antenna is mitigated by covering the AUT with a PLA coating of 7.5 mm thickness as it is depicted in Figure II.2 [5].

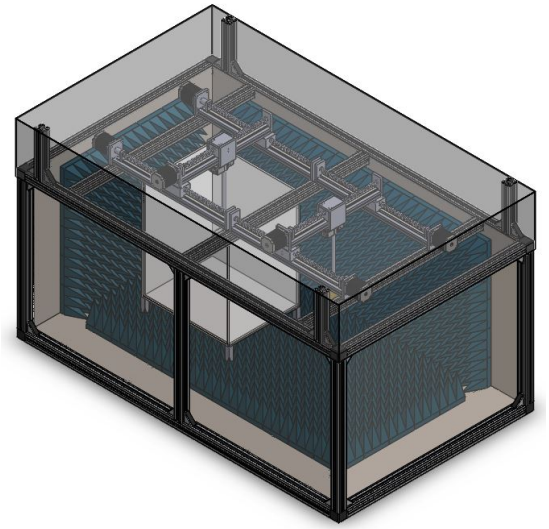

Fig. II.3: Mini-Anechoic Chamber for Sensor Measurement.

C. Design of the Set Up

Four main objectives have been considered at the design of the proposed miniaturized anechoic chamber: (1) to isolate the set up from external interference signals, (2) to absorb the reflections generated by the EM signals inside the set up, (3) to enable a motorized 2-axis independent movement between the RA and the AUT, along with a 360° rotation for each device, and (4) to permit recreating the embedding scenario where the AUT is intended to operate. Additionally, the proposed design offers good measurement accuracy and robustness while remaining a cost-effective solution.

The mini-anechoic chamber in Figure II.3, of dimensions 1530x930x700 mm, is an aluminium profile-based cuboid with 1 mm thick aluminium sheets placed in the inner faces of the profiles serving as the walls of the cuboid. The selection of a metallic material for the walls of the set up intends to mimic a Faraday cage and to endow the chamber with a strong protection from undesired waves coming from the outside.

The inner walls of the set up are covered with 12 cm height pyramid shaped absorbing material in order to inhibit the reflections generated at the walls. A 20 dB wall absorption is assured, and 10 dB absorption in the corners.

The most distinctive feature of the proposed miniaturized anechoic chamber is that, unlike classical chambers, it provides an undemanding and comfortable way to recreate the embedding scenario in which the AUT is intended to operate. For the embedding scenario selected to assess the viability of the set up, a 416x336x467 mm and 8 mm thick PMMA container has been designed to be filled with the ethanol solution. These dimensions are compliant with ethanol's far field distance ($d_{ff} = 42.7mm$ at 0.868 GHz). This container is held and fixed on top of the absorbing pyramids with a 3D printed pillar structure as depicted in Figure II.3. The selection of PMMA has been made considering its electromagnetic and mechanical properties, as it is a low permittivity low loss material that provides toughness, durability and lightness, which all-together contribute to signal post-processing simplification.

An overall view of the embedding scenario can be observed in Figures II.3.

Another main feature of the proposed design is that it permits a 2-axis linear movement with high precision for both the RA and the AUT, as well as a full 360° rotation, which combined allows to fully characterize the field radiated by the device under test. The linear movement is provided by two motorized linear guides placed along the longitudinal direction and another linear guide placed on top of the longitudinal guides, forming a dual axis linear translation stage (Figure II.3).

The 360° rotation movement of the RA and the AUT is guaranteed by a high precision motorized rotation stage attached to the 2-axis translation stage. The manufactured parts in charge of transmitting the circular movement from the rotation stage to the RA and the AUT respectively, permit to integrate a RF rotary joint (with a 2.4mm connector operating up to 50 GHz) in the rotation stage to isolate the rotation movement of the coaxial cables between the antennas and the rotation stage, from the cables going from the rotation stage to the VNA, and to ensure that both the RA and the AUT are placed at the center of the vertical axis of the set up. All stages are connected among them and to the RA and AUT with customized 3D printed pieces.

D. Spherical Wave Propagation Model

The transmission equation based on the classical model for spherical wave propagation in [10], was conceived to describe the propagation path between two radiating elements placed in air. This equation, can be easily readjusted to describe the propagation path these two elements would have if they were placed in a medium with a different permittivity. It is done by replacing the phase constant (β) for the propagation constant ($\gamma = \alpha + j\beta$), where α is the attenuation constant of the medium, and λ_0 by the effective wavelength of the medium ($\lambda_e = \lambda_0/\sqrt{\varepsilon_r}$).

Nevertheless, when only one of the antennas is placed inside the embedding medium, this equation does not provide an accurate representation of the behaviour of the propagation path between antennas. In this case, the Huygens principle allows to tackle this problem as the problem of the propagation of two sources, one (real) with origin at one of the antennas, and the other one (equivalent aperture) with origin at the interface with the medium. In this way, it is possible to make an analytical representation that describes more accurately the current propagation scenario.

$$S_{12A1} = Ae^{-\alpha_{MUT} d_{AUT}} e^{-jk_0(d_{AUT}+d_{RA})} \times \left(\frac{\lambda_0}{4\pi(d_{RA}+d_{AUT})}\right) \quad (1)$$

$$S_{12A2} = Ae^{-\alpha_{MUT} d_{AUT}} e^{-jk_0 d_{RA}} e^{-jk_{MUT} d_{AUT}} \times \left(\frac{\lambda_0}{4\pi d_0}\right)\left(\frac{\lambda_{MUT}}{4\pi d_{AUT}}\right) \quad (2)$$

$$A = \sqrt{G_{RA} G_{AUT} \rho^2_{air-MUT} \frac{Re(Z_{RA})}{Re(Z_{AUT})}} \quad (3)$$

Equation (1) applies the conception of the classical model for spherical wave propagation to the transmission coefficient of the current scenario (Approximation 1), while equation (2) represents the proposed propagation analytic model (Approximation 2). As it is demonstrated in the next section, the higher it is the complex permittivity of the medium, the closer it is the behaviour of the S_{12} parameter to Approximation 2, and the further it is from Approximation 1. λ_0 and λ_{MUT} are the wavelength in air and in the Medium Under Test (MUT), respectively. d_{RA} is the distance from the RA to the interface with the medium, while d_{AUT} is the equivalent parameter with respect to the AUT. α_{MUT} is the attenuation constant of the medium, k_0 is the phase constant in air and k_{MUT} the phase constant in the medium. G_{RA} and G_{AUT} are the gains of the RA and the AUT respectively, $\rho_{air-mut}$ is the transmission coefficient at the interface between the medium and air, and $Re(Z_{RA})$ and $Re(Z_{AUT})$ are the real part of the

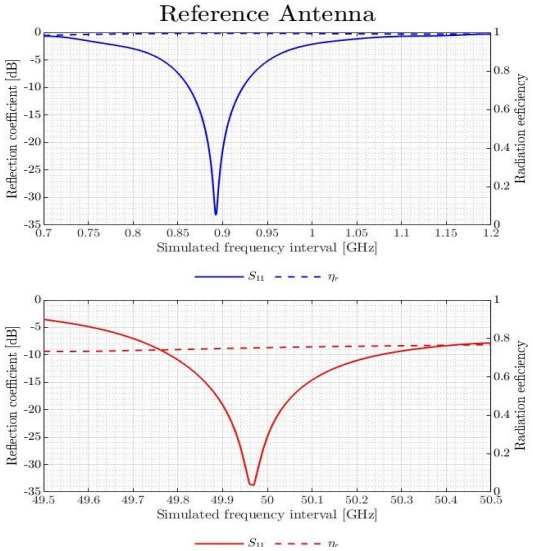

Fig. II.4: S_{11}(dB) and η_{rad} of the RA for 0.892 GHz (blue, top) and for 50 GHz (red, bottom)

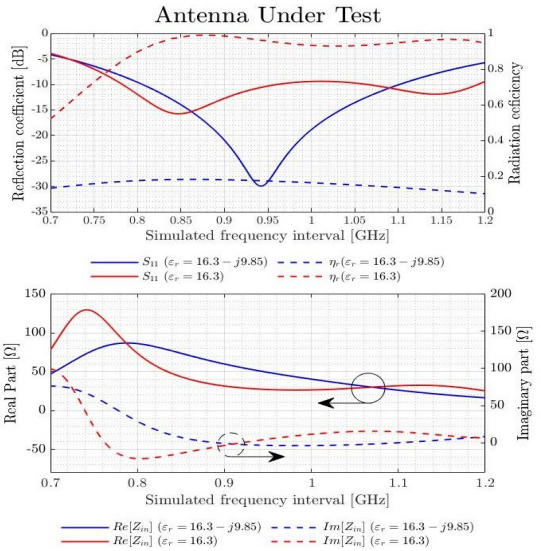

Fig. II.5: AUT's S_{11}(dB) and η_{rad} (top), and Z_{11} (bottom) at 0.892 GHz in ethanol and a lossless medium of $\varepsilon_r = 16.3$.

RA and the AUT's input impedance.

III. Analytic and Experimental Results

In this section, analytic and simulated results of both antennas working in the proposed scenario are presented.

Figure II.4 illustrates the reflection coefficient and the radiation efficiency obtained through CST simulations for both 0.892 GHz and 50 GHz RAs.

The reflection coefficient of the AUT, has been represented for the actual embedding scenario (ethanol) and for a lossless medium with real part relative permittivity equal to ethanol's (Figure II.5 (top)). When working in lossy media the S_{11} may not be a very good indicator of how well the device is radiating, as part of this energy may be actually "absorbed" by the medium itself. In this case, it is recommended to observe the input impedance of the antenna instead (Figure II.5 bottom).

Although it may seem from the reflection coefficient in Figure II.5 that the AUT exhibits a good impedance match in ethanol within the frequency interval of interest, its radiation efficiency when inside the ethanol solution is reduced in a 0.2 factor with respect to the antenna's radiation efficiency when the medium is loss free. This actually means that a significant part of the antenna's input resistance is not getting radiated, but absorbed by the lossy medium, as a consequence of the inherent losses of the medium. This is exactly the kind of phenomenon we expect to be able to measure using the miniaturized anechoic chamber presented in this manuscript. The PLA coating covering the AUT mitigates the undesired effect of the medium losses on the antenna's radiation efficiency, by isolating the antenna from the embedding medium.

In Figures III.1 and III.2, the S_{12} between the RA and the AUT has been represented over distance at 0.892 GHz and 50 GHz, respectively. Three different embedding scenarios have been considered: (1) low permittivity lossless embedding medium ($\varepsilon_r = 2$), (2) ethanol and (3) distilled water ($\varepsilon_r = 80.89 - j5.64$). The experimental value of the S_{12} parameter obtained through CST simulations for two matched antennas, is compared to the analytic approximation given by equations (1) and (2). For low permittivity embedding scenarios, the analytic approximation of the spherical wave

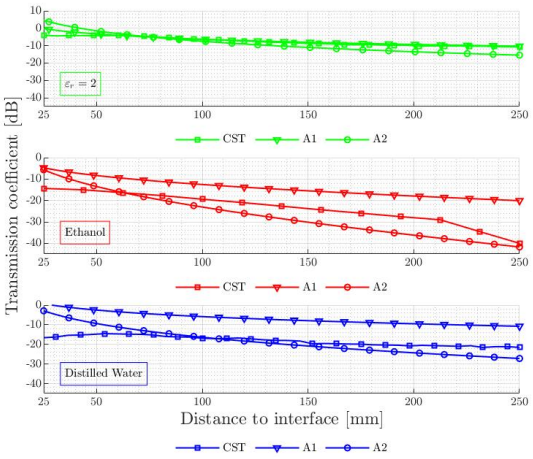

Fig. III.1: Analytic and simulated Transmission coefficient between the RA and the AUT over distance at 0.892 GHz.

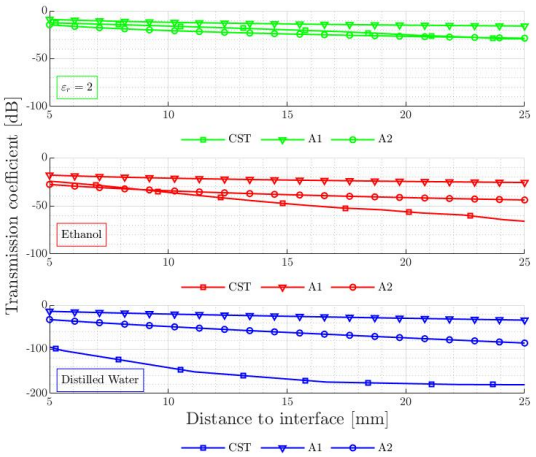

Fig. III.2: Analytic and simulated Transmission coefficient between the RA and the AUT over distance at 50 GHz.

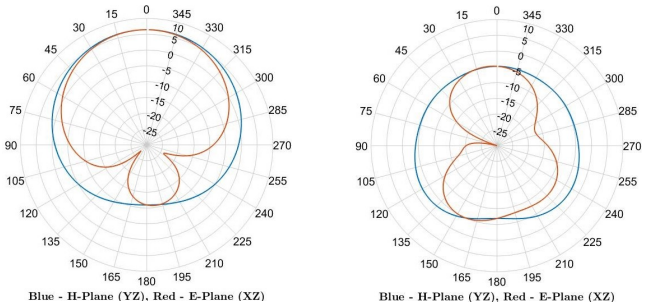

Fig. III.3: Radiation Pattern of the RA and the AUT.

propagation equation in (1) provides a better fit to represent the propagation path covered between RA and AUT, while for high permittivity embedding scenarios equation (2) offers a more accurate representation at 0.892 GHz. Operation at mmWave in high complex permittivity media demands measurement dynamic ranges mostly above the 130dB of today's VNAs, hence becoming a critical issue at measurement stage. The radiation pattern is included in Figure III.3.

IV. Conclusions

A multi-functional miniaturized anechoic chamber has been presented as a suitable method to characterize the behaviour of small antenna systems embedded in materials different than air for measurements covering the X-Wave bands. This open the possibility of employing this kind of measurement set up for applications where the device under test is required to be measured inside a certain medium. This set up is characterized by its versatility, reduced size, mobility, and reduced cost.

An analytic approximation for spherical wave propagation in scenarios involving one of the end devices being embedded in a high permittivity lossy material has been presented and validated through EM simulations.

Future work comprehends the actual fabrication of the proposed set up and its validation through a measurement campaign.

V. Acknowledgements

This work supported by projects CICYT PID2019-107885GB-C31 and MDM2016-0600, and Catalan Research Group 2017 SGR 219. It has been partially supported by FPI scholarship with reference BES-2017-081441.

REFERENCES

[1] Y. M. Antar, "Overview of some future trends in antenna research," in *2017 34th National Radio Science Conference (NRSC)*. IEEE, 2017, pp. 1–1.

[2] G. González-López, S. Blanch, J. Romeu, and L. Jofre, "Debye frequency-extended waveguide permittivity extraction for high complex permittivity materials. concrete setting process characterization," *IEEE Transactions on Instrumentation and Measurement*, 2019.

[3] G. González-López, L. Jofre Roca, S. Amorós García de Valdecasas, O. Rodríguez-Leor, C. Gálvez-Montón, A. Bayés-Genís, and J. O'Callaghan, "Resonance-based microwave technique for body implant sensing," *Sensors*, vol. 19, no. 22, p. 4828, 2019.

[4] S. Rashid, L. Jofre, A. Garrido, G. Gonzalez, Y. Ding, A. Aguasca, J. O'Callaghan, and J. Romeu, "3-d printed uwb microwave bodyscope for biomedical measurements," *IEEE Antennas and Wireless Propagation Letters*, vol. 18, no. 4, pp. 626–630, 2019.

[5] A. K. Skrivervik, M. Bosiljevac, and Z. Sipus, "Fundamental limits for implanted antennas: Maximum power density reaching free space," *IEEE Transactions on Antennas and Propagation*, vol. 67, no. 8, pp. 4978–4988, 2019.

[6] G. González, L. Jofre, J. Romeu, and I. Cairó, "Variable capacitive antenna loading for embedded rfid sensors," in *2019 13th European Conference on Antennas and Propagation (EuCAP)*. IEEE, 2019, pp. 1–5.

[7] Á. Cardama, L. Jofre, J. M. Rius, J. Romeu, S. Blanch, and M. Ferrando, "Antenas," *Edicions UPC*, vol. 8032, 2002.

[8] MVG. Starwave, shaping the future of 5g mmwave ota testing. [Online]. Available: https://www.mvg-world.com/es/news

[9] J. BRANDRUP, E. H. IMMERGUT, and E. A. GRULK, *Polymer Handbook*. John Wiley & Sons, Inc., 1999.

[10] C. A. Balanis, *Antenna theory: analysis and design*. John Wiley & Sons, Inc., 2016.

Publication VIII

5.8 [GG-VIII] 3-D Printed UWB Microwave Bodyscope for Biomedical Measurements

Publication: Rashid, S., Jofre, L., Garrido, A., Gonzalez, G., Ding, Y., Aguasca, A., & Romeu, J. (2019). 3-D printed UWB microwave bodyscope for biomedical mea- surements. IEEE Antennas and Wireless Propagation Letters, 18(4), 626-630.

Publication IX

5.9 [GG-IX] 3D-Printed UHF-RFID Tag for Embedded Applications

Publication: Vidal, N., Lopez-Villegas, J. M., Romeu, J., Barenys, A. S., Garcia-Miquel, A., González-López, G., & Jofre, L. (2020). 3D-Printed UHF-RFID Tag for Embedded Applications. IEEE access, 8, 146640-146647.

IEEE Access
Multidisciplinary ⋮ Rapid Review ⋮ Open Access Journal

Received July 13, 2020, accepted July 30, 2020, date of publication August 10, 2020, date of current version August 20, 2020.

Digital Object Identifier 10.1109/ACCESS.2020.3015335

3D-Printed UHF-RFID Tag for Embedded Applications

NEUS VIDAL[1], JOSEP MARIA LOPEZ-VILLEGAS[1], (Senior Member, IEEE), JORDI ROMEU[2], (Fellow, IEEE), ARNAU SALAS BARENYS[1], ALEIX GARCIA-MIQUEL[1], GISELLE GONZÁLEZ-LÓPEZ[2], AND LUIS JOFRE[2], (Fellow, IEEE)

[1]Department of Electronic and Biomedical Engineering, University of Barcelona (UB), 08028 Barcelona, Spain
[2]Department of Signal Theory and Communications, CommSensLab, Universitat Politècnica de Catalunya (UPC), 08034 Barcelona, Spain

Corresponding author: Neus Vidal (nvidal@ub.edu)

This work was supported by the Spanish Ministry of Economy and Competitiveness, under Project TEC2017-83524-R, Project TEC2016-78028-C-1P, and Project MDM2016-0600.

ABSTRACT This paper presents the design, manufacture and characterization of a novel 3D passive UHF-RFID tag for embedded applications. The prototype is fabricated using additive manufacturing techniques: 3D printing and copper electroplating. The design, manufacturing process and measurement set-up are presented and discussed in detail. We propose a biconical antenna design with spiral strips embedded in the cones to provide compactness without breaking the symmetry of the component and to improve bandwidth. The antenna is matched to a commercial UHF-RFID integrated circuit. We incorporate a packaging design that consists of a dielectric coating, to provide proper operation in different media or surrounding environments with changing electromagnetic properties. The good agreement between experimental results and Finite Element Method simulations allows us to validate the whole process. Finally, a compact capsule-type RFID tag is proposed and its performance in different media is reported.

INDEX TERMS 3D printing, UHF RFID tag, embedded antenna, antenna design, packaging.

I. INTRODUCTION

The use of additive manufacturing (AM) techniques to improve the performance of integrated antenna systems has huge potential. Recently published Special Issues on manufacturing techniques and 3D-printing technology for advanced and novel antenna applications suggest the future impact of this technology [1], [2]. By adopting 3D-printing techniques, we can escape from planarity and produce models that may allow increased compactness and whole system integration, while maintaining electrical performance. An example of an application where compactness and system performance improvement can be of considerable benefit is radio-frequency identification (RFID) technology.

Due to its cost-effectiveness and low power consumption electronics, passive RFID technology is widely used in many industrial applications such as tracking, access control, logistics, etc. [3]. However, there are still important limitations to this technology. One related challenge is making the antenna design sufficiently robust to allow proper operation in a surrounding environment with changing electromagnetic properties. If this requirement is not met, variations in antenna impedance may produce a mismatch and therefore a reduction in the RFID chip activation range. This is critical when dealing with lossy media such as liquids or biological tissues [4]. Hospitals are one example where the impact of the surrounding lossy media (medical personal, patients) can produce a decrease in the radiative efficiency of RFID tags [5].

A second challenge in the design of antennas for RFID applications is ensuring that the RFID tag can work not only close to heterogeneous or lossy media, but also immersed in them. In the literature, we can find case studies of fully embedded RFIDs for application in some industries, such as the automotive and construction sectors [6]–[8]. These report limitations of RFID tag operation, mainly due to the impact of external conditions. It is not only a question of the effect of electrical losses related to the specific medium, but also the time variability of the whole set of electrical properties. An antenna immersed in a certain medium must be able to operate properly, to the maximum extent, regardless of changes in the dielectric constant and conductivity. This does not only mean that it must exhibit good matching throughout a certain range of values, but also that it should respond adequately to temporal variations.

The associate editor coordinating the review of this manuscript and approving it for publication was Nosherwan Shoaib.

Another important aspect, which depends on the operating frequency, is the space distribution of the antenna field regions, as they substantially modify the behavior of the radiated power. The reactive near-field region has a great impact on the behavior of the radiated power of the antenna, as reported in [9]. The presence of lossy media dramatically decreases the radiative efficiency of the antenna, because they interact with the reactive near-field.

Packaging antennas is a potential way to resolve these issues that has already been proposed in previous studies [10]. Dielectric encapsulation to guarantee stable antenna impedance when immersed in a dielectric medium was validated through numerical simulations; and packaging can be designed to minimize changes in antenna reactance. Moreover, keeping the reactive near-field inside the coating minimizes the impact of medium losses on radiative efficiency [9], [11].

In accordance with all these considerations, in this work, we present the design and characterization of a compact 3D-printed passive UHF-RFID tag for embedded applications. Different designs and technologies have been proposed for 3D-printed antennas [1], [2], [12], [13]. Here, we present a novel biconical spiral antenna design, including a dielectric coating that acts as an electromagnetic buffer. The prototype is fabricated using AM techniques: material-jetting 3D printing and cooper electroplating. The antenna design specifications are set to match the input impedance of a commercial UHF-RFID integrated circuit.

The paper is organized as follows. In Section II, we explain the methodology, including the antenna design procedure and manufacturing process. Due to its importance, a whole section (Section III) is devoted to the measurement set-up. In Section IV, the electromagnetic simulations and experimental results are presented and discussed. Finally, Section V presents our main conclusions.

II. ANTENNA DESIGN AND MANUFACTURE

A. DESIGN OF THE 3D ANTENNA

The 3D antenna we designed consists of two main symmetrical radiators, a matching network, and a dielectric coating. The antenna body is a biconical structure with a square plate in the middle, perpendicular to the cone axes, implemented in a dielectric material whose electromagnetic (EM) parameters are: dielectric constant, 2.8 and loss tangent, 0.02. Due to the antenna geometry, we proposed a cylindrical coating. Figure 1 shows a view of the computer-assisted design (CAD) models.

EMPro from Keysight Technologies Inc. was used as the design and simulation environment. The radiators were defined on the external surface of the cones, as outer metal conical sections connected to the middle plate via a conical metal spiral. The matching network is implemented in the middle plate as an inductive transformer. Two square metal loops were defined using metal strips on both sides of the plate and a via hole. This configuration allows broadband matching of the antenna impedance to that of the RFID chip.

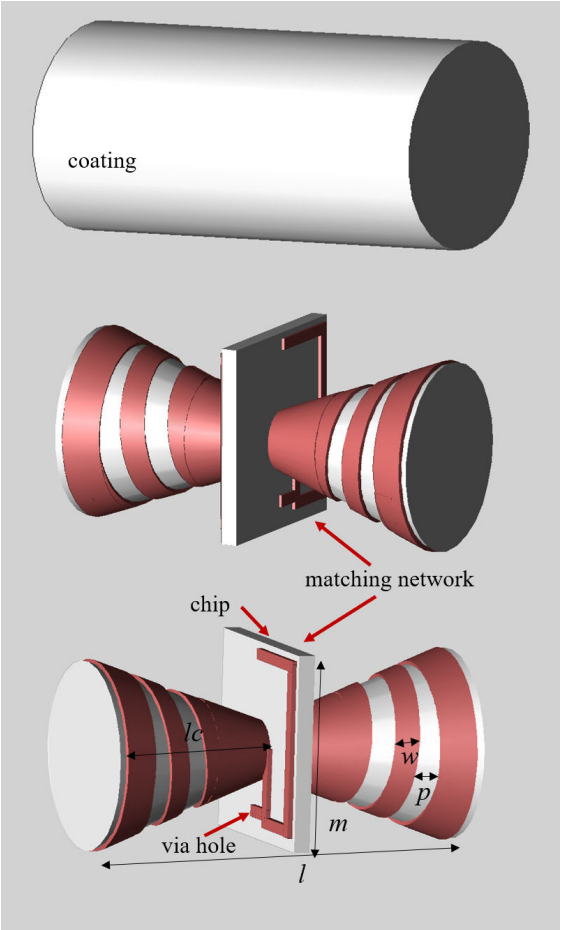

FIGURE 1. 3D view of the coating and the helical antenna design. The matching network located at each side of the perpendicular plate is shown. The via hole and chip locations are indicated. Main design parameters are labeled.

All the metal parts are partially buried inside the dielectric material (i.e., to half its thickness). This is a step required by the manufacturing process that will be discussed in detail in the next section. Finally, the coating is a cylinder that completely encloses the antenna, implemented using the same dielectric material as the body of the antenna. It is used as a buffer to minimize detuning effects due to variations in the EM properties of the surrounding environment.

The main design parameters are: l, the total length of the antenna; α, the cone angle; lc, the width of the conical sections of the radiators; w, the width of the metal trace in the conical spiral; p, the pitch between turns in the conical spiral; and the perimeter and surface of the square loops of the matching network. There are some constraints on these parameters to reduce the dimensions of the design space. For instance, an arbitrary choice of l, lc, w, and p, may lead to impossible geometries, and so unpractical antennas.

We used EM simulation tools based on the Finite Element Method (FEM) to evaluate the response of the antenna in terms of the differential reflection coefficient. This allows for optimization of the antenna design, to fulfill the target specifications. In practice, the right selection of the design parameters leads to antenna designs tuned to the desired operating

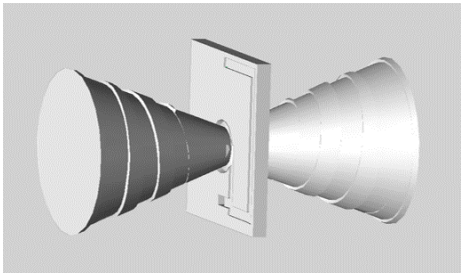

FIGURE 2. View of the final spiral antenna CAD file.

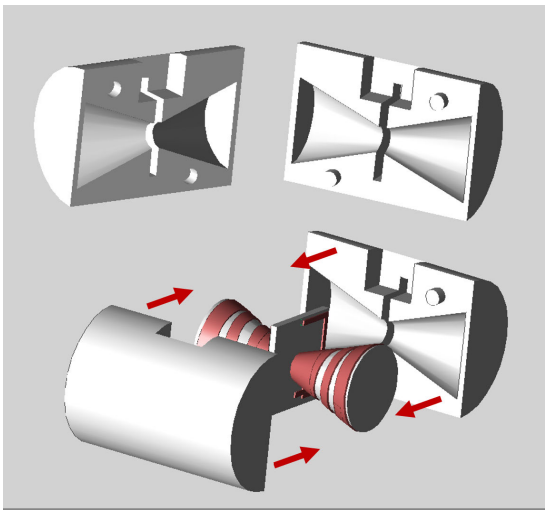

FIGURE 3. View of the final coating CAD files.

frequency and impedance of the RFID chip. Compact designs can also be achieved at the expense of antenna bandwidth.

B. MANUFACTURING PROCESS

The manufacturing process consisted of two groups of tasks that implement the transition from CAD (i.e., the optimized antenna design) to the final part (i.e. the actual component). The first group includes all the virtual tasks and is performed inside the design environment. After the optimized antenna design is obtained, all the simulation ports and field sensors are discarded. All the metal parts as well as all the dielectric parts are combined using Boolean operators into two single objects. Then the metal object is subtracted from the dielectric object to form the printable part. An example of the final result can be observed in Figure 2. The printable part is basically the main body of the antenna with trenches on the surface and via hole where the metal parts are located. This is a consequence of the fact that during the design phase the metal parts are partially buried inside the dielectric material. This group of virtual tasks finishes when the printable CAD object is coded in the appropriate format for 3D printing.

To manufacture the dielectric coating, the main body of the antenna is first subtracted from the dielectric cylinder using Boolean operators. Then, the resulting object is cut into two halves. Finally, after adding alignment features, the resulting structures are ready for 3D printing. An example is shown in Figure 3.

FIGURE 4. View of the final printed coated antenna.

The second group of tasks is related to the printing of the parts. The coating halves are printed directly. For the antenna, the first task consists of spraying the object with a silver ink [14] to form a conductive coating. Then the silver is removed from areas where it is not wanted by polishing so that the silver ink only remains in the trenches of the conical surface, on the middle plate and in the via hole. The remaining silver ink is conductive enough to serve as a seed for a standard copper electroplating process. The role of the silver ink is merely to serve as the seed onto which the copper electroplating layer grows. Any similar conductive ink could be used as the seed. The only effect of the conductivity of the seed is observed at the beginning of cooper growth, and particularly on the initial growth rate until an effective copper layer is present. After that, the growth does not depend on the seed at all.

The result is the final part, corresponding to the optimized antenna design. An example is shown in Figure 4. It is worth noting that the same manufacturing procedure has been successfully used to implement helical-microstrip transmission lines [15], and conical inductors with improved bandwidth [16]. This last reference includes a full explanation and a visual description of the virtual and physical tasks of the process flow for the design and 3D manufacturing.

III. MEASUREMENT SET-UP

To validate the design and manufacturing process of the antenna prototypes, it was necessary for us to compare FEM simulation and experimental results. Accordingly, we needed to measure the differential reflection coefficient of the antenna. Using a standard Vector Network Analyzer (VNA), this requires a transformation from single-ended to differential excitation. To achieve this goal, electrical and electro-optical converters have been proposed. In our case, we used an electrical transformer that incorporates, as a key component, a miniaturized balun NCS4-102+ from Mini-Circuits [17]. We chose this component because its amplitude and phase unbalance are minimal at the operating frequency of the RFID chip (i.e., 0.05 dB and 0.04 degrees at 868 MHz, respectively).

The transformer was implemented using a printed circuit board (PCB). The layout is shown in Figure 5a. On the

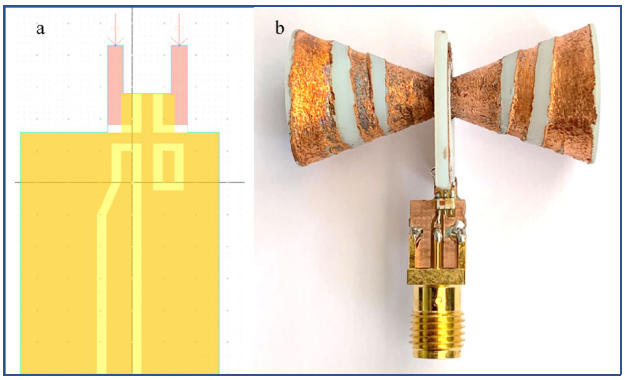

FIGURE 5. a) View of the electrical converter layout. b) Antenna prototype with the single ended to differential converted connected.

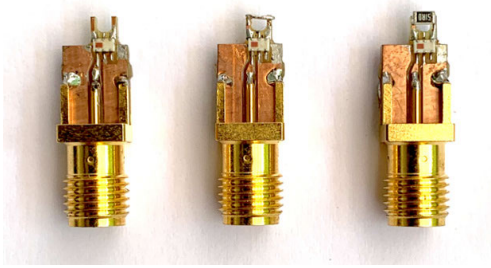

FIGURE 6. View of the calibration kit used to de-embed the effect of SMA connectors and pads. From left to right: open, short, and load.

bottom of the PCB we can observe pads for soldering an edge lunch SubMiniature version A (SMA) connector where the single-ended excitation is applied. In the middle are the pads for soldering the balun. Finally, on top, we can see two pins corresponding to the differential excitation applied to the antenna prototype. Figure 5b shows a sample antenna prototype with the single-ended to differential converter connected at the same location where the RFID chip is to be soldered.

It is important to note that prior to the measurements the VNA must be calibrated properly. This requires a custom calibration kit to be able to de-embed all the effects of the converter, other than the single-ended to differential conversion, from the S parameter measurement; for instance, it is necessary to de-embed insertion loss or impedance mismatch. We designed and manufactured the custom calibration kit using the same procedure as for the single-ended to differential converter. In practice, open, short, and broadband load standards were implemented by connecting the corresponding impedances between the differential pins of three converters. A view of the calibration kit is shown in Figure 6. With this custom calibration kit, the differential reflection coefficient of the antenna prototypes was measured in the range from 700 MHz to 1 GHz using an E5071C 4-port VNA from Keysight Technologies Inc.

IV. RESULTS AND DISCUSSION

A. FINAL DESIGN OF THE ANTENNA AND THE COATING

The production of the final model (antenna plus coating) consisted of different stages. The first was to design the antenna without the coating. The response in terms of the differential reflection coefficient, efficiency and bandwidth was evaluated. A set of antennas were designed and fabricated. We started with a biconical antenna design and introduced the spiral layout, then progressive miniaturization was performed. We varied the α, p and w parameters to obtain the smallest prototype that met the target specifications. Changes in α and w were not critical, similar results were obtained when changing the angle and the section of the radiator. The pitch between turns in the conical spiral was the key parameter: reducing p yielded a compact design, but also produced a major reduction in both efficiency and bandwidth. Table 1 presents the results for 4 different prototypes: the conical reference antenna and 3 spiral antennas. The design we finally selected and which is presented in the previous sections (antenna number 3 in Table 1) offers a compromise between size, bandwidth, and system efficiency. From this point on, all further compaction of the antenna resulted in a drastic bandwidth reduction and a decrease in efficiency (antenna number 4 in Table 1). Once the final design was chosen, we added the coating and readjusted the antenna size in accordance with the change in permittivity.

TABLE 1. Antenna prototypes without coating.

Antenna	Total Length (mm)	Radiation Efficiency (%)	Bandwidth (MHz)
1 	96	99	90-100
2 	52	96.6	60-90
3 	42.5	74.9	40-60
4 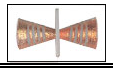	29.9	61.6	15-20

The second stage was related to the coating design, for which we considered previous theoretical work [10]. Those authors showed how proper packaging can minimize changes in the antenna reactance due to differences in the surrounding dielectric medium. They also demonstrated that packaging with a radius of 0.1λ contains most of the stored reactive energy and provides impedance stability. Consequently, we defined an initial radius for the cylinder of 20.65 mm (0.1λ at 868 MHz for the ε_r of the material). To test the effectiveness of this approach, we modeled the performance of our coated antenna when immersed in different media. From this point, antenna and packaging were always modelled and retuned simultaneously.

We chose media with different extreme electrical permittivity and conductivity: fat, cancellous bone, brain, and water. The dielectric properties of these media were taken from [18] and the values are listed in Table 2. The dielectric permittivity ranges from 1 to 84.5. Our results agreed with the previous theoretical analysis [10] and showed the expected behavior. The coating was an effective buffer that minimized the impact

TABLE 2. Electrical properties.

Symbol	Relative Permittivity	Loss Tangent
Reference	1	0
Fat	11.3	0.2
Cancellous Bone	20.9	0.32
Brain	57	0.6
Water	84.5	0.042

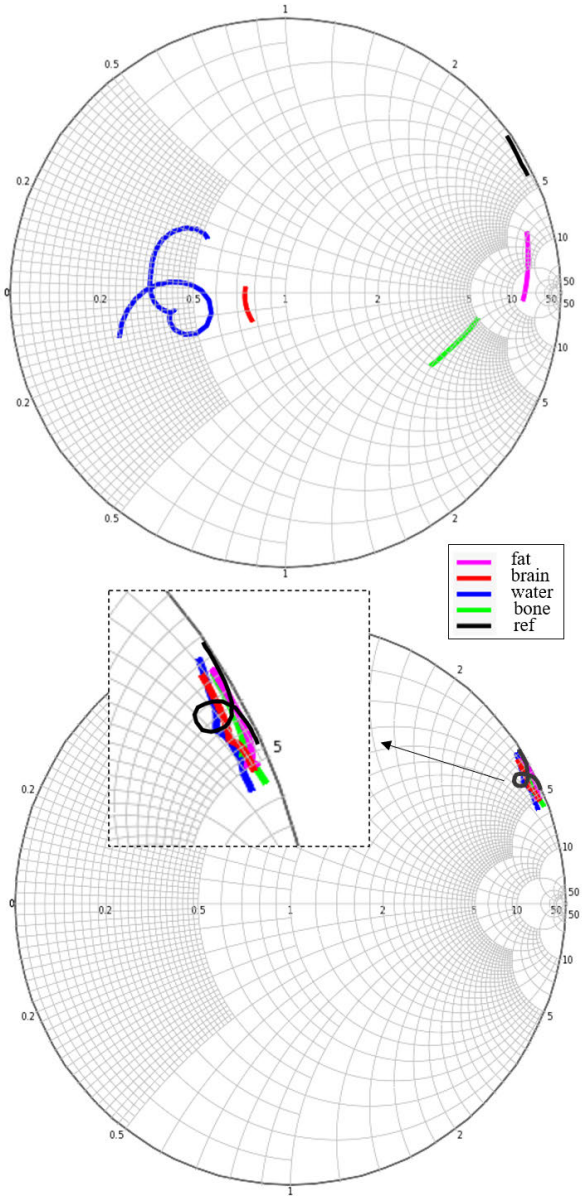

FIGURE 7. Results for the antenna Impedance from 0.75 GHz to 0.9 GHz; a) without coating and b) with coating. Tag is immersed in fat, cancellous bone, brain and water.

of the changing environment on antenna performance. At this point, to analyze possible further compactness of the coating, we progressively tested the impact of a reduction of its radius. Good results were also obtained for a radius of 0.06λ, so we kept this value for the final model.

Figure 7 (top) shows the simulated response of the RFID tag when immersed in different media. For purposes of comparison with previous published results (10), the reference impedance of the Smith Chart was set to 50 Ω. At the bottom of Figure 7, the same results are shown when the antenna is covered with the coating. In both cases, the behavior is analyzed for frequencies in the range from 0.75 to 0.95 GHz. We can observe that the input impedance of the antenna varies greatly when it is immersed in different media, while the values change only slightly when the coating is added. This demonstrates the effectiveness of the coating at stabilizing the antenna impedance, regardless of variation in the EM properties of the surrounding medium. The effect of the dielectric coating on the radiative characteristics of the tag antenna is analyzed in the next section.

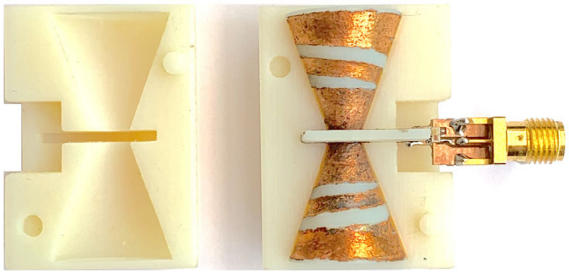

FIGURE 8. View of the final antenna prototype and coating, mounted and ready for EM characterization.

TABLE 3. Dimensions of the prototype.

Symbol	Quantity	Value
l	Total length	33.6 mm
α	Cones angle	20 °
lc	Length conical sections	16.1 mm
m	Metal trace width	2 mm
r	Coating radius	13 mm
cl	Coating length	36 mm
V	Capsule volume	191.13 cm^3

B. TAG RESULTS

Considering all the previous analysis and results, a final prototype was designed, fabricated, and tested. A view of the resulting antenna and coating is shown in Figure 8. To carry out the S11 parameter measurements, an opening was made in the coating. This allowed connection of the single-ended to differential converter (also shown in the figure) to the antenna. All the dimensions of the prototype, including antenna and coating, are indicated in Table 3.

The reflection coefficient of the prototype in the frequency band of interest is shown in Figure 9. The figure compares the simulation results obtained using FEM with the experimental measurements after de-embedding the effect of the single-ended to differential converter. Good agreement is observed between the experimental results and the FEM simulations, especially if we consider that the simulations were carried out using a true differential port while the measurements required the use of the single-ended to differential converter and a de-embedding procedure. In any case, we did observe some discrepancies, especially in

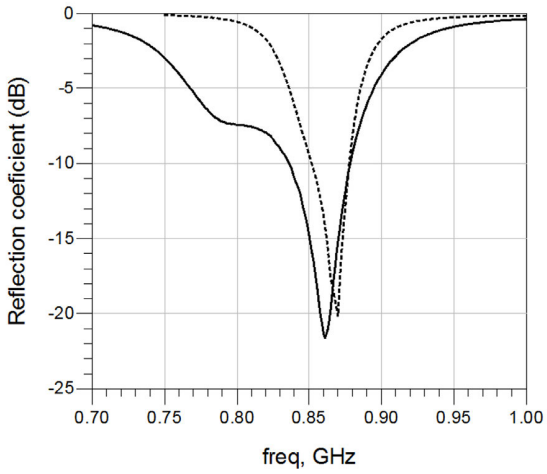

FIGURE 9. Simulated (dotted line) and measured (continuous line) reflection coefficient of the tag on air.

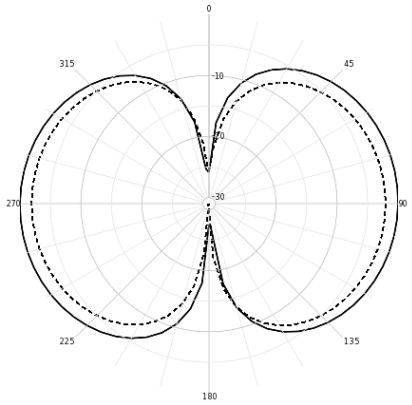

FIGURE 10. Polar cut of the radiation gain as a function of theta for phi=0: results of the final tag antenna without coating (continuous line) and with coating (dotted line).

the bandwidth. These discrepancies have two main origins. The first is the effect of printing tolerances. The printing accuracy is about 60 μm in the XY-plane and, 16 μm along the Z-axis. Considering the complexity of the geometry, this leads to a variable accuracy throughout the whole structure that is reflected in its electromagnetic behavior. This is particularly important for the most sensitive parts of the design, such as the matching network or the spirals. The second is related to possible variation of the electrical permittivity of the base structure. In the figure we can observe that the measured resonant frequency of the prototype is 860 MHz: a deviation of 8 MHz from the target value of 868 MHz. Concerning the antenna bandwidth at -10 dB, the values obtained are 26 MHz (FEM) and 39 MHz (experimental). This bandwidth offers enough compensation for detuning effects resulting from the tolerances of the manufacturing process.

Concerning the radiative properties of the coated antenna prototype, the simulated system efficiency was 42.18% at 868 MHz. The value without the coating was 74.9% (Table 1). The gain decreased from 0.34 dB to -2.99 dB. Finally, the impact of the coating on the radiation pattern is plotted on Figure 10.

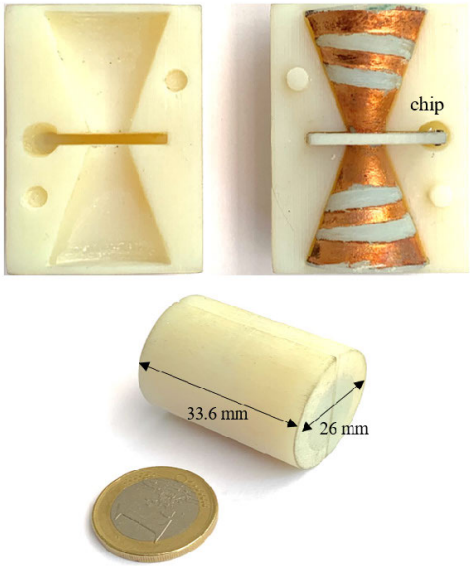

FIGURE 11. View of the final UHF-RFID Tag capsule.

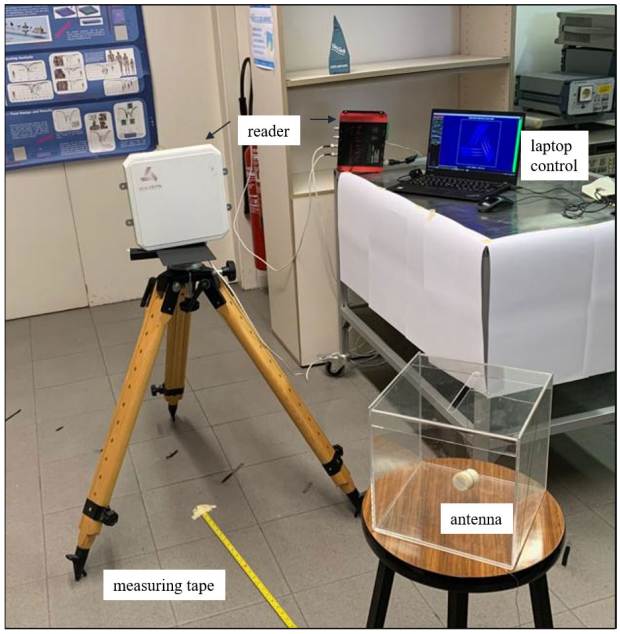

FIGURE 12. View of the RFID read-range measurement setup.

After validating the antenna design and the effectiveness of the dielectric coating, we considered the integration of the RFID IC to implement a fully functional device. In this case, the RFID IC was the Higgs 3 from Alien Technology, with a power threshold sensitivity of -15/-17 dBm. The input impedance of this component was used as a reference throughout the whole design process to match the antenna impedance. The final UHF-RFID tag capsule is shown in Figure 11: it has a volume of 191.13 cm^3 (length 36 mm, radius 13 mm). To evaluate the performance of the prototype, a commercial "Alien ALR-9900+" [19] reader was used. The set-up for measuring the RFID read-range is shown in Figure 12. The reader antenna was secured on a tripod aligned with the tag. The tag was fixed via a plastic wire

inside a methacrylate box. A measuring tape was placed on the floor. The tag measurements started at 0.5 m from the reader. Control software allowed us to check the reader–tag connectivity on the laptop. The tag was covered with a plastic film to waterproof the electronic components. First, the measurements were performed in air, and a read range of 4.5 m was obtained, which is coherent with the sensitivity of the chip (-15/-17 dBm). Then the tag was tested immersed in water and we obtained a 60% reduction in the range of the communication link. This agrees with EM simulations that account for losses in water, and validates the communication capabilities of the proposed tag.

V. CONCLUSION

In this work we present the design, manufacturing process, and results of experimental characterization of a 3D-printed passive UHF-RFID tag for embedded applications. We adopt a biconical geometry with 3D spirals on its surfaces to increase compactness. Geometrical parameters, such as the cone angle, distance between the metal strips and their dimensions, were analyzed to reduce the overall size of the prototype while maintaining, as far as possible, its frequency tuning, impedance matching and communication capabilities. Packaging consisting of a dielectric coating was added to minimize impedance changes when the antenna is immersed in different dielectric media. Initially, simulations were carried out to assess the impedance matching, in terms of the reflection coefficient, and the operational range of the antenna. Then we analyzed the coating. A specific cylindrical design was suggested, to contain most of the stored reactive energy and provide proper operation in different media or in environments with changing electromagnetic properties. The system was tested when immersed in different extreme materials, including air, water, and biological tissues.

After validating the design process, a tag prototype was fabricated using additive manufacturing techniques: 3D printing and copper electroplating. A specific measurement set-up was implemented to accurately measure the differential response of the antenna prototype. Finally, a fully functional compact UHF-RFID tag was assembled combining the antenna, the dielectric coating, and a commercial RFID IC. The results demonstrate the feasibility and good performance of the system. The coated 3D-printed antenna for RFID applications shows promising behavior in the UHF-RFID band for embedded applications. Sectors such as the construction industry, motor industry and healthcare, among others, could benefit from the use of tags that minimize the impact of external conditions and lossy media.

ACKNOWLEDGMENT

The authors would like to thank Alien Technologies for providing the IC.

REFERENCES

[1] "Guest Editorial: Microwave components and antennas based on advanced manufacturing techniques," *IET Microw., Antennas Propag.*, vol. 11, no. 14, pp. 1919–1920, Nov. 2017, doi: 10.1049/iet-map.2017.1007.
[2] S. K. Sharma, H. Xin, B.-I. Wu, J. C. Vardaxoglou, and C. H. Chan, "Guest editorial special cluster on three-dimensional printed antennas and electromagnetic structures," *IEEE Antennas Wireless Propag. Lett.*, vol. 17, no. 11, pp. 1998–2002, Nov. 2018.
[3] K. Jung and S. Lee, "A systematic review of RFID applications and diffusion: Key areas and public policy issues," *J. Open Innov. Technol., Market, Complex.*, vol. 1, no. 1, pp. 1–19, Dec. 2015.
[4] G. Deschamps, "Impedance of an antenna in a conducting medium," *IRE Trans. Antennas Propag.*, vol. 10, no. 5, pp. 648–650, Sep. 1962.
[5] W. Yao, C.-H. Chu, and Z. Li, "The use of RFID in healthcare: Benefits and barriers," in *Proc. IEEE Int. Conf. RFID-Technol. Appl.*, Jun. 2010, pp. 128–134.
[6] S. Basat, M. M. Tentzeris, and J. Laskar, "Design and development of a miniaturized embedded UHF RFID tag for automotive tire applications," in *Proc. IEEE Int. Workshop Antenna Technol. Small Antennas Novel Metamater.*, Lake Buena Vista, FL, USA, vol. 1, May/Jun. 2005, pp. 867–870.
[7] S.-H. Jeong and H.-W. Son, "UHF RFID tag antenna for embedded use in a concrete floor," *IEEE Antennas Wireless Propag. Lett.*, vol. 10, pp. 1158–1161, 2011.
[8] J.-M. Laheurte, A. Kabalan, H. Retima, E. Piedallu, F. Michelis, and B. Lebental, "Embedded UHF RFID tag for durability monitoring in concrete," *Wireless Sensor Netw.*, vol. 8, no. 7, pp. 137–144, 2016.
[9] A. K. Skrivervik, "Implantable antennas: The challenge of efficiency," in *Proc. 7th Eur. Conf. Antennas Propag. (EuCAP)*, Apr. 2013, pp. 3627–3631.
[10] J. Romeu, G. Gonzalez-Lopez, S. Blanch, and L. Jofre, "Antenna packaging for in-body applications," in *Proc. 14th Eur. Conf. Antennas Propag. (EuCAP)*, Copenhagen, Denmark, Mar. 2020, pp. 1–5.
[11] A. K. Skrivervik and F. Merli, "Design strategies for implantable antennas," in *Proc. Loughborough Antennas Propag. Conf.*, Nov. 2011, pp. 1–5.
[12] J. Bjorgaard, M. Hoyack, E. Huber, M. Mirzaee, Y.-H. Chang, and S. Noghanian, "Design and fabrication of antennas using 3D printing," *Prog. Electromagn. Res. C*, vol. 84, pp. 119–134, 2018.
[13] M. Liang, J. Wu, X. Yu, and H. Xin, "3D printing technology for RF and THz antennas," in *Proc. Int. Symp. Antennas Propag. (ISAP)*, Okinawa, Japan, Oct. 2016, pp. 536–537
[14] *Silver Adhesive Conductive Paint*. Accessed: May 30, 2020. [Online]. Available: https://docs.rs-online.com/d712/0900766b815139c0.pdf
[15] J. M. Lopez-Villegas, A. Salas, and N. Vidal, "Modeling of 3-D-printed helical-microstrip transmission lines for RF applications," *IEEE Trans. Microw. Theory Techn.*, vol. 67, no. 12, pp. 4914–4921, Dec. 2019.
[16] J. M. Lopez-Villegas, N. Vidal, J. Sieiro, A. Salas, B. Medina, and F. M. Ramos, "Study of 3-D printed conical inductors for broadband RF applications," *IEEE Trans. Microw. Theory Techn.*, vol. 66, no. 8, pp. 3597–3602, Aug. 2018.
[17] *Ceramic Balun RF Transformer*. Accessed: May 30, 2020. [Online]. Available: https://www.minicircuits.com/pdfs/NCS4-102+.pdf
[18] C. Gabriel, "Compilation of the dielectric properties of body tissues at RF and microwave frequencies," Occupational Environ. Health Directorate, Radiofrequency Radiat. Division, Brooks Air Force Base, San Antonio, Texas, USA, Tech. Rep. N.AL/OE-TR-1996-0037, 1996.
[19] *Alien Technology Readers*. Accessed: Mar. 18, 2020. [Online]. Available: http://www.alientechnology.com/products/readers/

NEUS VIDAL received the Ph.D. degree in physics from the University of Barcelona, Spain, in 1995. She is currently an Associate Professor with the University of Barcelona, where she is also a member of the Group of Excellence for Radio Frequency Components and Systems. Her current research interests include antenna design for biomedical applications and electromagnetic propagation-related issues.

JOSEP MARIA LOPEZ-VILLEGAS (Senior Member, IEEE) received the Ph.D. degree in physics from the University of Barcelona, Barcelona, Spain, in 1990. He is currently the Director of the Group of Excellence for Radio Frequency Components and Systems, University of Barcelona, where he is also a Full Professor with the Department of Electronic and Biomedical Engineering. His research interests include the design, optimization, and test of RF components, circuits and systems performed using silicon, multilayered technologies, such as multichip modules and low-temperature co-fired ceramics, 3D printing, the use of 3-D simulators for electromagnetic analysis of RF components, circuits and systems, the analysis of electromagnetic compatibility and electromagnetic interference problems, and the interaction of electromagnetic energy with biological tissues. He is particularly interested in the modeling and optimization of integrated inductors and transformers for general RF applications, and in particular for the development of new homodyne transceiver architectures based on injection-locked oscillators.

JORDI ROMEU (Fellow, IEEE) was born in Barcelona, Spain, in 1962. He received the Ingeniero de Telecomunicación and Doctor Ingeniero de Telecomunicaciòn degrees from the Universitat Politècnica de Catalunya (UPC), in 1986 and 1991, respectively. In 1985, he joined the Antennalab, Signal Theory and Communications Department, UPC, where he is currently a Full Professor and involved in antenna near-field measurements, antenna diagnostics, and antenna design. He was a Visiting Scholar at the Antenna Laboratory, University of California at Los Angeles, Los Angeles, in 1999, on an NATO Scientific Program Scholarship, and at the University of California at Irvine, in 2004. He holds several patents and has published 60 refereed articles in international journals and 80 conference proceedings. He was a Grand Winner of the European IT Prize, awarded by the European Commission, for his contributions in the development of fractal antennas, in 1998. More information can be found in http://www.researchgate.net/profile/Jordi_Romeu.

ARNAU SALAS BARENYS received the B.E. degree in electronics engineering of telecommunication from the Universitat de Barcelona (UB), Spain, and the M.S. degree in telecommunication engineering from the Universitat Autònoma de Barcelona (UAB), Spain, in 2017. He is currently pursuing the Ph.D. degree in engineering and applied science with UB. His research interests include electronics design, radiofrequency and electromagnetic modelling, communication systems, 3D design, and 3D printing.

ALEIX GARCIA-MIQUEL received the M.Sc. degree in telecommunication engineering from the Universitat Politècnica de Catalunya (UPC), Barcelona, Spain, in 2009, and the M.Sc. and Ph.D. degrees in biomedical engineering from the Universitat de Barcelona (UB), Barcelona, in 2013 and 2018, respectively. Since 2012, he has been collaborating with the Radiofrequency Group (GRAF), Electronics and Biomedical Engineering Department, UB, as an Assistant Professor and then as an External Collaborator. He has been involved in a wide range of positions, from multinational corporations to start-ups. His current research interests include antenna design, medical devices development, fetal medicine, and management of multidisciplinary teams.

GISELLE GONZÁLEZ-LÓPEZ was born in Havana, Cuba, in 1992. She received the B.S. degree in telecommunication and electronics engineering from Technical University ISPJAE, Havana, in 2015, and the M.S. degree in telecommunication engineering from the Technical University of Catalonia (UPC), Barcelona, in 2018. She is currently pursuing the Ph.D. degree with the Signal Theory and Communications (TSC) Department, Research Group of Remote Sensing, Antennas, Microwaves and Superconductivity, Unidadde Excelencia Maria de Maeztu, UPC. From 2016 to 2017, she was an Intern at the Research Group of Mobile communications (GRCM), UPC. Her research interests include but are not limited to embedded systems, media characterization, microwave antenna design, antenna impedance characterization, wireless communications, and mobile systems.

LUIS JOFRE (Fellow, IEEE) received the M.Sc. and Ph.D. degrees in electrical engineering (telecommunication engineering) from the Universitat Politècnica de Catalunya (UPC), Barcelona, Spain, in 1978 and 1982, respectively. Since 1982, he has been with the Communications Department, Telecommunication Engineering School, UPC, as an Associate Professor and then has been a Full Professor, since 1989. He was also a Visiting Professor at the Ecole Supèrieure d'Electricitè Paris, from 1981 to 1982, where he was involved in microwave antenna design and imaging techniques for medical and industrial applications. From 1986 to 1987, he was a Visiting Fulbright Scholar with the Georgia Institute of Technology, Atlanta, GA, USA, where he was involved in antenna near-field measurements and electromagnetic imaging. From 2000 to 2001, he was a Visiting Professor with the Electrical and Computer Engineering Department, Henry Samueli School of Engineering, University of California at Irvine, CA, USA, where he was involved in reconfigurable antennas and microwave sensing of civil engineering structures. He has been the Director of the UPC-Telefonica Chair on Information Society Future Trends, since 2003. He was a Principal Investigator of the 2008–2013 Spanish Terahertz Sensing Lab Consolider Project, the Research Leader of the 2017–2020 ComSense Lab Maria de Maeztu Project, the Academic Director of the Consortium for Future Urban Mobility (Carnet), and the Chairman of the EIT-Urban Mobility European Association. He has authored more than 200 scientific and technical articles, reports, and chapters in specialized volumes. His current research interests include antennas, electromagnetic scattering and imaging, and system miniaturization for wireless, and sensing industrial and bio-applications from microwaves to terahertz frequencies.

Bibliography

[1] V. K. Nassa, "Wireless communications: Past, present and future," *Dronacharya Research Journal*, vol. 50.

[2] A. M. French and J. P. Shim, "The digital revolution: Internet of things, 5g, and beyond," *Communications of the Association for Information Systems*, vol. 38, no. 1, p. 40, 2016.

[3] C. A. Balanis, *Advanced engineering electromagnetics*. John Wiley & Sons, 2012.

[4] J. S. Bobowski and T. Johnson, "Permittivity measurements of biological samples by an open-ended coaxial line," *Progress In Electromagnetics Research*, vol. 40, pp. 159–183, 2012.

[5] A. Ihamouten, G. Villain, and X. Dérobert, "Complex permittivity frequency variations from multioffset gpr data: Hydraulic concrete characterization," *IEEE Transactions on Instrumentation and Measurement*, vol. 61, no. 6, pp. 1636–1648, 2012.

[6] A. Cataldo, E. De Benedetto, and G. Cannazza, "Hydration monitoring and moisture control of cement-based samples through embedded wire-like sensing elements," *IEEE Sensors Journal*, vol. 15, no. 2, pp. 1208–1215, 2014.

[7] N. Coutanceau-Monteil, C. Jacquin, *et al.*, "Improvements of the coaxial line technique for measuring complex dielectric permittivities of centimetric samples in the 20 to 1,000 mhz range: application to sedimentary rocks," *The Log Analyst*, vol. 34, no. 05, 1993.

[8] A. Robert, "Dielectric permittivity of concrete between 50 mhz and 1 ghz and gpr measurements for building materials evaluation," *Journal of applied geophysics*, vol. 40, no. 1-3, pp. 89–94, 1998.

[9] S. Blanch and A. Aguasca, "Seawater dielectric permittivity model from measurements at l band," in *IGARSS 2004. 2004 IEEE International Geoscience and Remote Sensing Symposium*, vol. 2, pp. 1362–1365, IEEE, 2004.

[10] B. Davis, C. Grosvenor, R. Johnk, D. Novotny, J. Baker-Jarvis, and M. Janezic, "Complex permittivity of planar building materials measured with an ultra-wideband free-field antenna measurement system," *Journal of research of the National Institute of Standards and Technology*, vol. 112, no. 1, p. 67, 2007.

[11] W. B. Weir, "Automatic measurement of complex dielectric constant and permeability at microwave frequencies," *Proceedings of the IEEE*, vol. 62, no. 1, pp. 33–36, 1974.

[12] E. Piuzzi, G. Cannazza, A. Cataldo, S. Chicarella, E. De Benedetto, F. Frezza, S. Pisa, S. Prontera, and F. Timpani, "Measurement system for evaluating dielectric permittivity of granular materials in the 1.7–2.6-ghz band," *IEEE Transactions on Instrumentation and Measurement*, vol. 65, no. 5, pp. 1051–1059, 2015.

[13] H. C. Rhim and O. Buyukozturk, "Electromagnetic properties of concrete at microwave frequency range," *Materials Journal*, vol. 95, no. 3, pp. 262–271, 1998.

[14] A. A. Note, "Agilent basics of measuring the dielectric properties of materials," *Agilent literature number*, pp. 1–34, 2006.

[15] K. C. Yaw, "Measurement of dielectric material properties," *Application Note. Rohde & Schwarz*, pp. 1–35, 2012.

[16] D. M. Pozar, *Microwave engineering*. John wiley & sons, 2011.

[17] A. K. Skrivervik, M. Bosiljevac, and Z. Sipus, "Fundamental limits for implanted antennas: Maximum power density reaching free space," *IEEE Transactions on Antennas and Propagation*, vol. 67, no. 8, pp. 4978–4988, 2019.

[18] R. Moore, "Effects of a surrounding conducting medium on antenna analysis," *IEEE Transactions on Antennas and Propagation*, vol. 11, no. 3, pp. 216–225, 1963.

[19] M. Bosiljevac, Z. Sipus, and A. K. Skrivervik, "Radiation limitations for small implanted antennas," in *2019 13th European Conference on Antennas and Propagation (EuCAP)*, pp. 1–4, IEEE, 2019.

[20] D. Nikolayev, Z. Sipus, M. Bosiljevac, W. Joseph, M. Zhadobov, R. Sauleau, L. Martens, and A. K. Skrivervik, "Optimal frequency of operation and radiation efficiency limitations of implantable antennas," in *2020 14th European Conference on Antennas and Propagation (EuCAP)*, pp. 1–4, IEEE, 2020.

[21] Z. Sipus, M. Bosiljevac, D. Nikolayev, and A. Skrivervik, "Design concerns for in-body antennas based on frequency analysis of fundamental radiation limitations," in *2020 14th European Conference on Antennas and Propagation (EuCAP)*, pp. 1–5, IEEE, 2020.

[22] A. P. Gregory and R. Clarke, "Tables of the complex permittivity of dielectric reference liquids at frequencies up to 5 ghz.," 2012.

[23] H. C. Rhim and O. Buyukozturk, "Electromagnetic properties of concrete at microwave frequency range," *Materials Journal*, vol. 95, no. 3, pp. 262–271, 1998.

[24] E. Gartner, J. Young, D. Damidot, and I. Jawed, "Hydration of portland cement," *Structure and performance of cements*, vol. 2, pp. 57–113, 2002.

[25] M. Narmluk and T. Nawa, "Effect of fly ash on the kinetics of portland cement hydration at different curing temperatures," *Cement and concrete research*, vol. 41, no. 6, pp. 579–589, 2011.

[26] A. Cataldo, E. De Benedetto, and G. Cannazza, "Hydration monitoring and moisture control of cement-based samples through embedded wire-like sensing elements," *IEEE Sensors Journal*, vol. 15, no. 2, pp. 1208–1215, 2014.

[27] S. Zhou, W. Sheng, F. Deng, X. Wu, and Z. Fu, "A novel passive wireless sensing method for concrete chloride ion concentration monitoring," *Sensors*, vol. 17, no. 12, p. 2871, 2017.

[28] S. Zhou, F. Deng, L. Yu, B. Li, X. Wu, and B. Yin, "A novel passive wireless sensor for concrete humidity monitoring," *Sensors*, vol. 16, no. 9, p. 1535, 2016.

[29] B. Ozbey, V. B. Erturk, H. V. Demir, A. Altintas, and O. Kurc, "A wireless passive sensing system for displacement/strain measurement in reinforced concrete members," *Sensors*, vol. 16, no. 4, p. 496, 2016.

[30] A. Ramos, D. Girbau, A. Lazaro, and R. Villarino, "Wireless concrete mixture composition sensor based on time-coded uwb rfid," *IEEE Microwave and Wireless Components Letters*, vol. 25, no. 10, pp. 681–683, 2015.

[31] D. Jayawardana, R. Liyanapathirana, and X. Zhu, "Rfid-based wireless multisensory system for simultaneous dynamic acceleration and strain measurements of civil infrastructure," *IEEE Sensors Journal*, vol. 19, no. 24, pp. 12389–12397, 2019.

[32] Y. Liu, F. Deng, Y. He, B. Li, Z. Liang, and S. Zhou, "Novel concrete temperature monitoring method based on an embedded passive rfid sensor tag," *Sensors*, vol. 17, no. 7, p. 1463, 2017.

[33] S. Manzari, T. Musa, M. Randazzo, Z. Rinaldi, A. Meda, and G. Marrocco, "A passive temperature radio-sensor for concrete maturation monitoring," in *2014 IEEE RFID Technology and Applications Conference (RFID-TA)*, pp. 121–126, IEEE, 2014.

[34] G. González López, "Advanced embedded uwb t-match antenna system for rfid sensing," Master's thesis, Universitat Politècnica de Catalunya, 2018.

[35] C. A. Balanis, *Antenna theory: analysis and design*. John wiley & sons, 2016.

[36] P. V. Nikitin, K. S. Rao, R. Martinez, and S. F. Lam, "Sensitivity and impedance measurements of uhf rfid chips," *IEEE Transactions on Microwave Theory and Techniques*, vol. 57, no. 5, pp. 1297–1302, 2009.

[37] C. Wang and W. Dilger, "Prediction of temperature distribution in hardening concrete," *RILEM Proceedings 25, Thermal Cracking in Concrete at Early Ages*, pp. 21–28, 1994.

[38] A. K. Schindler, T. Dossey, and B. F. McCullough, "Temperature control during construction to improve the long term performance of portland cement concrete pavements," tech. rep., 2002.

[39] A. Neville, "Properties of concrete (vol. 4): Longman london," 1995.

[40] T. Kollie, J. Horton, K. Carr, M. Herskovitz, and C. Mossman, "Temperature measurement errors with type k (chromel vs alumel) thermocouples due to short-ranged ordering in chromel," *Review of Scientific Instruments*, vol. 46, no. 11, pp. 1447–1461, 1975.

[41] W. B. Weir, "Automatic measurement of complex dielectric constant and permeability at microwave frequencies," *Proceedings of the IEEE*, vol. 62, no. 1, pp. 33–36, 1974.

[42] H. J. Liebe, G. A. Hufford, and T. Manabe, "A model for the complex permittivity of water at frequencies below 1 thz," *International Journal of Infrared and Millimeter Waves*, vol. 12, no. 7, pp. 659–675, 1991.

[43] S.-J. Kwon, M. Q. Feng, and S. S. Park, "Characterization of electromagnetic properties for durability performance and saturation in hardened cement mortar," *NDT & E International*, vol. 43, no. 2, pp. 86–95, 2010.

[44] C. Society, *Guidance on Radar Testing of Concrete Structures*. Concrete Society, 1997.

[45] D. Bucur, N. Militaru, and G. Lojewski, "Models of dielectric materials used in high-speed design by fd 2 td method," in *2013 IEEE 19th International Symposium for Design and Technology in Electronic Packaging (SIITME)*, pp. 129–133, IEEE, 2013.

[46] I. del Hormigón Estructural, "Ehe-08," *Madrid, Ministerio de Fomento, Secretaría General Técnica*, 2008.

[47] Y. Shen, C. L. Law, and W. Dou, "Ultra-wideband measurement of the dielectric constant and loss tangent of concrete slabs," in *2008 China-Japan Joint Microwave Conference*, pp. 537–540, IEEE, 2008.

[48] M.-K. Olkkonen, V. Mikhnev, and E. Huuskonen-Snicker, "Complex permittivity of concrete in the frequency range 0.8 to 12 ghz," in *2013 7th European Conference on Antennas and Propagation (EuCAP)*, pp. 3319–3321, IEEE, 2013.

[49] B. Filali, F. Boone, J. Rhazi, and G. Ballivy, "Design and calibration of a large open-ended coaxial probe for the measurement of the dielectric properties of concrete," *IEEE Transactions on Microwave Theory and Techniques*, vol. 56, no. 10, pp. 2322–2328, 2008.

[50] S. Pisa, E. Pittella, E. Piuzzi, P. D'Atanasio, and A. Zambotti, "Permittivity measurement on construction materials through free space method," in *2017 IEEE International Instrumentation and Measurement Technology Conference (I2MTC)*, pp. 1–4, IEEE, 2017.

[51] W. J. McCarter, G. Starrs, and T. M. Chrisp, "Electrical conductivity, diffusion, and permeability of portland cement-based mortars," *Cement and Concrete Research*, vol. 30, no. 9, pp. 1395–1400, 2000.

[52] I. Foundation, *TISSUE PROPERTIES*. Available at https://itis.swiss/virtual-population/tissue-properties/database/dielectric-properties/.

[53] M. Bosiljevac, Z. Sipus, and A. K. Skrivervik, "Propagation in finite lossy media: An application to wban," *IEEE Antennas and Wireless Propagation Letters*, vol. 14, pp. 1546–1549, 2015.

[54] M. Gao, D. Nikolayev, M. Bosiljevac, Z. Sipus, and A. K. Skrivervik, "Rules of thumb to assess losses of implanted antennas," in *2021 15th European Conference on Antennas and Propagation (EuCAP)*, IEEE.

[55] S. I. Valls *et al.*, "Design of a x-wave mini-anechoic chamber for measuring minituarized and embedded wireless devices," B.S. thesis, Universitat Politècnica de Catalunya, 2020.

[56] V. Rodriguez, "Basic rules for indoor anechoic chamber design [measurements corner]," *IEEE Antennas and Propagation Magazine*, vol. 58, no. 6, pp. 82–93, 2016.

[57] M. Wuschek, "Test cells for investigating emission and susceptibility attractively priced alternatives to the anechoic chamber," *NEWS-ROHDE AND SCHWARZ*, pp. 7–9, 2000.

[58] WitekLab. Available at https://www.witeklab.com/en/.

[59] *EM Microelectronic, 18000-63 Type C (Gen2) and 18000-63 Type C / 18000-64 Type D (Gen2/TOTAL) RFID IC.* Available at https://www.emmicroelectronic.com/product/epc-and-uhf-ics/em4325.

[60] N. ID, *NORDIC ID NUR-10W RFID MODULES.* Available at https://www.nordicid.com/device/modules/.

[61] J. C. Bolomey, S. Capdevila, L. Jofre, and J. Romeu, "Electromagnetic modeling of rfid-modulated scattering mechanism. application to tag performance evaluation," *Proceedings of the IEEE*, vol. 98, no. 9, pp. 1555–1569, 2010.

[62] S. Capdevila, L. Jofre, J. Romeu, and J. C. Bolomey, "Multi-loaded modulated scatterer technique for sensing applications," *IEEE Transactions on Instrumentation and Measurement*, vol. 62, no. 4, pp. 794–805, 2013.

[63] Á. C. Aznar, J. R. Robert, J. M. R. Casals, L. J. Roca, S. B. Boris, and M. F. Bataller, *Antenas.* Univ. Politèc. de Catalunya, 2004.

[64] A. Abbosh, B. Henin, P. Sharpe, *et al.*, "Head phantom for testing microwave systems for head imaging," in *2012 Cairo International Biomedical Engineering Conference (CIBEC)*, pp. 191–193, IEEE, 2012.

[65] D. Paris, W. Leach, and E. Joy, "Basic theory of probe-compensated near-field measurements," *IEEE Transactions on Antennas and Propagation*, vol. 26, no. 3, pp. 373–379, 1978.